

Copyright is owned by the Author of the thesis. Permission is given for a copy to be downloaded by an individual for the purpose of research and private study only. The thesis may not be reproduced elsewhere without the permission of the Author.

Quantum many-body dynamics
of
bright matter-wave solitons



A thesis presented in partial fulfilment of the
requirements for the degree of
Doctor of Philosophy
at
Massey University, Albany
New Zealand

Thomas Ernst

August 2011

Abstract

The interplay of particle and resonant wave scattering including nonlinear effects creates systems of diverse and interesting quantum many-body physics. A better understanding of the physics in these systems could lead to new and exiting application exploiting their quantum nature.

As an example, in this thesis we investigate the scattering of bright matter-wave solitons in ultracold gases on a square well in one spatial dimension. For this, solutions of the mean-field Gross-Pitaevskii approximation and a full quantum many-body method, the so-called multiconfigurational time-dependent Hartree approach (MCTDH), are compared.

The MCTDH method is based on a finite basis set expansion, which naturally leads to errors in system properties, such as energies and densities, when compared to exact results. In this thesis, we propose an efficient solution to this problem by rescaling the interaction strength between the particles. Even for very large interactions in the Tonks-Girardeau limit, the rescaling leads to significant improvements. This is validated by successfully applying the rescaling to problems in ring systems as well as external confinements, such as a harmonic well and a double-well.

The MCTDH method is then applied to the soliton scattering problem and compared to results from mean-field calculations. The latter verify that solitons, when scattered on a well, show quantum effects, such as reflection. For the first time, we show that a soliton can be additionally permanently trapped by the well due to resonances with bound states.

For this thesis, to extend these results to a full many-body approach, we developed QiwiB. It is a program package implementing the MCTDHB method, which is a derivative of the MCTDH method, but optimised for bosonic systems. Limits for the validity of the MCTDHB approach are addressed by convergence studies on the soliton scattering problem. Furthermore, we demonstrate that the scattering on the well enables the creation of macroscopic binary quantum superposition states, i.e. *NOON* states. Novel *NOON* states corresponding to a superposition of a reflected soliton and a trapped soliton are observed. These states are shown to exist for a large range of initial conditions, and a possible experimental realisation is discussed.

Acknowledgments

Firstly, I want to thank my supervisor Prof. Joachim Brand for bringing me all the way from Germany to New Zealand and introducing me to the fascinating world of matter-wave solitons. I am very grateful for all the fruitful discussions, suggestions and his patience with me as well as all the critical comments, from which I have learned so much.

I also want to thank David Hallwood, for the many extensive and inspiring discussions as well as for being such a great work colleague. I also want to thank Jake Gulliksen for being an awesome office mate. I really enjoyed collaborating with them on physics projects as well as the time together on the tennis court. I also want to thank Renyuan, Sasha and Gaby for all the great conversations and the fun time together, and creating such a great atmosphere in the office.

I also would like to thank Prof. Peter Schwerdtfeger for all the BBQs and the great advice on physics problems as well as life issues.

Furthermore many thanks go to all current and former members of the CTCP, in particular Andreas, Andy, James, Matthias, and Michael for their awesome work on the computer administration, and Patrick for help and advice as well as all the coffee.

My gratitude also goes to Prof. Hans-Dieter Meyer, for his kind introduction to MCTDH, and his patience in finding answers to all my questions.

Most of all, I want to thank Susan, for just being her and making my life a dream. You are wonderful and I would not know what to do without you.

Last but not least, I want to thank my parents, who always supported me. Me going to New Zealand certainly was not what they were hoping for, and therefore I am very grateful and happy to have parents who I can always count on and never stop loving me. Thank you for everything, you are the best.

Contents

1	Introduction	1
1.1	Background and motivation	1
1.2	Outline of this thesis	7
1.3	Publications	9
2	Theoretical background	11
2.1	Simple theories on Bose-Einstein condensates	11
2.1.1	The ideal gas	11
2.1.2	Interactions	12
2.1.3	Gross-Pitaevskii equation	13
2.1.4	Beyond Gross-Pitaevskii	15
2.2	One-dimensional system	16
2.2.1	Gross-Pitaevskii equation in 1D	16
2.2.2	Long range order	17
2.2.3	Superfluidity	18
2.3	Dimensionless equations	19
2.4	Exact solvable models	21
2.4.1	Tonks-Girardeau (TG) gas	21
2.4.2	Lieb-Liniger model	23
2.5	Solitons	25
2.6	MCTDH/MCTDHB - Theory behind Qiwib	27
2.6.1	Finite basis-set expansion	28
2.6.2	Variationally optimised basis - MCTDH	29
2.6.3	MCTDHB/Qiwib	30
3	Bright soliton scattering with Gross-Pitaevskii	37
3.1	Introduction to the problem	38
3.2	Phenomenology of soliton scattering by a quantum well	39
3.3	Variational analysis	49
3.3.1	Two-mode model	49
3.3.2	Numerical results	52

CONTENTS

3.4	The trapping process	56
3.4.1	Analytical model	56
3.4.2	Temporal trapping	63
3.5	Probing energy levels	66
3.6	Summary	70
4	MCTDH - simple improvements due to rescaling of the interaction	71
4.1	Convergence studies	72
4.1.1	Discussion on CPU times	75
4.1.2	Convergence with respect to the number of single-particle functions	76
4.1.3	Convergence with respect to the number of grid points	78
4.1.4	Convergence with respect to the width of the interaction potential	78
4.1.5	Conclusion	79
4.2	Rescaling of the interaction	79
4.2.1	Theoretical background	79
4.2.1.1	Two particles on a ring	80
4.2.1.2	Empirical rescaling	83
4.2.1.3	Connection to T matrix renormalisation	84
4.2.1.4	MCTDH	85
4.2.2	Bosons in a ring	85
4.2.3	Bosons in a harmonic potential	89
4.2.4	Bosons in a double well	91
4.3	Summary	94
5	Full quantum dynamics of soliton scattering	97
5.1	Introduction to the problem	98
5.2	Two-mode MCTDHB model	99
5.2.1	TRL window for the second bound state	102
5.2.2	$NOON$ -like superposition states inside the RT window	102
5.3	Multi-mode MCTDHB models	104

5.3.1	<i>TRL</i> windows for the two-mode MCTDHB	105
5.3.2	Loss of coherence for multi-mode systems	109
5.4	Convergence properties	114
5.4.1	Motivation	114
5.4.2	Discussion	117
5.5	Summary	121
6	Conclusions and Outlook	125
6.1	Conclusions	125
6.2	Outlook	127
Appendix		129
A Robust mesoscopic superposition of strongly correlated ultracold atoms		
- an application of the rescaling method		129
A.1	Motivation	129
A.2	Results	130
A.3	Particle loss	133
A.4	Summary	134
B Numerical methods		137
B.1	Wave propagation	137
B.2	Imaginary time propagation	140
B.3	Numerical implementation of QiwiB	141
B.3.1	Single-particle functions	141
B.3.2	Propagation of prefactor \vec{C}	141
B.3.3	Improved relaxation	142
B.3.4	Implementation of the whole propagation scheme	143
B.3.5	Calculation of $\mathbf{H}_{\vec{C}}$ and the mean fields $\rho_{\mathbf{kq}}$ and $\rho_{\mathbf{k}sq\mathbf{l}}$	144
B.3.6	Transformation to natural orbital basis	145
C QiwiB - Influence of N and M on CPU times		147

CONTENTS

D The QiwiB program package	151
D.1 Background	151
D.2 Summary of key features	152
D.3 Examples	154
D.3.1 Particles in a well	154
D.3.2 Travelling bright soliton	158
Bibliography	164

List of Figures

1.1	Transition to a BEC.	2
1.2	Bright and dark soliton.	4
3.1	Sketch of a soliton moving towards a well.	38
3.2	GP results R and T vs velocity.	40
3.3	GP results for R , T , L vs potential depth.	43
3.4	Density at $V_0 = 5.2$ and $t = 77$ (full trapping) and $V_0 = 6.5$ and $t = 65$ (partial trapping).	44
3.5	Time evolution of the density for the cases of full trapping, reflection and transmission as well as partial trapping.	45
3.6	Comparing L (GP) and $N_{L,rel}$ (time-independent GP) for different well widths.	47
3.7	T from GP calculations compared to exact one-body results for increasing $v_{initial}$	48
3.8	Phase difference $\Delta\Phi$ from two-mode model.	52
3.9	R , T , L from the two-mode model.	53
3.10	Time evolution of the density in the two-mode model for the cases of full reflection, trapping, transmission as well as partial trapping.	55
3.11	T vs kinetic energy from GP calculations.	57
3.12	Time evolution of the kinetic and interaction energies for the transmitted part of the soliton from GP results at $V_0 = 4.9$ and $V_0 = 5.1$	58
3.13	Logarithmic density plot of the condensate for different times at $V_0 = 4.9$. A reflected component (radiation) is clearly visible.	59
3.14	Logarithmic density plot of the condensate for different times at $V_0 = 5.1$. Compared to Fig. 3.13 the reflected part is clearly larger.	59
3.15	Time evolution of the kinetic and interaction energies for the reflected part of the soliton from GP results at $V_0 = 4.9$ and $V_0 = 5.1$	60
3.16	Maximal possible trapping vs initial velocity.	61
3.17	Time evolution of the density at $V_0 = 5.182$ ($T \approx 1$) and $V_0 = 5.183$ ($L \approx 1$).	63

LIST OF FIGURES

3.18	Temporary trapping time for the soliton compared to exact one-body results.	64
3.19	Time evolution of the density for temporary trapping.	65
3.20	Number of trapped atoms N_L vs chemical potential μ from GP calculations compared with time-independent GP results.	68
3.21	Number of trapped atoms N_L vs chemical potential μ from GP calculations compared to the location of linear bound states.	69
4.1	Total CPU time vs number of single-particle functions and number of grid points.	73
4.2	Relative energy difference different numbers of single-particle functions.	75
4.3	Relative energy difference for different numbers of grid points.	77
4.4	Relative energy difference for different widths of the Gaussian-shaped interaction potential.	79
4.5	MCTDH results for the ground state energy vs interaction strength for the two bosons in a ring.	80
4.6	Relative energy difference vs interaction strength before and after rescaling.	86
4.7	Density-density correlation function for 5 particles in a ring for different interaction strengths.	88
4.8	Maximal relative deviation of the energy after rescaling from the exact result E_{LL} over the range of interaction strengths $0 < g < \infty$	89
4.9	Density function for 5 particles in a harmonic well for different interaction strengths.	90
4.10	Ground- and excited-state energies for two particles in a harmonic well compared to exact results.	91
4.11	Excited-state energies for two particles in a harmonic well compared to exact results in the TG limit.	93
5.1	R, T, L for the TRL window for different particle numbers.	100
5.2	R, T, L for the RT window for different particle numbers.	101
5.3	Density, natural orbitals and the state populations in the natural orbital basis for $N = 80, M = 2$ and $V_0 = 4.85$ as well as $V_0 = 4.864$	103

5.4	<i>R, T, L</i> for the <i>TRL</i> window for $N = 120$ and different numbers of single-particle functions.	106
5.5	<i>R, T, L</i> for the <i>TRL</i> window for $N = 10$ and different numbers of single-particle functions.	107
5.6	Time evolution of the density and the natural orbitals at $t = 150$ for $N = 10$, $M = 8$ and $V_0 = 4.88$	108
5.7	Time evolution of the density and natural orbital populations for $N = 10$, $M = 8$ and $V_0 = 4.84$	109
5.8	Time evolution of the density and natural orbitals for $N = 120$, $V_0 = 6.5$ and $M = 2$ as well as $M = 4$	110
5.9	Reflected soliton density for <i>NOON</i> and mixed state.	111
5.10	Time evolution of the one-body density matrices at different times for $N = 120$, $V_0 = 6.5$ and $M = 2$ as well as $M = 4$	113
5.11	Time evolution of the density and the natural orbital populations for $N = 80$, $M = 2$ and $V_0 = 4.82$	115
5.12	Maximal natural orbital populations for different particle numbers and their respective maximal feasible number of single-particle functions.	118
5.13	Time evolution of the density and the natural orbital populations at $t = 150$ for $N = 1000$, $M = 3$ and $V_0 = 4.848$	123
6.1	Outlook: Collision of two solitons in a <i>NOON</i> state.	127
A.1	Sketch of rotating bosons in a ring stirred by an external potential.	130
A.2	Energy level splitting vs interaction strength and total momentum state occupation numbers in the non-interacting regime and for the TG limit.	132
A.3	The superposition quality after particle loss vs interaction strength.	135
C.1	Total CPU time vs number of particles for QiviB calculations.	148
C.2	Total CPU time vs number of single-particle functions for QiviB calculations.	149

LIST OF FIGURES

- D.1 Original *Octave* picture of the density at $t = 3.79$ for 20 particles in a harmonic well for QiviB calculations. 155
- D.2 Original *Octave* picture for the reduced one-body density matrix of 20 particles in a harmonic well for QiviB calculations. 157
- D.3 Original *Octave* picture for the time evolution of the density with 20 particles in a harmonic well for QiviB calculations. 159

List of Tables

5.1	Natural orbital populations for $N = 80$ and $M = 2 \dots 4$ at $V_0 \approx 4.82$ at $t \approx 60$	116
5.2	Maximal natural orbital populations for $N = 10 \dots 10000$ and $M =$ $2 \dots 8$ inside the RT window.	119

LIST OF TABLES

List of abbreviations

General abbreviations

BEC	Bose-Einstein condensate
GP	Gross-Pitaevskii
GPE	Gross-Pitaevskii equation
1D	one dimension or one-dimensional
NOON	NOON state: superposition of N particles occupying the first natural orbital and N particles occupying the second one, i.e. $\alpha N, 0\rangle + \beta 0, N\rangle$ with α and β being complex numbers.
MCTDH	Multiconfigurational time-dependent Hartree
MCTDHB	Multiconfigurational time-dependent Hartree explicitly optimised for bosonic symmetry
MCTDH(B)	MCTDH and/or MCTDHB
Qiwib	Quantum integrator with interacting bosons, a program package developed for this thesis, which solves the MCTDHB equations
TG	Tonks-Girardeau
LL	Lieb-Liniger
RK	Runge-Kutta

Physical observables and operators

T	Transmission, i.e. in this thesis the relative number of particles that passed the well
R	Reflection, i.e. in this thesis the relative number of particles that got reflected from the well
L	Trapping, i.e. in this thesis the relative number of particles that got trapped inside the well
TRL	TRL window: range of potential depths around the resonance with a bound state of the well and where the reflection is less than one.

LIST OF ABBREVIATIONS

RT	RT window: range of potential depths between a regime of full reflection and full transmission
N	number of particles
M	number of single-particle functions, equivalent to the number of natural orbitals
N_g	number of grid points for the discretised spatial coordinate in the numerical calculations
$\psi(x, t)$	Gross-Pitaevskii wave-function in one dimension
$\Psi(x_1, \dots, x_N, t)$	Total wave function for N particles in one dimension
$ \Psi(t)\rangle$	Total wave function for N particles in second quantised form
g	dimensionless effective interaction strength in one dimension
μ	chemical potential
$\rho(x, y, t)$	Reduced one-body density matrix given as $\rho(x, y, t) = N \int dx_2 \dots dx_N \Psi^*(x, x_2 \dots, x_N) \Psi(y, x_2 \dots, x_N)$
ϕ_i	i th single particle function
ϕ_i^{NO}	i th natural orbital defined by $\rho(x, y, t) = \sum_{i=1}^M \rho_i [\phi_i^{NO}(y)]^* \phi_i^{NO}(x)$
ρ_{kq}	Density matrix in single-particle representation defined by $\rho(x, y, t) = \sum_{k,q=1}^M \rho_{kq} \phi_k^*(y) \phi_q(x)$
ρ_i	Density matrix in natural-orbital representation defined by $\rho(x, y, t) = \sum_{i=1}^M \rho_i [\phi_i^{NO}(y)]^* \phi_i^{NO}(x)$
$ \vec{n}\rangle$	many-body state in second quantisation: $ \vec{n}\rangle = \prod_{k=1}^M \frac{1}{\sqrt{n_k!}} [b_k^\dagger(t)]^{n_k} \text{vac}\rangle$ with $\vec{n} = (n_1, \dots, n_M)$ and $\sum_{i=1}^M n_i = N$
$C_{\vec{n}}$	Configuration amplitude defined by $ \Psi(t)\rangle = \sum_{\vec{n}} C_{\vec{n}} \vec{n}\rangle$ in the single-particle representation
$C_{\vec{n}}^{NO}$	Configuration amplitude defined by $ \Psi(t)\rangle = \sum_{\vec{n}} C_{\vec{n}}^{NO} \vec{n}\rangle$ in the natural-orbital representation

Physical constants

\hbar	Planck's constant $\hbar = 1.054571726(47) \times 10^{-34} J s$
k_b	Boltzmann constant $k_b = 1.3806488(13) \times 10^{-23} J/K$

*Your work is to discover your
world and then with all your
heart give yourself to it.*

Buddha



Introduction

1.1 Background and motivation

Bose-Einstein condensate (BEC)

All matter in our universe consists of two elementary types of particles, characterised by half-integer spin and integer spin, which are called fermions and bosons, respectively. Bosonic systems obey the Bose-Einstein statistics, where it is possible that an arbitrary number of particles can occupy the same quantum state. Fermions, however, are subject to the Pauli exclusion principle, which states that two fermions cannot occupy the exact same quantum state, and therefore they are described by the Fermi-Dirac statistics. This essential difference leads to contrasting many-body properties. Experimentally, condensation of a gas of bosons occurs when the average number of particles confined in a cube of the de Broglie wave length exceeds about three, and therefore the phase space density becomes larger than $\sim \hbar^{-3}$ (see Sec. 2.1.1 of this thesis). This can be achieved by lowering the temperature of the gas. Such behaviour was first predicted in 1924 by Einstein [1, 2] based on previous work by Bose [3], and therefore the effect was named Bose-Einstein condensation. After this discovery, it was found that physical phenomena, such as superconductivity and the superfluidity of liquid helium, are related to Bose-Einstein condensation. However, for the latter, due to strong inter-particle interactions, the condensate fraction contributes only $\sim 10\%$ to the total particle number, and therefore the effect of condensation is only one of many

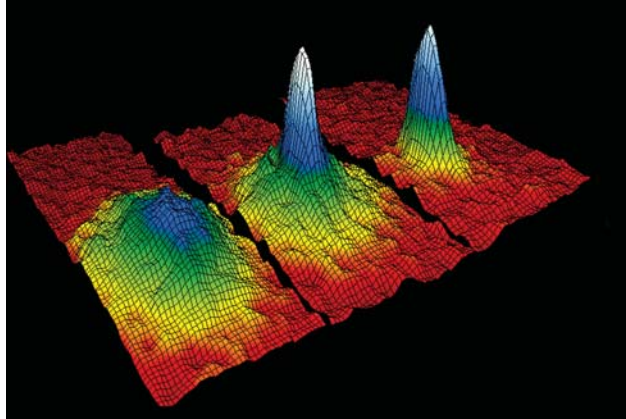


Figure 1.1: Picture of a BEC confined in a harmonic trap. The three pictures show the transition from a thermal gas for high temperatures (left) to an emerging condensate below a critical temperature being surrounded by a thermal cloud of atoms (middle), and the final condensate at very low temperatures (right) (picture is provided by NIST/JILA/CU-Boulder and is in the public domain).

others in such a system. To create a gas of bosons with most of the particles in the condensate state lower temperatures and lower densities were needed. This closer resembles the system of non-interacting bosons, for which Einstein originally predicted the condensation. New developments and ideas in laser technology led to the ways of how to cool down atoms with laser light [4]. These works resulted in first experiments on trapping and cooling atoms, and for their outstanding contributions in this field, Chu, Cohen-Tannoudji and Phillips received the Nobel Prize in physics in 1997. But it was not until 1995 when Cornell and Wieman created the first BEC with ^{87}Rb atoms [5] (see Fig. 1.1), shortly before Ketterle realised his BEC of ^{23}Na atoms [6]. The latter is also known for his interference experiments of two colliding condensates to investigate coherence effects [7]. All three were awarded the Nobel prize in physics in 2001 for their inspiring works on ultracold atoms.

Since then, an outburst of new developments, ideas and investigations led to much new and exciting research on ultracold gases. Particularly, the experimentally long coherence lengths (typically exceeding the system size) and the superfluid characteristics of a condensate made it a playground for scientists to observe the quantum nature of matter on a macroscopic level. In BECs those quantum ef-

fects are greatly enhanced because of its very low temperatures, and therefore condensates allow for direct studies of quantum phenomena.

In recent experiments and theoretical studies, atoms were trapped in optical lattices to model solid-state systems [8–11]. By increasing the scattering length, which describes the interaction between the particles, and which can be tuned very accurately by external magnetic fields, the superfluid to Mott insulator transition was extensively studied [12, 13]. Moreover, the technology used for cooling down bosons enabled the creation of degenerate ultracold Fermi gases as well [14–17]. The transition of weakly interacting fermions, described by the BCS theory [18], to a strongly interacting regime, in which pairs of fermions create a molecular BEC, were now accessible for experiments [19]. Furthermore, the possibility of creating macroscopic superposition states with cold atoms shows a potential use for the field of quantum information and to perform precision measurements [20–31].

One-dimensional BEC and solitons

Theoretically and experimentally, low-dimensional quantum gases are particularly interesting [32, 33]. We previously mentioned fermions and bosons as the two elementary types of particles in our universe. This is only fully true for three dimensions. For lower dimensions, however, the distinction between both particles gets blurred [34]. For instance, the statistics for the generalised particles found in two dimensions, which are called anyons, is a combination of fermion and boson statistics [35]. Furthermore, in the regime of large interactions the bosons form regular lattices similar to how fermions would crystallise [36, 37]. Therefore, a strong confinement of the particles in one or two dimensions to reduce the dimensionality of the system results not only in interesting new phenomena but its reduced complexity also allows for analytical studies [36, 38, 39]. Theoretical results for systems in three spatial dimensions are usually cumbersome to obtain, and often lack accuracy due to the approximations being used [40–44]. Considering one-dimensional systems, however, a number of analytical solutions for the many-body problem were derived, in particular for the Tonks-Girardeau gas of strongly interacting particles [36] and the Lieb-Liniger gas of bosons in a one-dimensional ring [38, 39] (see Sec. 2.4). Those theories provide exact results and therefore can

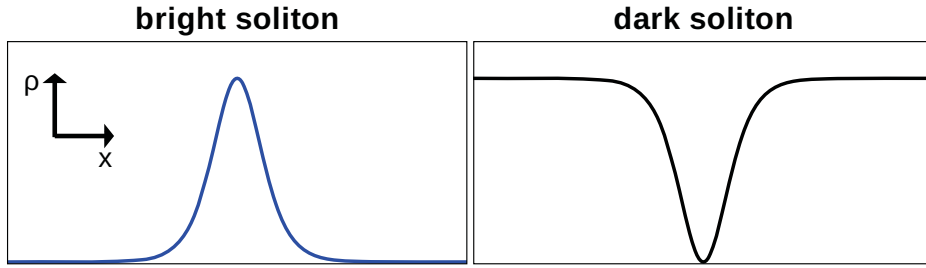


Figure 1.2: Densities $\rho(x)$ for a bright and a dark soliton. The former manifests itself as a peak in one spatial dimension (x -axis) while the latter is a dip on a bright background.

be used to gauge the accuracy of numerical calculations.

To model a three-dimensional BEC, the nonlinear Gross-Pitaevskii equation, which describes particles interacting with a mean field created by all particles combined, provides a lowest order approximation of the full many-body problem [45, 46]. Even though, in one-dimensional systems, for many cases a BEC strictly does not exist, the bosonic cloud can be described as a quasi-condensate, which behaves similar to a BEC but on a finite scale in the spatial coordinate [46] (see Sec. 2.2.2 in this thesis for details). This justifies the reduction of the Gross-Pitaevskii theory to a one-dimensional analogue [46].

Of particular interest for us are solitons. They are non-spreading isolated (solitary) waves, which emerge from collisions unchanged, and can travel for large distances without changing their shape or properties. Mathematically, they are solutions of several types of nonlinear equations and discussed in more detail in Sec. 2.5. Nonlinear equations describe many different problems, and therefore soliton solutions can be, amongst others, found in water waves, cloud formations [47] and fibre optics [48]. Since the one-dimensional Gross-Pitaevskii equation is a nonlinear equation as well, some of its exact solutions are identified as solitons. In this thesis we are interested in solitons in BECs, that are therefore referred to as BEC solitons or matter-wave solitons. Two types of matter-wave solitons can analytically be derived: Dark solitons and bright solitons. Their names originate from observations of optical solitons, as shown in Fig. 1.2, where the dark soliton is a dark localised spot on a bright background, and a bright soliton is bright localised

peak on a dark background. In this thesis we focus on bright matter-wave solitons. A well-known property of solitons is that they behave in many respects as classical particles do, e.g. with respect to their collisional properties or their motion in a slowly-varying external potential [49]. Recently, experimental progress made it possible to create matter-wave solitons and to explore their properties [50–52].

Soliton scattering in a BEC

The importance of soliton physics in other areas of physics [53–56] has motivated a large number of scientists to investigate the scattering of solitons on different kinds of potentials, like barriers or impurities [28, 29, 57–61], wells [62–66], steps [67–69] and a potential ramp [70]. In this thesis, we focus on the quantum well, for which we can derive exact results for the one-particle Schrödinger equation and find the discrete energy spectrum of linear bound states.

Those bound states are different to the problems in our classical world, where a particle always either reflects from a barrier or passes over it once the particle’s kinetic energy exceeds a certain threshold. Therefore, it always passes a negative barrier, i.e. a well. However, in quantum physics this is not the case anymore [71]. Particles can now be described as waves and their scattering properties depend on scattering amplitudes and probabilities. Quantum particles are found to partially reflect from a well, depending on the resonance of its energy with (quasi-) bound states of the well.

Going one step further, interactions between the particles turn the previously one-body problem into a many-body problem of much greater complexity. Therefore, BECs experience nonlinear mean-field interactions, which present a complication in the experiments [72, 73]. However, due to the collective behaviour in BECs, Pasquini et al. [74, 75] found experimentally that Bose-Einstein condensates can be reflected from a surface in spite of mostly attractive atom-surface interactions. While this shows the similarity to single-particle quantum physics, the nonlinear interactions might result in effects that are not observable in non-interacting systems.

In the case of matter-wave solitons, it was previously shown that they may experience “quantum” reflection from a potential well and yet maintain their particle-

like state to a large degree [66]. In addition to such nonlinear wave effects, macroscopic quantum tunnelling, fragmentation and superposition states were recently discussed as well [28–30, 76, 77].

In this thesis, we show that a soliton can also be permanently trapped inside the well, which was to our knowledge an effect not understood before. Similar to resonant effects for repulsive condensates scattered on a double barrier potential [78, 79], we find a population transfer between the soliton and nonlinear bound states of the potential well. This resonant process, together with loss of atoms in the form of “radiation”, slows down the soliton to form a stationary soliton bound to the well.

Full quantum many-body approach

Understanding the complexities of many-body quantum physics remains a grand challenge, in particular when it comes to excited states and dynamical problems. Systems of ultracold atoms can now be prepared with few to millions of particles and the experimental control over interactions, system size, and quantum states is rapidly improving [12, 80, 81].

Since its first appearance, the mean field Gross-Pitaevskii method was very successful in describing effects found for condensates of a very large number of bosons. However, few-particle systems, strongly interacting regimes, high densities or quantum phenomena, such as entanglement, are not accessible with the Gross-Pitaevskii method, and therefore more complicated methods involving full many-body physics have to be used. Nowadays, a considerable amount of research focuses on the creation of entanglement in ultracold atomic systems, which requires calculations at a single particle level. Methods based on fixed basis set expansions with Wannier functions describing an optical lattice, which leads to the Bose-Hubbard model [8], and with harmonic oscillator eigenfunctions [82] or a plane-wave basis [83, 84] for trapped systems were extensively used. Methods like time-evolving block decimation [85] and time-dependent density matrix renormalisation [86, 87] exploit spatial entanglement properties to allow for time-dependent simulations of larger multi-particle problems. However, these approaches are limited by accessing only a finite Hilbert space.

For the research presented in this thesis we focus on two other methods, the so-called multiconfigurational time-dependent Hartree (MCTDH) method [88–91] and a variation of it, which was tailored for purely bosonic systems and is called the MCTDHB method [92, 93]. A finite basis set expansion is used again to describe the full quantum many-body state. However, the basis functions are now time-dependent and always variationally optimised. In this thesis we show that this method is now capable of describing quantum phenomena, such as superposition states and entanglement. Compared to the Gross-Pitaevskii results, this leads to new interesting effects, in particular the creation of macroscopic binary superposition states, so-called *NOON* states. For this, we developed QiwiB (quantum integrator with interacting bosons), a program package solving the non-trivial MCTDHB equations. It is a major open source project and a part of this thesis.

Research based on these methods could potentially lead to real-world applications of nonlinear-wave scattering. Although the current work addresses matter-wave solitons in particular, our findings are also applicable to nonlinear optics or other nonlinear wave problems governed by the many-body Schrödinger equation.

1.2 Outline of this thesis

Starting with the second chapter, an introduction to general Bose-Einstein theory is presented as well as more specific topics that are relevant to this thesis. The one-dimensional Gross-Pitaevskii equation for zero temperature and its bright soliton solutions are discussed in sections 2.1, 2.2 and 2.5. Furthermore, in Sec. 2.4 exact models for the full many-body problem, namely the Lieb-Liniger model for bosons in a ring and the Tonk-Girardeau gas for strongly interacting particles, are introduced, while Sec 2.6 presents an introduction to the MCTDH and MCTDHB approaches.

In chapter 3 we present the soliton scattering problem within the Gross-Pitaevskii approach. In Sec. 3.1 and 3.2 we introduce the problem and show that the final wave function exhibits different regimes of reflection, transmission and trapping. The latter deserves special attention as it is an exciting effect not known from exact single-particle solutions. The variational two-mode model in Sec. 3.3 and analytical work on the dynamics of trapping in Sec 3.4 show the underlying mechanism

CHAPTER 1. INTRODUCTION

of resonant energy transfer and radiation. We furthermore suggest a method to probe energy levels from a potential of unknown shape.

To extend the calculations from the second chapter to the MCTDHB many-body approach, studies on the properties of the MCTDH/MCTDHB expansion with their advantages and, more importantly, their limitations are discussed in chapter 4. The studies in Sec. 4.1 show that the convergence with the size of the truncated Hilbert space is extremely slow. Therefore, numerically feasible calculations are limited to small Hilbert spaces, which leads to errors in the energy spectrum and density distributions. However, in Sec. 4.2.1 we introduce a very valuable correction to this expansion in the form of a rescaling formula for the interaction strength. The last parts of this chapter present evidence that this rescaling significantly improves the results by testing our approach on three examples, i.e. for bosons in a ring as well as bosons confined in a harmonic and a double-well trap.

Chapter 5 combines the knowledge of the previous two chapters by presenting full quantum many-body calculations for the soliton scattering problem. We discuss the creation of fragmented states and *NOON* states, and their dependence on the potential depth. In contrast to previous studies on superpositions of counter-propagating solitons, we present a novel superposition of one soliton being reflected from the well and the other one being trapped. We demonstrate that this case is observable for all particle numbers, and therefore we expect them to be achievable in experiments. Furthermore, we discuss convergence properties of our results and the MCTDHB method in general.

In the appendix we present work on the creation of robust superpositions in a system of several bosons confined to a one-dimensional ring. To improve its results, the proposed rescaling scheme from chapter 4.1 was applied. Furthermore, the appendix discusses numerical implementations for Qiwib and analyses CPU times for different sets of parameters. We also included an overview of Qiwib, showcasing its features, numerical implementations, and present a quick introduction to its usage by discussing two example simulations.

1.3 Publications

Much of the work contained in this thesis has been published in three articles in *Physical Review A*. All the results from chapter 3 and Sec. 4.2 can be found in Ref. [94] and Ref. [95], respectively. Furthermore, the research presented in App. A was published before in Ref. [84]. In addition, the QiviB program was made public and can be downloaded freely from [96].

*He who loves practice
without theory is like the
sailor who boards ship
without a rudder and com-
pass and never knows where
he may cast.*

Leonardo da Vinci

2

Theoretical background

This chapter gives a brief introduction to the main theoretical topics, which are relevant for this thesis. In Sec. 2.1 we first cover the quantum statistics for cold bosons, introduce an approximate description of the physical particle interaction and derive the Gross-Pitaevskii (GP) equation as the lowest order approximation for an interacting gas of bosons. This is followed by a discussion of one-dimensional systems and how low dimensionality affects the BEC properties of superfluidity and long-range order. For this thesis, we conveniently introduce dimension-less equations and observables in Sec. 2.1, and later present exact results for one-dimensional many-body systems. In Sec. 2.5 the mathematics of solitons as solutions of nonlinear equations, in particular the GP equation, are shown. Finally, the last section discusses the multiconfigurational time-dependent Hartree (MCTDH) method and the multiconfigurational time-dependent Hartree for bosons (MCTDHB) approach. They are both full many-body theories that go beyond the GP method to simulate the full multiple-particle quantum problem.

2.1 Simple theories on Bose-Einstein condensates

2.1.1 The ideal gas

Consider an ensemble of non-interacting bosonic atoms propagating freely in space. Even in this simple case, it is possible to reach a regime for Bose-Einstein condensation.

CHAPTER 2. THEORETICAL BACKGROUND

Assume a uniform gas of bosons of mass m that is in equilibrium with temperature T . From popular text books [45, 46, 97] we find that there exists a critical temperature $T_c = \frac{2\pi\hbar^2}{k_b m} \left(\frac{n}{\zeta(3/2)} \right)^{\frac{2}{3}}$ below which we obtain a macroscopic population of the single-particle ground state of the system. Here, \hbar is Planck's constant, k_b the Boltzmann constant and ζ the Riemann zeta function. The condensate fraction for an atomic gas of density n is given by

$$n_0 = n \left[1 - \left(\frac{T}{T_c} \right)^{\frac{3}{2}} \right]. \quad (2.1)$$

Compared to the uniform case, a confinement leads to a larger increase of n_0 when decreasing the temperature. To find a physical meaning for the condensation process we take a look at the de Broglie wavelength for bosons $\lambda_{dB} = \sqrt{\frac{2\pi\hbar^2}{mk_b T}}$. At $T < T_c$ we find

$$\lambda_{dB}^3 n > \zeta \left(\frac{3}{2} \right) \approx 2.612. \quad (2.2)$$

Therefore the Bose-Einstein condensation can occur if the quantum-nature length scale λ_{dB} is of the same order as the separation between the particles $\sim 1/n^{1/3}$. For the typical momentum of a particle given by $\sim (k_b T m)^{1/2}$, this corresponds to a critical phase space density of $\sim \hbar^{-3}$. At this critical point, the wave packets start to overlap and to behave coherently.

2.1.2 Interactions

In the previous section it was shown that interactions between bosons are not necessary for the formation of a condensate. However, in reality particles are always interacting due to Coulomb interaction, Van-der-Waals interaction, dipole interactions and many more. In order to find an appropriate model for the physical interaction potential all possible types of interactions have to be considered. This is, however, computationally not feasible. In scattering theory for two weakly interacting bosons a Born expansion of the finite range interaction potential leads to a form of the final wave-function where the scattering amplitude does not depend on the interparticle distance anymore. Low temperatures in BECs lead to small kinetic energy of the particles, and therefore the scattering amplitude is ap-

2.1. SIMPLE THEORIES ON BOSE-EINSTEIN CONDENSATES

proximately constant [32]. The total cross section for two bosons is then given by [46]

$$\sigma = 8\pi a_s^2. \quad (2.3)$$

The scattering length a_s depends on the atomic species but can be determined very accurately in experiments. For a detailed derivation the reader is referred to the books of Pethick and Smith [45] and Pitaevskii and Stringari [46].

In the limit of low densities, the exact interaction potential is replaced with a regularised pseudo-potential which maintains the same scattering properties as the real one. The most common choice is given by [98, 99]

$$V(\vec{r}_1, \vec{r}_2) = V(r_{12}) = g_{3D} \delta^{(3D)}(r_{12}) \frac{\partial}{\partial r_{12}} r_{12} \quad (2.4)$$

with $r_{12} = |\vec{r}_1 - \vec{r}_2|$, the three-dimensional interaction strength $g_{3D} = \frac{4\pi a_s \hbar^2}{m}$ and the three-dimensional delta potential $\delta^{(3D)}$. For the work presented in this thesis this approximation is sufficient. But we also note that there are other cases involving higher energies where it is recommended to include higher order scattering, i.e. d-wave scattering [100].

2.1.3 Gross-Pitaevskii equation

There are different approaches to derive the equation of motion for N Bose-condensed particles. For convenience only one of them is shown here (see Ref. [46] for further details). The three-dimensional many-body Hamiltonian for interacting particles in second quantisation has the following form

$$\begin{aligned} \hat{H} = & \int d^3\vec{r} \hat{\Psi}^\dagger(\vec{r}, \tau) H_0 \hat{\Psi}(\vec{r}, \tau) \\ & + \frac{1}{2} \int d^3\vec{r}_1 \int d^3\vec{r}_2 \hat{\Psi}^\dagger(\vec{r}_1, \tau) \hat{\Psi}^\dagger(\vec{r}_2, \tau) V_{\text{int}}(\vec{r}_1, \vec{r}_2) \hat{\Psi}(\vec{r}_2, \tau) \hat{\Psi}(\vec{r}_1, \tau) \end{aligned} \quad (2.5)$$

with the single-particle Hamiltonian $H_0 = (\hbar^2/2m)\Delta_{\vec{r}} + V_{\text{ext}}(\vec{r}, \tau)$ and the interatomic interaction potential $V_{\text{int}}(\vec{r}_1, \vec{r}_2)$. Here \vec{r} is a three-dimensional vector determining the spatial position and τ is the time. The creation and annihilation

CHAPTER 2. THEORETICAL BACKGROUND

operators for bosons, $\hat{\Psi}$ and $\hat{\Psi}^\dagger$, satisfy the usual commutation relations for bosons

$$[\hat{\Psi}(\vec{r}_1, \tau), \hat{\Psi}^\dagger(\vec{r}_2, \tau)] = \delta(\vec{r}_1 - \vec{r}_2), \quad [\hat{\Psi}(\vec{r}_1, \tau), \hat{\Psi}(\vec{r}_2, \tau)] = [\hat{\Psi}^\dagger(\vec{r}_1, \tau), \hat{\Psi}^\dagger(\vec{r}_2, \tau)] = 0$$

We further replace V_{int} with Eq. (2.4). Substituting Eq. (2.5) into the Heisenberg equation of motion for the operator $\hat{\Psi}$ gives

$$i\hbar \frac{\partial}{\partial \tau} \hat{\Psi}(\vec{r}, \tau) = [\hat{\Psi}(\vec{r}, \tau), \hat{H}] \quad (2.6)$$

$$= \left[\hat{H}_0 + V_{\text{ext}}(\vec{r}, \tau) + g_{3D} \hat{\Psi}^\dagger(\vec{r}, \tau) \hat{\Psi}(\vec{r}, \tau) \right] \hat{\Psi}(\vec{r}, \tau). \quad (2.7)$$

The operator $\hat{\Psi}$ can be expanded for a basis of single-particle functions ϕ_i , given by

$$\hat{\Psi}(\vec{r}, \tau) = \sum_i \phi_i(\vec{r}, \tau) \hat{a}_i(\tau).$$

where \hat{a} annihilates a particle in state i . For a BEC, only one single-particle function is macroscopically occupied, which we assume to be ϕ_0 . Therefore, to a good approximation, the operators \hat{a}_0 and \hat{a}_0^\dagger can be replaced by $\sqrt{N_0}$, where $\langle \hat{a}_0^\dagger \hat{a}_0 \rangle = N_0$ is the number of particles in state 0. Therefore, we find

$$\hat{\Psi}(\vec{r}, \tau) = \sqrt{N_0} \phi_0(\vec{r}, \tau) + \sum_{i \neq 0} \phi_i(\vec{r}, \tau) \hat{a}_i(\tau) \quad (2.8)$$

and to lowest order $\hat{\Psi}(\vec{r}, \tau) = \sqrt{N_0} \phi_0(\vec{r}, \tau) =: \psi(\vec{r}, \tau)$ [46]. This leads to the time-dependent Gross-Pitaevskii equation (TDGPE)

$$i\hbar \frac{\partial}{\partial \tau} \psi(\vec{r}, \tau) = \frac{\hbar^2}{2m} \Delta_r \psi(\vec{r}, \tau) + V_{\text{ext}}(\vec{r}, \tau) \psi(\vec{r}, \tau) + g_{3D} |\psi(\vec{r}, \tau)|^2 \psi(\vec{r}, \tau). \quad (2.9)$$

Assuming that the solutions are stationary and the only time dependence comes from a global phase then the wave function can be written as $\psi(\vec{r}, \tau) = |\psi(\vec{r})| \exp(\Theta \tau)$. A convenient choice of the phase is given by $\Theta = -\frac{i}{\hbar} \mu$ for the so-called chemical potential μ ¹. Inserting this ansatz into Eq. (2.9), we obtain the time-independent

¹This is strictly speaking only true for temperatures $T \ll T_c$, for which the depletion is negligible and the occupation of the order parameter is macroscopic. In these limits, μ can be identified with the true chemical potential which is then equal to the Hartree-Fock single-particle energy [32].

2.1. SIMPLE THEORIES ON BOSE-EINSTEIN CONDENSATES

Gross-Pitaevskii equation (GPE)

$$\mu\psi(\vec{r}) = \frac{\hbar^2}{2m}\Delta_{\vec{r}}\psi(\vec{r}) + V_{\text{ext}}(\vec{r}, \tau)\psi(\vec{r}) + g_{3D}|\psi(\vec{r})|^2\psi(\vec{r}). \quad (2.10)$$

The GPE is applicable to simulate experiments at temperatures T much smaller than the critical temperature T_c . Also, the particles should only interact very weakly so that the scattering length $a_s \ll \lambda_{dB}$ [46].

The Gross-Pitaevskii mean-field theory has been proven to successfully describe a large variety of experiments. However, the increased sensitivity and control of the experimental equipment has made it possible to study new phenomena for which a more advanced theoretical treatment is necessary.

2.1.4 Beyond Gross-Pitaevskii

In the last two decades, improvements and new theories have been developed to model systems beyond the limitations of the GPE. In this section we will briefly discuss two methods that have been shown to be successful in describing excitations and other features in ultracold gases that can not be seen by using the GP method.

Hartree-Fock Bogoliubov

Assuming that for a BEC the majority of particles occupy the same state, we can write the Bogoliubov ansatz [46]

$$\hat{\Psi}(r, \tau) = \psi(\vec{r}, \tau) + \delta\hat{\psi}(\vec{r}, \tau) \quad (2.11)$$

where $\psi(r, \tau)$ is the order parameter for the condensate and $\delta\hat{\psi}(r, \tau)$ describes the thermal and quantum fluctuations. For the bosonic operators \hat{c}^\dagger and \hat{c} , that create and annihilate non-interacting quasi-particles, we can use the ansatz $\delta\psi(\vec{r}, \tau) = \sum_j \left(u_j(\vec{r}, \tau)\hat{c}_j - v_j^*(\vec{r}, \tau)\hat{c}_j^\dagger \right)$ to obtain coupled equations for u and v , from which the non-condensed fraction of the gas can be determined. This approach also allows for finite temperature time-dependent calculations. The Hartree-Fock-Bogoliubov (HFB) method has been very successful in describing many-particle phenomena [40,101]. However, HFB is not quite consistent in the sense that it needs corrections

CHAPTER 2. THEORETICAL BACKGROUND

due to ultraviolet divergences. They arise because of the non-physical contact interaction potential that is being used. In addition, HFB demands a large number of particles to be valid and therefore can not be used for few-particle systems.

c-field method

Recently, c-field methods, or classical field methods, have risen in popularity. They share the same idea of describing the density operator with a quasi-probability function within a basis of coherent states. The exact knowledge of this function determines the system and its time-dynamics. In addition, the action of a quantum mechanical operator on the density operator can now be mapped to an action of a classical operator on the quasi-probability function [102]. Nowadays, the positive-P [103, 104] and the truncated Wigner methods (TWM) [105–107] find most attention and a huge development has happened recently which is expected to extend even further. In the TWM, it is numerically not possible to directly integrate the quasiprobability function. Therefore, a large number of different trajectories are calculated instead. The idea is that a finite number of those trajectories can accurately sample the Wigner function. The TWM is dynamically stable and gives remarkable results for a number of problems. However, it is not suitable to describe few-particle systems and their long-time dynamics considered in this thesis.

2.2 One-dimensional system

2.2.1 Gross-Pitaevskii equation in 1D

So far a fully three-dimensional theory to model an ultracold Bose gas has been introduced. However, for the course of this thesis we are interested in quasi-one-dimensional systems. They are characterised by a strong confinement in two transverse dimensions. In this situation the condensate is said to be frozen in the transversal plane as the energies of the particles are not sufficient to populate excited states in this direction. Therefore, the much weaker longitudinal confinement ensures that the dynamics of the system is restricted to this one di-

mension. Hence, an effective one-dimensional theory is expected to give accurate results as long as the temperature T is small. Further details can be found in Refs. [46, 108, 109]. The one-dimensional interaction potential is now given as $V(r_1, r_2) = V(|r_1 - r_2|) = g_{1D}\delta(|r_1, r_2|)$ [109] with an effective one-dimensional interaction strength $g_{1D} = 2\hbar a_s \omega_\perp$ and the delta function δ in one dimension. This leads to the 1D time-dependent GP equation which can now be written as

$$i\hbar \frac{\partial}{\partial \tau} \psi(z, \tau) = \left[-\frac{\hbar^2}{2m} \frac{\partial^2}{\partial z^2} + V_{1D}(z, \tau) + g_{1D} |\psi(z, \tau)|^2 \right] \psi(z, \tau) \quad (2.12)$$

for the GP wave-function $\psi(z, \tau)$ in longitudinal direction z and confined by the longitudinal potential $V_{1D}(z, \tau)$. In this particular case a transversal confinement with cylindrical symmetry $V_\perp(r) = \frac{1}{2}m\omega_\perp^2 r^2$ has been assumed. The normalisation of $\psi(z, \tau)$ is given by

$$\mathcal{N} = \int |\psi(z, \tau)|^2 dz$$

where \mathcal{N} can be chosen arbitrarily since the only relevant information is given by $g_{1D}\mathcal{N}$. In Sec. 2.3 we will show how to introduce a proper scaling to relate the normalisation to physical properties.

2.2.2 Long range order

Off-diagonal long-range order (ODLRO) of the reduced one-body density $n(\vec{r}, \vec{r}')$ is related to a BEC [46]. A particular set of single-particle functions, so called natural single-particle functions or orbitals, exists that satisfy $n(\vec{r}, \vec{r}') = \sum_i n_i \phi_i^*(\vec{r}) \phi_i(\vec{r}')$. For a BEC we find that $n_0 \sim N$ is the only large occupation number while the others are much reduced to $n_{i \neq 0} = \langle \hat{a}_i^\dagger \hat{a}_i \rangle \ll N$. According to Eq. (2.8) this leads to

$$n(\vec{r}, \vec{r}') = \langle \hat{\Psi}^\dagger(\vec{r}) \hat{\Psi}(\vec{r}') \rangle = N_0 \phi_0^*(\vec{r}) \phi_0(\vec{r}') + \sum_{i \neq 0} \phi_i^*(\vec{r}) \phi_i(\vec{r}') \langle \hat{a}_i^\dagger \hat{a}_i \rangle.$$

For a uniform gas the single-particle functions are simply plain waves $\phi_i(\vec{r}) = \frac{1}{\sqrt{V}} \exp(i\vec{p}_i \vec{r} / \hbar)$. Then the Fourier transform of Eq. (2.8) leads to

$$n(\vec{p}) = N_0 \delta(\vec{p}) + \dots$$

This delta function ensures that

$$n(\vec{r}, \vec{r}')_{|\vec{r}-\vec{r}'|\rightarrow\infty} = \frac{N_0}{V} \neq 0$$

approaches a non-zero value for $|\vec{r} - \vec{r}'| \rightarrow \infty$. This feature is known as ODLRO and arises solely due to a macroscopic occupation of a single state.

However, for one dimension this long-range order does not exist anymore. There one can find for $|z - z'| > \xi$

$$n(z, z') \propto \left(\frac{\xi}{|z - z'|} \right)^\nu \quad (2.13)$$

where $\xi = \sqrt{\frac{a_\perp^2}{8a_s n_1}}$ is the one-dimensional healing length that determines the length scale over which the condensate density changes. Furthermore n_1 is the one-dimensional density, a_s is the three-dimensional scattering length, $a_\perp = \sqrt{\hbar/(m\omega_\perp)}$ the transversal harmonic oscillator length and $\nu = 1/(\pi\sqrt{2n_1 a_\perp^2/a})$. The precondition $n_1 a_\perp / a_s \gg 1$ ensures that ν is small. This was seen in experiments, where $\nu \sim 10^{-3}$ [110]. Therefore, the long-range order does not vanish for finite distances much larger than the healing length. Strictly speaking, a BEC does not exist in one dimension but Eq. (2.13) still suggests a BEC-like state that is usually called quasi-BEC.

The derivation presented above assumes zero temperature. It should be noted that due to thermal fluctuations at finite temperature the long-range order is further reduced and destroyed for large temperatures. For the work presented in this thesis, however, we are only considering the zero temperature regime and therefore will not go into further detail here.

2.2.3 Superfluidity

Associated with the BEC is the effect of superfluidity, an unusual state of matter. Superfluids behave like fluids that can travel through guides without viscosity and energy dissipation. This makes them stable under rotation. For example, the rotational velocity of a gas flowing in a ring would be constant in time, i.e. there would be no existing friction to decelerate the gas. Landau derived criteria for the

2.3. DIMENSIONLESS EQUATIONS

existence of a superfluid [46, 111]. According to his results excitations can only occur if the velocity v of the superfluid relative to the stationary confinement is greater than some critical velocity v_c , i.e. the velocity of sound. It is given by

$$v < v_c = \min_p \frac{\epsilon(p)}{p}$$

where $\epsilon(p)$ is the energy of a single excitation. For an ideal gas $\epsilon(p) \propto p^2$, and therefore $v_c = 0$, i.e. no superfluid. However, for an interacting gas at zero temperature one can find, from the Bogoliubov spectrum for small momentum excitations,

$$v_c = \sqrt{\frac{ng}{m}}.$$

For one-dimensional systems the velocity of sound is given by

$$v_c = \frac{\hbar}{ma_{\perp}} \sqrt{2an_1}.$$

Clearly, at least for zero temperature, superfluidity arises due to the interactions between the particles. The situation changes for finite temperatures, but for the scope of this thesis we do not present a detailed discussion on this, and refer the reader to popular text books [45, 46].

The superfluid velocity is commonly given by

$$v_s(z, \tau) = \frac{\hbar}{m} \nabla \theta(z, \tau) \tag{2.14}$$

where θ is the phase of the superfluid order parameter $\psi(z, \tau) = |\psi(z, \tau)| \exp[i\theta(z, \tau)]$. Notice that the superfluid velocity defined in this fashion can be time-dependent and is generally not spatially constant.

2.3 Dimensionless equations

For convenience we would like to introduce equations and observables in dimensionless units. This is necessary to improve the accuracy in numerical simulation. Choosing an appropriate scaling, multiplications of numbers that differ in tens of

CHAPTER 2. THEORETICAL BACKGROUND

orders of magnitude can be avoided. First, we choose an arbitrary energy scale $\tilde{E} > 0$, the length scale \tilde{z} and the unit density \tilde{n} to introduce following dimensionless properties:

$$\begin{aligned} t &:= \tau/\tilde{t} \\ x &:= z/\tilde{z} \\ \psi(x) &:= \phi(x\tilde{z})/\sqrt{\tilde{n}} \\ E &:= \epsilon/\tilde{E} \end{aligned}$$

where the total energy is given by

$$\epsilon = \langle \hat{H} \rangle.$$

A convenient, but special choice for the natural energy unit is $\tilde{E} = \hbar^2/(m\tilde{z}^2) = \hbar^2/(ma_{\perp}^2) = \hbar\omega_{\perp}$, the energy scale of the transversal plane. The time scale is given by $\tilde{t} = \hbar/\tilde{E}$. Performing the adequate replacements in Eq. (2.12) we can rewrite the 1D Gross-Pitaevskii equation in dimensionless form, given by

$$i\frac{\partial}{\partial t}\psi(x, t) = \left[-\frac{1}{2}\frac{\partial^2}{\partial x^2} + g|\psi(x, t)|^2 + V(x) \right] \psi(x, t). \quad (2.15)$$

We have introduced $V(x) = V_{1D}(x\tilde{z})/\tilde{E}$ and the dimensionless coupling constant $g = g_{1D}\tilde{n}/\tilde{E}$. In addition, the normalisation of ψ , which is given by

$$\mathcal{N} = \int |\psi(x, t)|^2 dx, \quad (2.16)$$

relates to the physical number of particles N in the system by

$$N = \mathcal{N}\tilde{n}\tilde{z}.$$

The energy and length scales can typically be chosen to match certain system parameters. In the following section Sec. 2.5 we will give typical numbers for BEC solitons.

We will see for the case of the full MCTDH/MCTDHB many-body approach

that $\mathcal{N} = \int d\vec{r}_1 \dots d\vec{r}_N \Psi(\vec{r}_1, \dots, \vec{r}_N) = N$. Therefore we find $\tilde{n} = 1/\tilde{z}$. Hence, in MCTDHB we do not need the extra unit density but instead all properties can be made dimensionless with a natural energy \tilde{E} and natural length \tilde{z} . For the simulations described in chapter 3 and chapter 5 the natural scales are given in terms of the transversal scales, while in chapter 4 more convenient scalings are introduced.

2.4 Exact solvable models

A one-dimensional uniform gas of N bosons with a short-range interaction is described by a Hamiltonian of the following form:

$$H = - \sum_{i=1}^N \frac{\partial^2}{\partial x_i^2} + 2\gamma n_{1D} \sum_{i>j} \delta(x_i - x_j). \quad (2.17)$$

Here, γ is the Lieb-Liniger parameter, a dimensionless coupling strength, which is defined as $\gamma = c/n_{1D}$, where c is the interaction strength between the particles [38, 45]. Furthermore, $n_{1D} = N/L$ is the one-dimensional density for a system of length L . This system can be generally solved via a Bethe ansatz [112], which assumes a free particle solution except when two particles overlap. In this section we present two analytical models, one for a strongly interacting gas of bosons, the Tonks-Girardeau gas [36], and the other one for arbitrary interaction strengths, the Lieb-Liniger model [38].

2.4.1 Tonks-Girardeau (TG) gas

In the interaction-free case, $\gamma = 0$, the solutions to 2.12 are trivial and for many problems well known. For the other extreme case of very strong repulsive interactions $\gamma \rightarrow \infty$, a gas of bosons in one dimension at zero temperature can be described via the Tonks-Girardeau theory [36]. This particular case exhibits a very interesting behaviour. If the interaction is strong enough, the repulsion becomes so dominant that the particles can not pass each other anymore. This phenomenon is similar to a non-interacting Fermi gas confined to one dimension where the particles can not pass each other because of the Pauli exclusion principle.

CHAPTER 2. THEORETICAL BACKGROUND

Therefore, the full many-body wave-function should be

$$\Psi_{TG}(\dots, x_j, \dots, x_k, \dots) = 0 \text{ if } x_j = x_k. \quad (2.18)$$

In Ref. [36] a Bose-Fermi mapping procedure was proposed to describe the wave-function in the TG limit. A general ansatz to describe such a state preserving the bosonic symmetry is given by a Slater determinant, which solves the free particle equations. The full many-body wave-function is given by [45]

$$\begin{aligned} \Psi_{TG}(x_1, \dots, x_N) &= \Psi_F(x_1, \dots, x_N) \prod_{1 \leq s < t \leq N} \text{sign}(x_t - x_s) \\ &= \det \begin{vmatrix} e^{ik_1 x_1} & e^{ik_1 x_2} & \dots & e^{ik_1 x_N} \\ e^{ik_2 x_1} & e^{ik_2 x_2} & \dots & e^{ik_2 x_N} \\ \vdots & \vdots & & \vdots \\ e^{ik_N x_1} & e^{ik_N x_2} & \dots & e^{ik_N x_N} \end{vmatrix} \prod_{1 \leq s < t \leq N} \text{sign}(x_t - x_s) \end{aligned} \quad (2.19)$$

with $\text{sign}(|x|) = 1$ and $\text{sign}(-|x|) = -1$. Furthermore, Ψ_F describes the ground state of non-interacting fermions. This ansatz preserves the bosonic symmetry under particle exchange. Both, the Fermi gas and the TG gas have been shown to share the same expressions for the energy $E = \sum_{j=1}^N k_j^2$ and momentum $p = \sum_{j=1}^N k_j$, which is an indication that in one dimension fermions and bosons are not clearly distinguishable anymore. Therefore, the transition from a weakly to a strongly interacting TG gas is often called fermionisation. We note, however, that the smooth momentum distribution of a TG gas differ greatly from a step-like distribution in the fermionic case. This is related to the fact that two fermions are unable to occupy the same momentum state while bosons still can. Furthermore it can be shown that due to the different symmetry properties under particle exchange higher order correlation functions differ as well.

Assuming periodic boundaries to avoid problems with the system ends, the wave-function now satisfies

$$\Psi(\dots, x_i, \dots) = \Psi(\dots, x_i + L, \dots) \quad \forall i. \quad (2.20)$$

This leads to a discrete spectrum for the k_j , given by

$$k_j = \frac{2\pi}{L} n_j \left(\frac{N+1}{2} \right) \quad (2.21)$$

for any positive integer n_j . Minimising the energy yields the k_j for the TG ground-state wave-function, which is given by

$$\Psi_{TG}(x_1, \dots, x_N) = \frac{2^{N(N-1)/2}}{\sqrt{n!L^N}} \prod_{i<j} |\sin[\pi(x_i - x_j)/L]| \quad (2.22)$$

Analogous calculations can be done to calculate excited-state wave-functions and energies as well. In addition, the one-body density matrix

$$\rho(x, t) = \int dx_2 \int dx_3 \dots \int dx_N |\psi_{TG}(x, x_2, \dots, x_N, t)|^2 \quad (2.23)$$

and the reduced pair correlation function

$$g(0, x, t) = \int dx_3 \int dx_4 \dots \int dx_N |\psi_{TG}(0, x, x_3, x_4, \dots, x_N, t)|^2 \quad (2.24)$$

can then be calculated numerically, and for specific systems even analytically. In principle this holds for any arbitrary external potential.

Recent experimental progress in creating effectively one-dimensional systems made it possible to test the TG model and to prove the fermion-boson duality in lower dimensions [113, 114].

In chapter 4 we will make use of the TG approach to compare exact results with our numerical MCTDH results. This allows us to study the accuracy of MCTDH/MCTDHB. Furthermore the exact TG energy is used to extend the rescaling method in Sec. 4 to many-particle systems.

2.4.2 Lieb-Liniger model

Unfortunately, the Bose-Fermi mapping described in the previous section can not give us any information about finite values of the interaction $\gamma < \infty$. However, for the limiting case of vanishing external potential, which is similar to the physical

CHAPTER 2. THEORETICAL BACKGROUND

situation of bosons in a ring of length L , exact results can still be obtained. This system was first solved by Lieb and Liniger in 1963 [38]. For a complete derivation we refer to Refs. [38, 45, 112] and only present the results that are relevant for the thesis at hand. An analytical calculation for the two-body problem leads to the more general jump condition [45] for N particles

$$\left(\frac{\partial}{\partial x_j} - \frac{\partial}{\partial x_k}\right)\Psi|_{x_j=x_k+\epsilon} - \left(\frac{\partial}{\partial x_j} - \frac{\partial}{\partial x_k}\right)\Psi|_{x_j=x_k-\epsilon} = 2c\Psi|_{x_j=x_k} \quad (2.25)$$

with $\epsilon \rightarrow 0$. This equation has to be satisfied by a generalised form of the wavefunction in Eq. (2.19), which is given by

$$\Psi(x_1, \dots, x_N) = \mathcal{N} \sum_P (-1)^{[P]} \exp\left(i \sum_{i=1}^N k_{P_i} x_i\right) \prod_{j<l} [k_{P_j} - k_{P_l} - ic \text{sign}(x_j - x_l)] \quad (2.26)$$

with the normalisation \mathcal{N} . Furthermore, P describes all permutations of (k_1, \dots, k_N) and $[P]$ is the parity of the permutation. Similar to the TG case, this state has the energy $E = \sum_{j=1}^N k_j^2$ and momentum $p = \sum_{j=1}^N k_j$. The periodic boundary conditions then lead to the relations

$$k_k L - 2\pi I_k - \sum_{k_l} \theta(k_k - k_l) = 0 \quad (2.27)$$

with $\theta(k) = -2 \tan^{-1}(\frac{k}{c})$ and $I_k = n_k - \frac{N+1}{2}$. This equation can be solved iteratively for all k_j . We follow the work by Yang and Yang [115] to illustrate how to solve Eq. (2.27) numerically. I_k give us a degree of freedom and every particular choice results in a different set of k 's. Minimising

$$B(k_1, \dots, k_N) = \frac{1}{2}L \sum_{i=1}^N k_i^2 - 2\pi \sum_{i=1}^N I_i k_i - \frac{1}{2} \sum_{i,j=1}^N \int_0^{k_i - k_j} \theta(k_i - k_j) d(k_i - k_j) \quad (2.28)$$

solves Eq. (2.27) for a given set of I_k . This is trivial to show by calculating $\frac{\partial}{\partial k_k} B$ which equals the left hand side of Eq. (2.27). For the ground state the I_k are chosen to be centred around 0. Excited states, however, are not as trivial. There, we have to distinguish between two types of elementary excitations [39]. Type

1 excitations take a particle from K , which is the largest value for the k in the ground-state configuration, to a value $q > K$. Type 2 excitations take a particle from $|q| < K$ to $\text{sign}(q) [K + 2\pi/L]$.

The Lieb-Liniger approach is very useful in testing approximate approaches. For instance, one can compare the excitation spectrum with results from the Bogoliubov theory [116]. It was shown in Refs. [38,39] that the low lying Bogoliubov excitations are in good agreement with the Lieb-Liniger theory for weak interactions. Analogous, in Sec. 4.2 we will compare MCTDH calculations with the exact Lieb-Liniger results and show the generality of the rescaling approach presented in Sec. 4.

2.5 Solitons

Solitons are classical phenomena first observed and studied by John Scott Russel (1808-1882). In 1834, when walking along the Scottish Union canal, he observed a single wave travelling for a few kilometres. He named this effect *wave of translation* [117]. Later it was renamed to solitary wave or soliton. Since then, solitons have been identified in other media than water: Clouds can form solitons [47], and even light has been shown to produce solitary waves [48].

Solitons are characterised by their stability, their spatial localisation, and their particle-like scattering properties. They can scatter from each other and remain unchanged afterwards, apart from a phase shift.

The underlying mechanism for the formation of solitons is a subtle interplay between dispersion and nonlinear effects. While dispersion broadens the width of any wave packet, the nonlinearity stabilises it. This can easily be seen when looking at light propagating through glass. In this case, the refractive index varies for different frequencies. This is known as the optical Kerr effect. When a light wave packet of appropriate shape travels through the medium, the nonlinear Kerr effect can result in the self-focusing of the light.

Applications arose due to the invention of fibre optics where solitons can be used for high speed transport of information and data [48]. Furthermore, recent investigations have found solitons in biological structures like DNA and proteins [118].

CHAPTER 2. THEORETICAL BACKGROUND

Therefore, in many respects, solitons are not only unique and exciting but also a highly important physical phenomenon. A theoretical description is desirable and many attempts have been made to describe solitons analytically. One ansatz leads to a nonlinear equation of the form

$$i\dot{u}(x) = \left[-\frac{1}{2}\Delta + U|u(x)| \right] u(x). \quad (2.29)$$

This equation can be solved analytically. Comparing Eq. (2.15) with Eq. (2.29) we find that they are similar for $V(x, t) = 0$ in Eq. (2.15). This suggests that solitons should be observable in Bose condensed gases as well. Two analytical solutions exist, depending on the sign of the interaction parameter g . For repulsive bosons, i.e. $g > 0$, the solutions are called dark solitons. In a uniform gas their general analytical expression is given by

$$\psi(x, t) = A \left(i\frac{v}{c} + \sqrt{1 - \frac{v^2}{c^2}} \tanh \left[B(x - x_0) \sqrt{1 - \frac{v^2}{c^2}} \right] \right) e^{i\theta(x, t)}$$

where A and B are system-dependent constants, x_0 is the initial position at $t = 0$, v is the velocity of the travelling soliton, c is the speed of sound and $\theta(x, t)$ is the time-dependent phase. For $V = 0$ the soliton is characterised by a dip in density at $x_{dip} = x_0$ and a π -phase jump at x_{dip} , and therefore it is called a dark soliton. For time-dynamical simulations and experiments with $v \neq 0$ grey soliton solutions exist. In this case, the dip is not as pronounced, i.e. the density at the soliton centre is non-zero. Therefore, one of the ways to create such a dark soliton is to stir a condensate confined in a ring geometry [119]. Their stability and relation to higher-dimensional objects, the so-called vortices, is discussed in Ref. [120].

The work presented in this thesis solely focuses on bright solitons, which means that the interparticle interaction is attractive, i.e. $g < 0$. Hence, the solution of Eq. (2.15) for a vanishing potential $V(x, t) = 0$ is given by

$$\psi(x) = A \operatorname{sech} \left(A\sqrt{-g}(x - x_0 - vt) \right) e^{i\theta(x, t)}, \quad (2.30)$$

with an amplitude A , velocity v , and x_0 being the position at $t = 0$. The solution

is normalised according to

$$\mathcal{N} = \int dx |\psi(x, t)|^2 = \frac{2A}{\sqrt{-g}}. \quad (2.31)$$

The phase is given by $\theta(x, t) = vx - \omega t$ and $\omega = v^2/2 + \mu$ is the frequency. The chemical potential of a stationary soliton is given by $\mu = gA/2$. Furthermore, the width of the soliton is defined as $l_s = 1/(A\sqrt{-g})$ [49].

For all the numerical simulations in chapter 3 we set $g = -1$. This leads us to the relation $\tilde{E} = -g_{1D}\tilde{n}$. Moreover, we assume the amplitude to be $A = 1$, and therefore $N = 2\tilde{n}\tilde{z}$. Hence, solving the equation $\tilde{E} = -g_{1D}N/2\tilde{z} = \hbar^2/(m\tilde{z}^2)$ for \tilde{z} fully determines the energy scale as $\tilde{E} = mN^2g_{1D}^2/(4\hbar^2) = N^2\omega_{\perp}^2 a_s^2 m$ and the unit length $\tilde{z} = -\hbar/(N\omega_{\perp} a_s m)$. Therefore, the unit length is determined by the width of the soliton which is simply given by $l_s = 1$.

Typical experimental values for a BEC of ${}^7\text{Li}$ [50, 51] are $\omega_{\perp} \approx 2\pi \times 710\text{Hz}$, $a_s \approx -0.2\text{nm}$ and $N \approx 6 \times 10^3$. This yields a length scale of $\tilde{z} \cong 1.7\mu\text{m}$, which is consistent with experimental observations [50]. The time unit is $\tilde{t} \approx 0.3\text{ms}$ which relates to a velocity scale of $\tilde{z}/\tilde{t} \approx 5.7\mu\text{m/ms}$, a value that is experimentally accessible as well. Because of the quasi-one-dimensionality there are restrictions on the particle number and the interaction: The transverse energy unit $\hbar\omega_{\perp}$ must be much larger than the interaction energy [46] and the longitudinal width of the soliton should be small enough so that the transverse potential energy does not expand and destroy the condensate [50, 121–124].

2.6 MCTDH/MCTDHB - Theory behind Qiwib

Two approaches have already been discussed in Sec. 2.1.4 for going beyond the mean-field Gross-Pitaevskii approach. In this section we introduce the multiconfigurational time-dependent Hartree (MCTDH) approach and its bosonic version (MCTDHB), two theoretical methods based on a finite basis-set expansion. It shows great promise for describing multi-particle systems to high accuracy.

2.6.1 Finite basis-set expansion

Consider N quantum particles in three dimensions interacting with each other via $W(\vec{r}_i, \vec{r}_j)$, following the notation in Ref. [92]. The particles are subject to an external potential $V_{\text{ext}}(x, t)$, which may depend on time:

$$H_{mb} = \sum_i^N h_i(\vec{r}_i, t) + \sum_{i<j} W(\vec{r}_i, \vec{r}_j). \quad (2.32)$$

Here $h_i = -\frac{\hbar^2}{2m}\Delta_{\vec{r}_i} + V_{\text{ext}}(\vec{r}_i, t)$ is the one-body Hamiltonian for the i th particle and \vec{r}_i its spatial position. For simplicity we assume that all particles have the same mass m . Although we will specifically deal with identical bosons later on, at this point considerations are not restricted to a specific quantum statistics and the Hamiltonian (2.32) could describe single or multi-component Bose or Fermi gases or mixtures thereof. All these possibilities are of interest and related to actual or possible experimental scenarios.

The true N -particle wave function can be expanded in the form

$$\Psi(\vec{r}_1, \dots, \vec{r}_N, t) = \sum_J A_J(t) \Phi_J(\vec{r}_1, \dots, \vec{r}_N), \quad (2.33)$$

in a basis consisting of products of single-particle wave functions

$$\Phi_J(\vec{r}_1, \dots, \vec{r}_N) = \prod_{k=1}^N \phi_{j_k}(\vec{r}_k), \quad (2.34)$$

where we have introduced the multi-index $J = (j_1, \dots, j_N)$ for the set of N single-particle indices. The single-particle wave functions (or *mode* functions) are mutually orthonormal, i.e. $\int \phi_j^*(\vec{r}) \phi_k(\vec{r}) d\vec{r} = \delta_{jk}$.

In practice we choose a finite set of M single-particle functions to define the finite basis-set expansion. The size of the finite basis of multi-particle Hilbert space is nominally M^N , although for identical particles this number is significantly smaller by accounting for bosonic or fermionic exchange symmetry. For bosons, which we investigate in this thesis, the size of the Hilbert space reduces to a binomial coefficient $\binom{N+M-1}{N} = \frac{(N+M-1)!}{N!(M-1)!}$. Note that for $M = 1$ the problem

reduces to the GP approach.

Therefore, the full problem in Eq. (2.32) is approximated by truncating the Hilbert space to span a finite basis and represent the Hamiltonian as a finite matrix with elements

$$H_{IJ} = \langle \Phi_I | H_{mb} | \Phi_J \rangle. \quad (2.35)$$

We denote the solution of the corresponding matrix Schrödinger equation for the coefficient vector with \bar{A}_J and the eigenvalues of the truncated matrix \bar{E}_ν . These approximate the exact coefficient vector A_J and eigenvalues E_ν , which form part of the spectrum of H_{mb} . Since the basis-set truncation can be understood as a variational procedure with a restricted variational space, the approximate ground-state energy $\bar{E}_G \geq E_G$ is an upper bound for the true one. By increasing the number of modes M , and thereby computational space, the approximation improves and the approximate energy converges to the correct one. However, for an interacting system this convergence is painfully slow, as seen in chapter 4.

2.6.2 Variationally optimised basis - MCTDH

Variationally optimising the set of single-particle functions defined in Eqs. (2.33) and (2.34) is the aim of the MCTDH method [88–90]. Starting from the same many-body problem Eq. (2.32), we use the same basis-set expansion as in Eqs. (2.33) and (2.34), where we now allow the single-particle wave functions $\phi_j(x, t)$ to be time-dependent in addition to the time-dependence of the coefficients $A_J(t)$

$$\begin{aligned} \Psi(\vec{r}_1, \vec{r}_2, \dots, \vec{r}_N, t) &= \sum_J A_J(t) \Psi_J(\vec{r}_1, \vec{r}_2, \dots, \vec{r}_N, t) \\ &= \sum_{j_1}^{M_1} \sum_{j_2}^{M_2} \dots \sum_{j_N}^{M_N} A_{j_1, j_2, \dots, j_N}(t) \phi_{j_1}^{(1)}(\vec{r}_1, t) \phi_{j_2}^{(2)}(\vec{r}_2, t), \dots, \phi_{j_N}^{(N)}(\vec{r}_N, t). \end{aligned} \quad (2.36)$$

This allows us to perform a consistent derivation of the best possible state by optimising A_J and $\phi_j^{(k)}$ simultaneously as we will show later on. Now, each degree of freedom is described by a separate set of M_i single-particle wave functions. For $M_i \rightarrow \infty$ this expansion is exact. These single-particle functions are still

orthogonal and normalised via

$$\int d\vec{r} \phi_{j_i}^{(k)\dagger}(\vec{r}_i) \phi_{j_j}^{(k)}(\vec{r}_i) = \delta_{ij}$$

for all k, i, j . A variational principle leads to the MCTDH coupled equations of motion for the coefficients and single-particle wave functions, which can be solved with the MCTDH program package [88, 90, 91].

For a fixed basis of single-particle functions MCTDH reduces to the exact diagonalisation method. Therefore, the key advantage is that MCTDH always stays in a variationally optimised basis. This generally ensures higher accuracy or keeps the Hilbert space as small as possible for a given accuracy. MCTDH is therefore effective at describing different trapping potentials, yet requires a numerically unattainable number of single-particle functions to describe strongly interacting systems. In chapter 4 we will investigate the convergence properties of MCTDH with respect to M in more detail.

2.6.3 MCTDHB/QiwiB

This thesis exclusively investigates bosonic systems in one dimension. For this, a bosonic version of the MCTDH, the so-called MCTDHB, where “B” stands for bosons, can be derived. This theory takes advantage of the bosonic symmetry, and therefore many Hartree products in Eq. (2.36) are the same. This reduces the truncated Hilbert space significantly compared to MCTDH, which always includes all permutations of a Hartree product, even for purely bosonic simulations. Also, numerical inaccuracies in the simulations lead to errors that can destroy the bosonic symmetry in MCTDH which leads to the system converging into a fermionic state. This problem, however, is not present within MCTDHB. Therefore, we developed QiwiB (see chapter 5), a program that solves the MCTDHB equations. For the derivation of the MCTDHB equations of motion we follow Ref. [92].

First we simplify the derivation by considering N interacting bosons in one dimension subject to an external potential $V_{\text{ext}}(x, t)$, which may again depend on

time. The Hamiltonian for this system is given by

$$H_{mb} = \sum_{i=1}^N h_i(x_i) + \sum_{i<j} g\delta(x_i - x_j), \quad (2.37)$$

where $h_i = -\frac{\hbar^2}{2m} \frac{\partial^2}{\partial x_i^2} + V_{\text{ext}}(x_i, t)$ is the one-body Hamiltonian for particles of the same mass m interacting by contact interactions of strength g . This model is able to describe, for instance, quantum gases of ultracold atoms in an elongated and tightly confining trapping potential [109] and is therefore suitable for the problems presented in this thesis.

Since we are dealing with indistinguishable particles only one set of single-particle functions is necessary to describe all particles. Therefore, Eq. (2.36) for the purely one-dimensional bosonic case reduces to

$$\begin{aligned} \Psi(x_1, x_2, \dots, x_N, t) &= \sum_J A_J(t) \Psi_J(x_1, x_2, \dots, x_N, t) \\ &= \sum_{j_1}^M \sum_{j_2}^M \dots \sum_{j_N}^M A_{j_1, j_2, \dots, j_N}(t) \phi_{j_1}(x_1, t) \phi_{j_2}(x_2, t), \dots, \phi_{j_N}(x_N, t) \end{aligned} \quad (2.38)$$

but with the same set $\{\phi_j\}$ for all degrees of freedom compared to Eq. (2.36). It is convenient to turn to second quantisation and define our problem in terms of operators and Fock states. For this we introduce the bosonic field operator $\hat{\Psi}(x)$ that annihilates a particle at position x and the related annihilation operators b_k for the single-particle functions ϕ_k , defined as

$$\begin{aligned} b_k(t) &= \int \phi_k^\dagger(x, t) \hat{\Psi}(x) dx, \\ [b_k, b_l] &= [b_k^\dagger, b_l^\dagger] = 0, \\ [b_k^\dagger, b_l] &= \delta_{kl}. \end{aligned}$$

In terms of the new operators b and b^\dagger Eq. (2.37) transforms into

$$\hat{H} = \sum_{k,q} b_k^\dagger b_q h_{kq} + \frac{1}{2} \sum_{k,s,q,l} b_k^\dagger b_s^\dagger b_q b_l W_{ksql}, \quad (2.39)$$

with

$$h_{kq} = \int dx \phi_k^*(x, t) h_q(x, t) \phi_q(x, t),$$

$$W_{ksql} = g \int dx \phi_k^*(x, t) \phi_s^*(x, t) \phi_q(x, t) \phi_l(x, t).$$

Moreover, Eq. (2.38) can then be written in terms of bra and ket vectors as

$$|\Psi(t)\rangle = \sum_{\vec{n}} C_{\vec{n}}(t) |\vec{n}, t\rangle$$

$$= \sum_{n_1} \cdots \sum_{n_M} C_{n_1, n_2, \dots, n_M} \prod_{k=1}^M \frac{1}{\sqrt{n_k!}} [b_k^\dagger(t)]^{n_k} |\text{vac}\rangle, \quad (2.40)$$

where we introduced the new prefactors $C_{\vec{n}}$. The occupation of the single-particle functions is given by $\vec{n} = (n_1, n_2, \dots, n_M)$. Naturally, this means that $\sum_{i=1}^M n_i = N$, where N is the number of bosons in the system.

Within the Lagrangian formalism we can define the action as

$$S[\{C_{\vec{n}}(t)\}, \{\phi_k(x, t)\}] = \int dt \left\{ \langle \Psi | \hat{H} - i \frac{\partial}{\partial t} | \Psi \rangle - \sum_{k,j=1}^M \mu_{k,j}(t) [\langle \phi_k | \phi_j \rangle - \delta_{k,j}] \right\},$$

where the $\mu_{k,j}$ ensure orthogonality and normalisation. Hence the variation with respect to $\{C_{\vec{n}}\}$ and $\{\phi_k\}$ leads to two coupled equations of motion. The details of the derivation can be found in [92]. Before we can write down the final equations of motion, we introduce the reduced one-body density matrix

$$\rho(x_1, x_2, t) = \langle \hat{\Psi}^\dagger(x_2) \hat{\Psi}(x_1) \rangle = \sum_{k,q=1}^M \rho_{kq} \phi_k^*(x_2) \phi_q(x_1) \quad (2.41)$$

and the reduced two-body matrix

$$\rho(x_1, x_2, x'_1, x'_2, t) = \langle \hat{\Psi}^\dagger(x_2) \hat{\Psi}^\dagger(x'_2) \hat{\Psi}(x_1) \hat{\Psi}(x'_1) \rangle \quad (2.42)$$

$$= \sum_{k,s,q,l=1}^M \rho_{ksql} \phi_k^*(x_2) \phi_s^*(x'_2) \phi_q(x_1) \phi_l(x'_1). \quad (2.43)$$

The ρ_{kq} and ρ_{ksql} together with h_{kq} and W_{ksql} form the so-called mean-fields in the numerical integration and are updated every so-called mean-field time step (see appendix B.3.4 for details and the numerical implementation). Finally, the equations of motion are given by

$$\begin{aligned} \mathbf{H}_{\vec{C}}(t)\vec{C}(t) &= i\frac{\partial}{\partial t}\vec{C}(t) \\ i\frac{\partial}{\partial t}|\phi_j\rangle &= \hat{\mathbf{P}} \left[\hat{h}|\phi_j\rangle + g \sum_{k,s,q,l=1}^M \{\boldsymbol{\rho}^{-1}\}_{jk}\rho_{ksql}\phi_s^*(x)\phi_l(x)|\phi_q\rangle \right] \end{aligned} \quad (2.44)$$

with the projector

$$\hat{\mathbf{P}} = 1 - \sum_{m=1}^M |\phi_m\rangle\langle\phi_m|,$$

the inverse of the density matrix $\boldsymbol{\rho} = \{\rho_{kq}\}$, $\mathbf{H}_{\vec{C}} = \{H_{\vec{n}\vec{m}} = \langle\vec{n}|\hat{H}|\vec{m}\rangle\}$ and $\vec{C} = \{C_{\vec{n}}\}$. Eq. (2.44) can now be solved numerically. Details for this and the implementation into QiwiB can be found in appendix B.3.

The projector in Eq. (2.44) also implies that the single-particle wave-functions are orthogonal to their variation in time:

$$\langle\phi_i|\frac{\partial}{\partial t}|\phi_j\rangle = 0$$

for all i, j . We also want to note that this is only a special case of constraints that can be defined and included into the equations of motion [125, 126]. Those constraints do not change the physics of the problem. However, they might benefit certain systems by decreasing convergence times or simulation times. Generally these constraints \hat{g} are defined as $\langle\phi_i|\frac{\partial}{\partial t}|\phi_j\rangle = \langle\phi_i|\hat{g}|\phi_j\rangle$. However, for the QiwiB and the MCTDH calculations described in chapter 5 we choose $\hat{g} = 0$ as otherwise the equations of motion are slightly more complicated.

Fragmentation of BECs

In MCTDH(B) there is a freedom of choice for the optimal basis since a unitary transformation $\overline{\phi}_j = \sum_{i=1}^M U_{ij}\phi_i$ can turn a given basis $\{\phi_i\}$ into a equivalent basis $\{\overline{\phi}_j\}$. One particularly interesting basis is the natural orbital basis $\{\phi_i^{NO}\}$. The

basis diagonalises the density matrix ρ_{kq} so that the reduced density matrix is given by

$$\rho(x_1, x_2, t) = \langle \hat{\Psi}^\dagger(x_2) \hat{\Psi}(x_1) \rangle = \sum_{k=1}^M \rho_k [\phi_k^{NO}(x_2)]^* \phi_k^{NO}(x_1). \quad (2.45)$$

For all k , where ρ_k is macroscopic, i.e. $\rho_k \sim O(N)$, the natural orbitals ϕ_k^{NO} represent a macroscopic population of Gross-Pitaevskii-like mean-field wave functions. As shown in Sec. 2.2.2, a large value of ρ_k is related to long-range order in the one-body density matrix and therefore Bose-Einstein condensation. One single non-zero value of ρ_k leads to the same results as predicted by the GP theory (see Sec. 2.1.3). However, for two or more large values of ρ_k MCTDHB describes fragmented states, which goes beyond what is achievable with GP theory. This is demonstrated in chapter 5 where we will numerically create stable fragmented states, so-called NOON states, during dynamical scattering processes.

So far MCTDHB has been used to study several physical problems, such as the fermionisation of a few-particle system [127] or the dynamics of bosons in a double well [128]. More recently, the scattering of a soliton on a positive barrier and the existence of NOON states have been subject of investigation [28–30, 76].

MCTDH and MCTDHB overview

We summarise the advantages and disadvantages of MCTDH:

- variationally optimised basis - usually gives higher accuracy for the same size of the Hilbert space compared to exact diagonalisation
- suitable for bosonic and fermionic systems and different kinds of particles
- suitable for weak interactions as well as strong interactions
- few approximations are needed and only the restriction to a finite number of single-particle functions is relevant
- Heidelberg MCTDH program package is written in Fortran and source code is available upon request [91]

2.6. MCTDH/MCTDHB - THEORY BEHIND QIWIB

- calculation of excited states achievable
- calculation of stationary states is possible as well as time-dependent simulations
- well documented and no programming skills required
- highly parallelised
- not suitable for large number (>10) of particles

- inclusion of temperature non-trivial
- We do not mention the many other details of MCTDH that are not of much relevance for the work presented in this thesis but refer to [90].

On top of that, the MCTDHB method has additional advantages:

- takes advantage of bosonic symmetry - reduced Hilbert space
- program package Qiwib developed for this thesis solves MCTDHB equations (for more information see App. D)
 - capable of performing calculations with up to thousands of particles
 - automatically keeps bosonic symmetry
 - user-friendly interface
 - documentation available
 - open source

*The most exciting phrase
to hear in science, the
one that heralds new dis-
coveries, is not "Eureka!"
("I found it!") but rather
"hmm....that's funny..."*

Isaac Asimov

3

Bright soliton scattering with Gross-Pitaevskii

This chapter focuses on the scattering of a moving soliton from an attractive rectangular well. While exact solutions of the one-dimensional Schrödinger equation for the scattering of single particles from a well are well known, the nonlinearity in the Gross-Pitaevskii equation gives rise to new and exciting phenomena. Previously, it was found that under certain conditions the soliton fully reflects from the well [66]. The quantum nature of the discrete bound states is found to be responsible for this non-classical behaviour, which the authors introduced as enhanced quantum reflection. In this thesis, we show that in addition other effects can be observed as well. In particular, the soliton can be permanently trapped for a range of potential depths. This is a new and exciting result that does not occur for single-particle scattering. The studies in this chapter, for the first time, explain the non-trivial physics during the scattering process and its resulting interesting effects, such as quantum reflection, resonant tunnelling and trapping.

After an introduction to the problem in Sec. 3.1, numerical results are presented and discussed (see Sec. 3.2). Furthermore, to get a deeper understanding of the underlying mechanism, we solved a variational two-mode model and present analytical work on the trapping process in sections 3.3 and 3.4 respectively. Finally, a method to probe energy levels in a potential of unknown shape is proposed. The results presented in this chapter have already been published by the author [94].

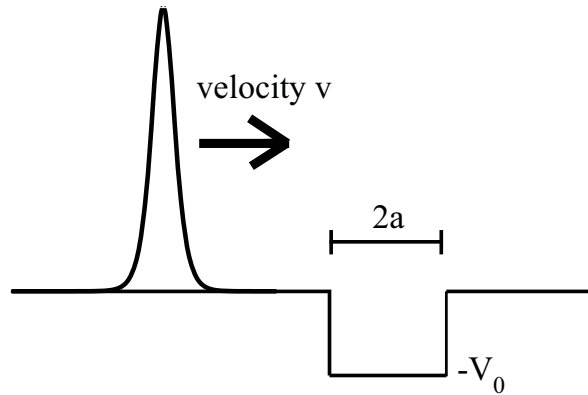


Figure 3.1: A bright soliton is being scattered by a rectangular well with width $2a$ and depth V_0 .

3.1 Introduction to the problem

In this chapter we use dimensionless units as described in Sec. 2.3 and solve the one-dimensional Gross-Pitaevskii equation given in Ref. 2.15. In chapter 2.5 we already discussed the general theoretical description of a bright soliton travelling with velocity v . Here we investigate its scattering behaviour when adding an attractive well. For simplicity we assume the well to be a rectangular potential well defined as

$$V_{ext}(x) = \begin{cases} 0 & \text{for } |x| > a \\ -V_0 & \text{for } |x| \leq a. \end{cases} \quad (3.1)$$

Initially a soliton solution of the form given by Eq. 2.30 propagates towards the well which is shown in Fig. 3.1.

The width of the potential well has to be chosen small enough so that a particle-like propagation of the soliton due to an adiabatically changing potential can be avoided. For such a potential the soliton is expected to behave classically and always pass the well. Here $l_s = 2a = 1$ satisfies this condition and is chosen unless

3.2. PHENOMENOLOGY OF SOLITON SCATTERING BY A QUANTUM WELL

specified otherwise.

Previously Lee and Brand [66] investigated in detail the enhanced reflection of solitons for the special case of a Rosen-Morse potential $V_{ext}(x) = -V_0 \text{sech}^2(\alpha x)$ at low velocities. They discovered that the soliton is reflected from the well for velocities below a critical velocity v_c , while for $v > v_c$ the soliton fully transmits over the well. This was observed by investigating the phase of the soliton when scattered of the well and it was suggested that resonant processes are responsible for these effects.

Here, we solved Eq. (2.15) numerically via the Crank-Nicholson method using a standard finite difference discretisation of the spatial derivatives (see Appendix B.1). The results were verified with an adaptive 5th order Runge-Kutta-Fehlberg method. The algorithms were implemented in standard C/C++ and Octave [129]. The simulations were performed in a box with hard wall boundaries. The box length was set to $l_{box} = 80$ unless stated otherwise. Furthermore, we used $N_g = 2001$ grid points and a fixed time step of $\Delta t = 0.01$. The convergence of our calculations with respect to these quantities was monitored carefully. Reflection from the boundaries was avoided by appropriate timing of the simulation. We also used complex absorbing potentials at the boundaries to verify that reflection effects remained below a quantifiable threshold.

3.2 Phenomenology of soliton scattering by a quantum well

In this section we present results from numerical solutions of Eq. (2.15) corresponding to a soliton approaching the well given by Eq. (3.1). Here, the interaction between the particles is chosen to be $g = -1$ while the wave function is normalised according to $\int |\psi|^2 dx = 2$. Therefore, the soliton's amplitude is given by $A = 1$. In Sec. 2.5 this was shown to be a convenient choice. In the initial set-up the soliton (2.30) is being placed at position $x_0 = -12$ left of the quantum well and moving with the velocity $v > 0$ towards it (see Fig. 3.1).

As physical observables we introduce the reflected (R), trapped/localised (L), and transmitted (T) fraction of the soliton, which are calculated at a time signi-

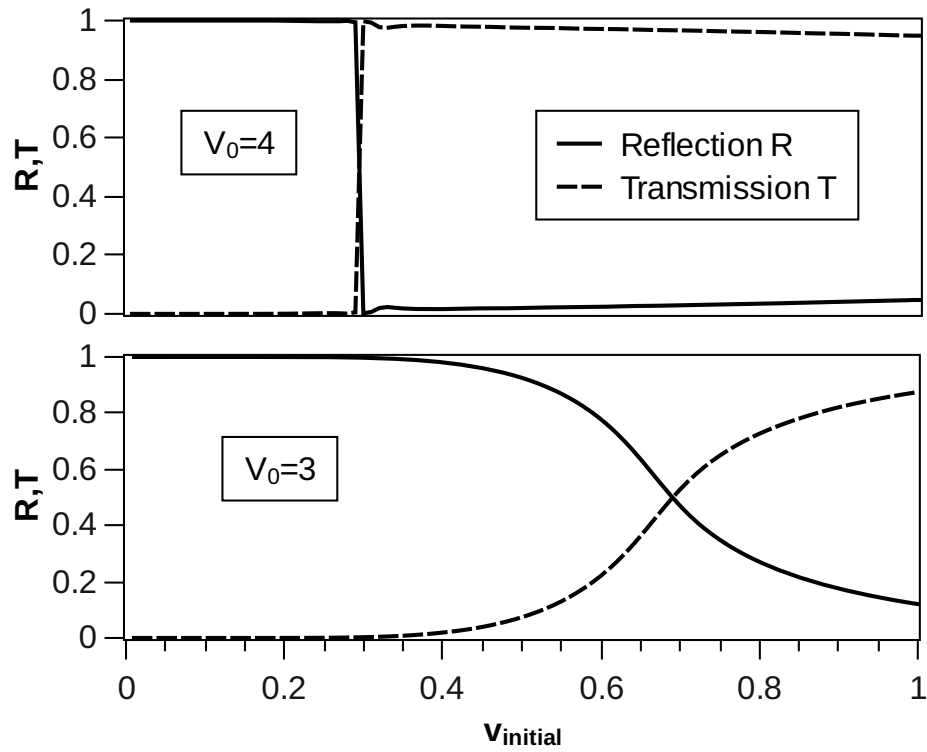


Figure 3.2: The reflected (R) and transmitted (T) fraction after the collision with the well for varying initial velocities and two different potential depths. For $V_0 = 4$ the top panel shows that for small values of v_{initial} the soliton is being fully reflected while above a critical velocity $v_{\text{initial}} > v_c$ the soliton travels over the well undisturbed. A slightly smaller depth of $V_0 = 3$ shows a smooth transition from the fully reflecting to the fully transmitting regime.

3.2. PHENOMENOLOGY OF SOLITON SCATTERING BY A QUANTUM WELL

ificantly after the initial impact of the soliton from the well:

$$\begin{aligned}
 R &= \frac{1}{\mathcal{N}_s} \int_{-\infty}^{-8a} dx |\psi(x, t)|^2 \\
 L &= \frac{1}{\mathcal{N}_s} \int_{-8a}^{8a} dx |\psi(x, t)|^2 \\
 T &= \frac{1}{\mathcal{N}_s} \int_{8a}^{\infty} dx |\psi(x, t)|^2,
 \end{aligned} \tag{3.2}$$

with $R + L + T = 1$ and $a = \frac{1}{2}$. Fig. 3.2 shows R and T for varying initial velocities and two different potential depths. For $V_0 = 4$ the top panel shows that for small values of the initial velocity v_{initial} the soliton is fully reflected, while above a critical velocity $v_{\text{initial}} > v_c$ the soliton travels over the well undisturbed. A slightly smaller depth $V_0 = 3$ shows a more smooth transition from the fully reflecting to the fully transmitting regime. From this we draw the conclusion that it will be interesting to study the dependence of the scattering properties on the potential depth.

Figure 3.3 shows R , T and L as a function of the depth of the well for a fixed initial velocity $v_{\text{initial}} = 0.3$. We chose to study the case of small velocity where $v_{\text{initial}}^2/2 \ll |\mu| = 0.5$. For the parameters of Ref. [51] (see also Sec. 3.1), this velocity amounts to $v \approx 1.7\text{mm/s}$.

The upper panel of Fig. 3.3 shows several regimes with similar results. On a background of almost complete reflection we find potential depths that allow the soliton to be fully transmitted or trapped. We thus call these regimes transmission-reflection-trapping (*TRL*) windows. In the following, we focus our discussion mostly on the second window around $V_0 = 5$, as shown in the lower panel for a smaller range of V_0 .

For certain values of V_0 the soliton reflects completely from the well. But by increasing the depth of the quantum well R suddenly drops to zero while the transmitted fraction jumps to an absolute maximum. Further increase gives a sudden drop of T to almost zero and most of the soliton is trapped inside the quantum well. Then the trapping component L starts to decrease while the reflected part increases. At least some of the reflected and transmitted amplitude in this part of Fig. 3.3 can be attributed to what we define as radiation, i.e. small amplitude

CHAPTER 3. BRIGHT SOLITON SCATTERING WITH GROSS-PITAEVSKII

waves. This becomes apparent in Fig. 3.4, where snapshots of the density of the time-dependent wave function are shown. We will discuss the role that radiation plays in enabling trapping by carrying away kinetic energy in Sec. 3.4. For slightly larger V_0 we observe the co-existence of a reflected soliton with a trapped component together with radiation in the transmission channel becoming very small again.

Figure 3.4 reveals another remarkable feature: The condensate density has a single node localised close to the centre of the well. Our simulations show that the number of nodes located in the well is a characteristic of each TRL window. Indeed we find that TRL windows appear around a critical well depth, at which a new linear bound state with the appropriate number of nodes is formed. In the first TRL window, the density reveals no node, the second one shows one, the third one shows two nodes and so on. The density of the soliton while located above the well is similar to the density functions for bound states of the Schrödinger equation in a quantum well. A more detailed analysis of the relation of the TRL window to linear resonances and nonlinear bound states of the well is given further on in this section.

The time-dynamics of the soliton are summarised in the density plot in Fig. 3.5. The pictures show the four different scenarios of full reflection, full transmission, full trapping and partial trapping. On the lower left picture the density sloshes around the centre but a closer look reveals that the radiation reduces the amplitude of this oscillation and therefore stabilises the trapped soliton. Furthermore, the position of the dip in density remains almost stationary, varying by not more than 5% of the potential width. The reason for this is that for our choice of parameters the energy differences between the bound states in the well are large compared to any energy scale of the incoming soliton. Hence only one of these states can be populated, in the case of Fig. 3.5 it is the first excited state.

We now discuss the relation of the trapping phenomenon to (stationary) non-linear bound states of the well. Figure 3.6 compares two different observables. The first is the trapped component L from the time-dependent simulations. The other observable is the relative number of particles $N_{L,rel}(V_0)$ in an eigenstate of the time-independent Gross-Pitaevskii equation for a fixed chemical potential μ . This is set to the same value as the chemical potential of the initial soliton

3.2. PHENOMENOLOGY OF SOLITON SCATTERING BY A QUANTUM WELL

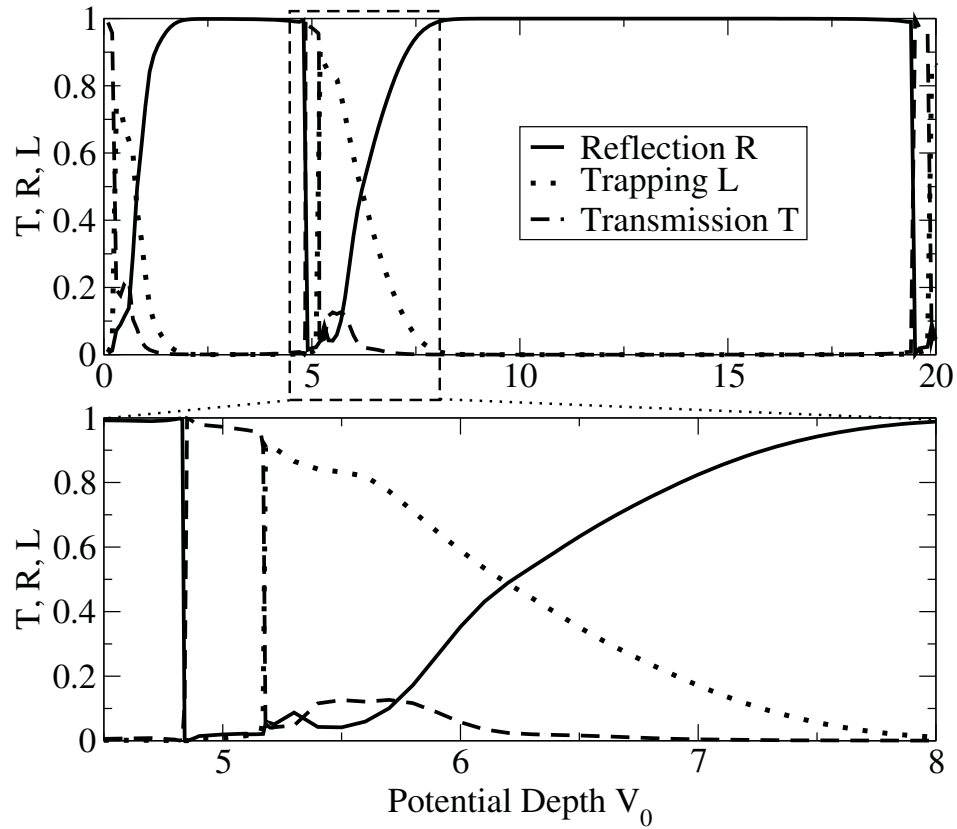


Figure 3.3: Reflection R , Transmission T and Trapping L (L for localised) as a function of V_0 and a fixed velocity $v = 0.3$ by solving Eq. 2.15. The lower picture shows the section around the second TRL window. The well width $2a = 1$ is kept constant and we use $A = 1$ and $g = -1$. The same parameters are used throughout the paper unless explicitly stated otherwise.

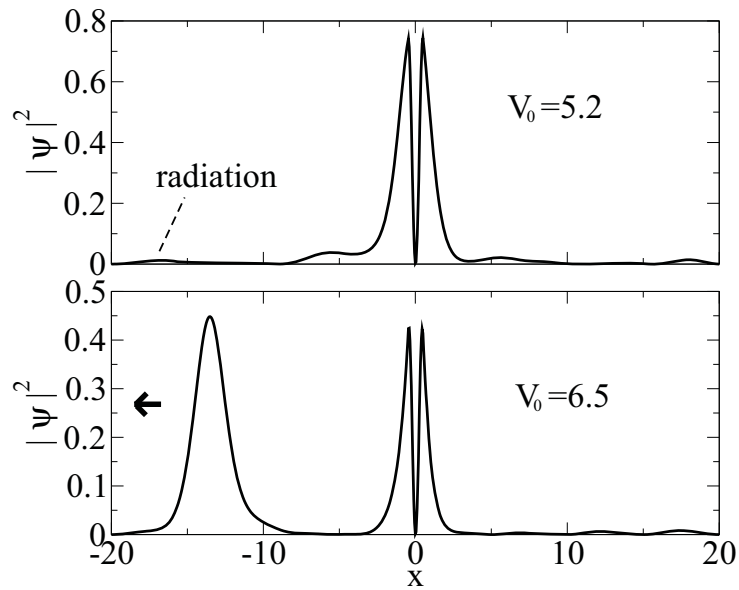


Figure 3.4: The upper picture shows a snapshot of the condensate density at $t = 77$ for $V_0 = 5.2$ where trapping is maximised in the second *TRL* window. One can see the trapped mode in the first excited bound state (see text) and the radiation which stabilises the trapped soliton. The lower picture shows partial trapping with a reflected soliton at $t = 65$ and $V_0 = 6.5$.

3.2. PHENOMENOLOGY OF SOLITON SCATTERING BY A QUANTUM WELL

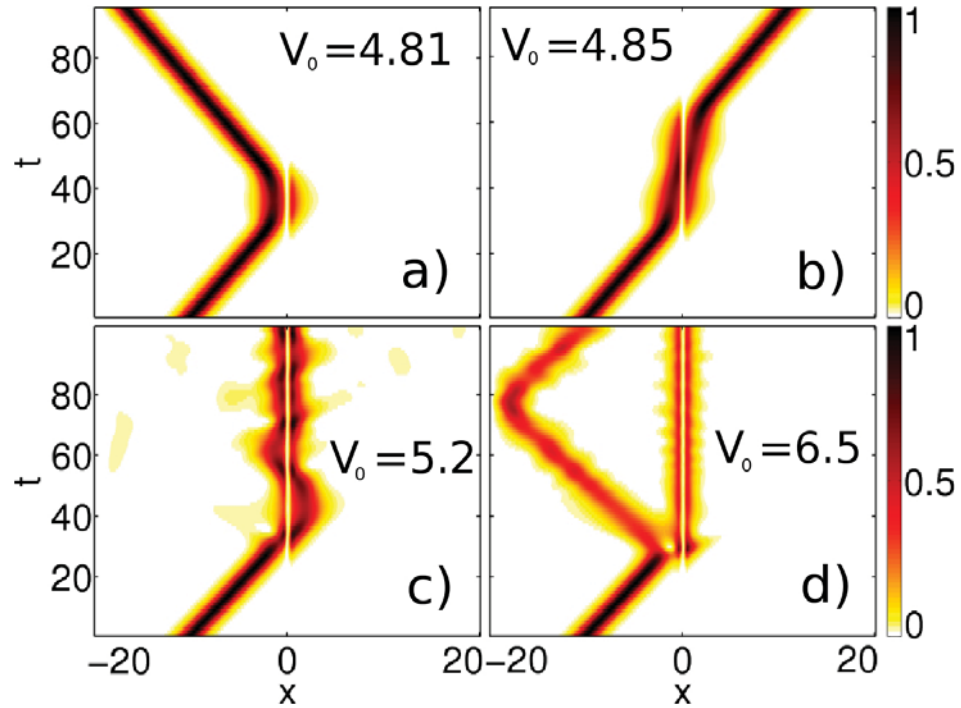


Figure 3.5: Time and spatial dependence of the condensate density $|\psi(x, t)|^2$ (normalised to a maximum amplitude of 1) for four different V_0 as in Fig. 3.3 but with $l_{box} = 40$. The case of full reflection is shown in panel a) while the one for full transmission is given in b). Furthermore, c) presents a fully trapped soliton while in d) the case of partial trapping and reflection is shown (the additional reflection towards the end comes from the hard wall boundary conditions).

CHAPTER 3. BRIGHT SOLITON SCATTERING WITH GROSS-PITAEVSKII

($\mu_{\text{initial}} = -0.5$) in the time-dependent simulations. Specifically, $N_{L,rel}(V_0)$ is given by

$$N_{L,rel}(V_0) = \frac{\mathcal{N}_E(V_0, \mu)}{\mathcal{N}_S(\mu)} \quad (3.3)$$

where $\mathcal{N}_E(V_0, \mu)$ is the normalisation constant (2.31) of the single-node stationary solution of Eq. (2.15) with the chemical potential μ while $\mathcal{N}_S(\mu)$ is the normalisation of a free soliton with the same chemical potential. In the numerical procedure V_0 is changed iteratively to keep the chemical potential at the desired value. The results for $N_{L,rel}(V_0)$ can then be compared with the relative number of trapped atoms L , obtained from the time-dependent simulations. Even for different parameters the agreement between both graphs is very good. Therefore, the trapped part of the soliton in the time-dynamical simulations populates an eigenstate in the well. These findings indicate that trapping is a resonant phenomenon with the chemical potential being the parameter of primary relevance.

Another feature in Fig. 3.3 are the resonant transmission bands. They are closely related to the above-barrier transmission resonances in the linear Schrödinger equation, which is found from Eq. 2.15 for $g = 0$. There one can find an exact solution for the transmission [130]

$$T_{\text{lin}}(V_0) = \left[1 + \frac{V_0^2}{v^2(v^2 + 2V_0)} \sin^2(2a\sqrt{v^2 + 2V_0}) \right]^{-1}. \quad (3.4)$$

In Fig. 3.7 we compare the transmission for $g = 0$ with the case of solitons at $g = -1$ at different velocities v . For very high velocities both curves approach each other. This is easily explained by the fact that the kinetic part in Eq. (2.15) becomes much larger than the nonlinear term and therefore dominates the transmission spectrum. Thus decreasing v smoothly increases the effects of the nonlinearity, in particular the formation of resonant transmission windows instead of transmission resonance lines. But their positions remain the same, which means that the nonlinearity just affects the shape of the transmission lines. Therefore, the basic mechanism of above-well shape resonances known from the linear Schrödinger equation remains valid for solitons.

3.2. PHENOMENOLOGY OF SOLITON SCATTERING BY A QUANTUM WELL

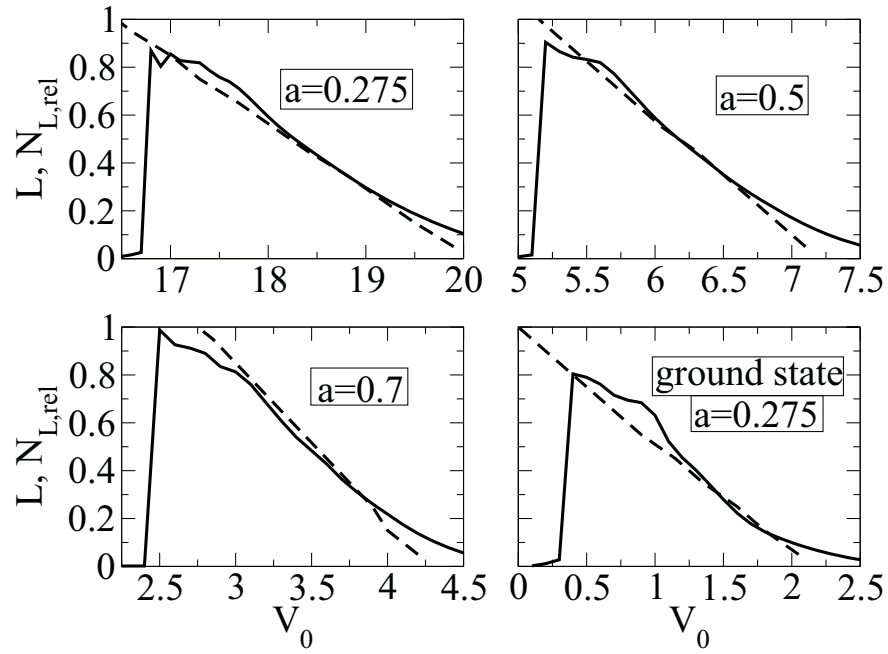


Figure 3.6: $L(V_0)$ (solid line) from the time-independent solutions and $N_{L,rel}(V_0)$ (dashed line) from the time-independent calculations around the second bound state at $V_0 \approx 5$ for a fixed chemical potential $\mu = -\frac{1}{2}$. Both quantities show similar behaviour, even for different potential width. In addition the bottom right picture a similar agreement for calculations near the first bound state at small V_0 .

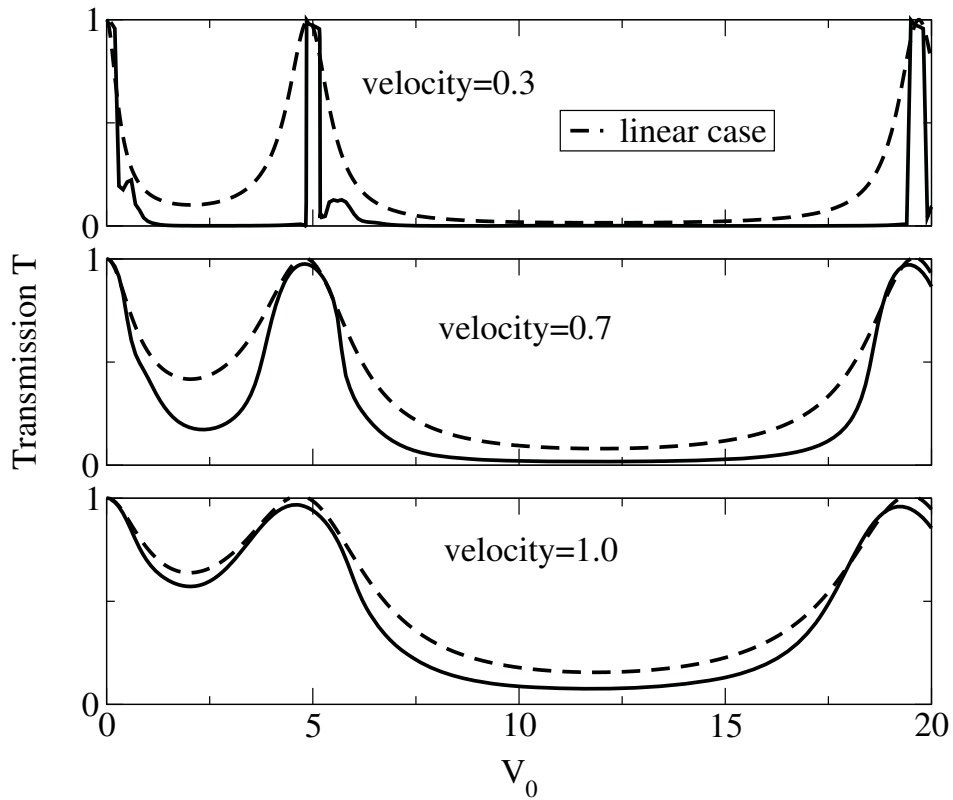


Figure 3.7: Comparison of T for solitons ($g = -1$, solid line) with the analytical solution $T_{\text{lin}}(V_0)$ [Eq. (3.4)] for linear waves ($g = 0$, dashed line). From top to bottom we increased v_{initial} of the incoming soliton. For increasing velocities the kinetic term in the Gross-Pitaevskii equation becomes dominant, and therefore both curves approach each other.

3.3 Variational analysis

3.3.1 Two-mode model

Goodman et al. [63] studied soliton-defect interactions by simple two-mode models featuring a mobile soliton and a localised (trapped) mode. Here we extend this approach by including a so-called breathing mode for the trapped soliton which allows for an oscillation of the soliton width over time.

We approximate the well by an attractive delta potential, defined as

$$V(x) = -\delta(x)V_0 \quad (3.5)$$

with $V_0 > 0$. With this simplification there is exactly one linear bound state for all potential depths. Therefore, we use an ansatz that splits the total wave function

$$\psi = \psi_s + \psi_t. \quad (3.6)$$

into a free soliton (see Eq. 2.30)

$$\psi_s = A_s \operatorname{sech}(A_s x - Q_s) e^{i\Phi_s} e^{iV_s x} \quad (3.7)$$

and a trapped part

$$\psi_t = A_t \operatorname{sech}(x/a_t) e^{i\Phi_t} e^{i\sigma_t \log[\cosh(x/a_t)]} \quad (3.8)$$

that models a nonlinear mode that is localised at the well. Here we assume that, for small values of V_0 , the trapped soliton solution can be approximated by a free stationary soliton with a particular form of a chirping term $\log[\cosh(x/a_t)]$, which is capable of describing breathing modes. This can be used as a substitute for radiation effects which should allow the soliton to be trapped as the chirping term can transfer kinetic energy into another form of excitation. The choice for this particular form of the chirping term is consistent with Ref. [62] where it has been shown to be suitable for soliton scattering. The system's Lagrangian is given by

CHAPTER 3. BRIGHT SOLITON SCATTERING WITH GROSS-PITAEVSKII

$$L = \int_{-\infty}^{\infty} dx \left\{ \frac{i}{2} \left(\psi^\dagger \frac{\partial}{\partial t} \psi - \psi \frac{\partial}{\partial t} \psi^\dagger \right) - \frac{1}{2} \left| \frac{\partial}{\partial x} \psi \right|^2 + \frac{1}{2} |\psi|^4 - V(x) |\psi|^2 \right\}.$$

This Lagrangian can not be integrated analytically due to cross terms in the integrand. However, it has been suggested to neglect all cross terms that are not connected to the delta function [63]. This can be partly justified because typically those cross terms are highly oscillatory. Therefore they can be considered to be much smaller than the other terms after the integration. Brief numerical calculations seem to verify this assumption. That leads us to the approximate Lagrangian, which is given by

$$\begin{aligned} L \approx & -2A_t^2 a_t \dot{\Phi}_t - 2A_t^2 a_t \dot{\sigma}_t (2 - \log(4)) + 2A_t^2 \dot{a}_t \sigma_t - \frac{1}{3} \frac{A_t^2}{a_t} (1 + \sigma_t^2) + \frac{2}{3} A_t^4 a_t \\ & - 2A_s \dot{\Phi}_s - 2\dot{V}_s Q_s + \frac{1}{3} A_s^3 - A_s V_s^2 \\ & + V_0 \{ A_t^2 + A_s^2 \operatorname{sech}^2(Q_s) + 2A_t A_s \operatorname{sech}(Q_s) \cos(\Phi_s - \Phi_t) \}. \end{aligned} \quad (3.9)$$

To obtain the equations of motion one has to solve the Euler-Lagrange equations

$$\frac{d}{dt} \left(\frac{\partial L}{\partial \dot{q}_i} \right) = \frac{\partial L}{\partial q_i} \quad (3.10)$$

for $q_i = A_s, \Phi_s, Q_s, V_s, A_t, \Phi_t, a_t, \sigma_t$.

This leads to

$$\begin{aligned}
 \frac{d}{dt}A_s &= V_0 A_s A_t \operatorname{sech}(Q_s) \sin(\Phi_s - \Phi_t) \\
 \frac{d}{dt}\Phi_s &= \frac{1}{2}(A_s^2 - V_s^2) + V_0 [A_s \operatorname{sech}^2(Q_s) + A_t \operatorname{sech}(Q_s) \cos(\Phi_s - \Phi_t)] \\
 \frac{d}{dt}Q_s &= A_s V_s \\
 \frac{d}{dt}V_s &= -V_0 [A_s^2 \operatorname{sech}^2(Q_s) \tanh(Q_s) + A_s A_t \operatorname{sech}(Q_s) \tanh(Q_s) \cos(\Phi_s - \Phi_t)] \\
 \frac{d}{dt}a_t &= \frac{\sigma_t}{3a_t} + (2 - \log(4)) \frac{V_0}{A_t} A_s \operatorname{sech}(Q_s) \sin(\Phi_s - \Phi_t) \\
 \frac{d}{dt}\sigma_t &= \frac{1}{3a_t^2}(1 + \sigma^2) - \frac{A_t^2}{3} - \frac{V_0}{2a_t} + \frac{V_0}{2A_t a_t} A_s \operatorname{sech}(Q_s) [2\sigma_t \sin(\Phi_s - \Phi_t) - \cos(\Phi_s - \Phi_t)] \\
 \frac{d}{dt}\Phi_t &= -\dot{\sigma}_t(2 - \log(4)) + \frac{\dot{a}_t \sigma_t}{a_t} - \frac{1}{6a_t^2}(1 + \sigma_t^2) + \frac{2}{3}A_t^2 \\
 &\quad + \frac{V_0}{2A_t a_t} [A_t + A_s \operatorname{sech}(Q_s) \sin(\Phi_s - \Phi_t)]. \tag{3.11}
 \end{aligned}$$

Two of these eight dynamical variables can be eliminated due to conservation laws. Hence, the amplitude A_t can be found from the normalisation of the wave function

$$\mathcal{N}_0 = 2A_s + 2A_t^2 a_t, \tag{3.12}$$

since \mathcal{N}_0 is a constant of the motion. We obtain

$$A_t = \sqrt{\frac{\mathcal{N}_0}{2} - \frac{A_s}{a_t}}. \tag{3.13}$$

Furthermore, it is not necessary to calculate Φ_t and Φ_s separately as the only interesting and physically important property is the phase difference

$$\Delta\Phi = \Phi_t - \Phi_s. \tag{3.14}$$

We note that the total phase $\Phi_t + \Phi_s$ has a trivial time dependence since it is canonically conjugate to the total energy (Hamiltonian), which is another constant of motion. This way the problem to solve consists of six coupled first-order ordinary differential equations.

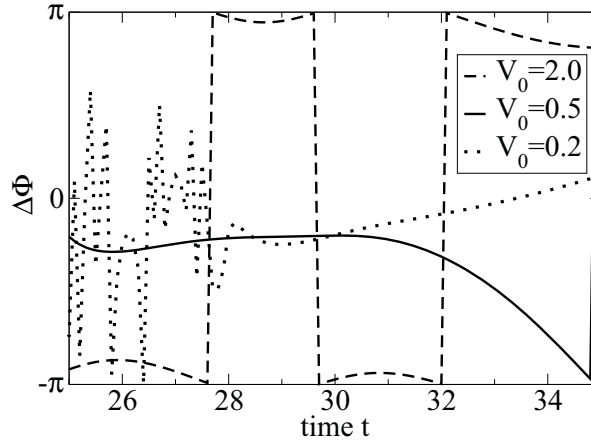


Figure 3.8: The phase difference $\Delta\Phi$ for different potential depths and for the time when the incoming soliton reaches the quantum well at $t \approx 30$ [see Eq. (3.11)]. The solid line and the dotted line show clearly a phase difference close to 0. This is where transmission and trapping occurs respectively. An example for reflection with a turning point at $t \approx 29$ is given by the dashed line where $\Delta\Phi \approx \pm\pi$.

3.3.2 Numerical results

This ansatz allows us to calculate the time dynamics of a soliton without solving the Gross-Pitaevskii equation directly. But, of course, this is still a very simple approximation and thus the results are not expected to be as accurate as the GP results. However, they can give further insight into the mechanism involved. As in the previous section, the initial velocity is set to $v_{\text{initial}} = 0.3$ and the initial position of the soliton is $Q_s = -10$. We choose physically reasonable, small initial values for the parameters of the trapped mode ($A_t = 10^{-4}$ and $a_t = 10^{-2}$) in order to avoid numerical divergences. Furthermore, we use $\Delta\Phi = 0$ at $t = 0$, yet we find that the results are not dependent on this initial choice.

Fig. 3.8 shows the phase difference $\Delta\Phi$ for different V_0 during the scattering process. For $V_0 = 0.2$ the soliton is being transmitted and we find $\Delta\Phi \ll 1$. Increasing the potential depth to $V_0 = 0.5$ results in (partial) trapping and $\Delta\Phi \ll 1$ while for a even larger $V_0 = 2$ there is full reflection ($\Delta\Phi \approx \pm\pi$). From Eq. (3.11) we can see that the time dependence of the velocity V_s strongly depends on $\cos(\Delta\Phi)$.

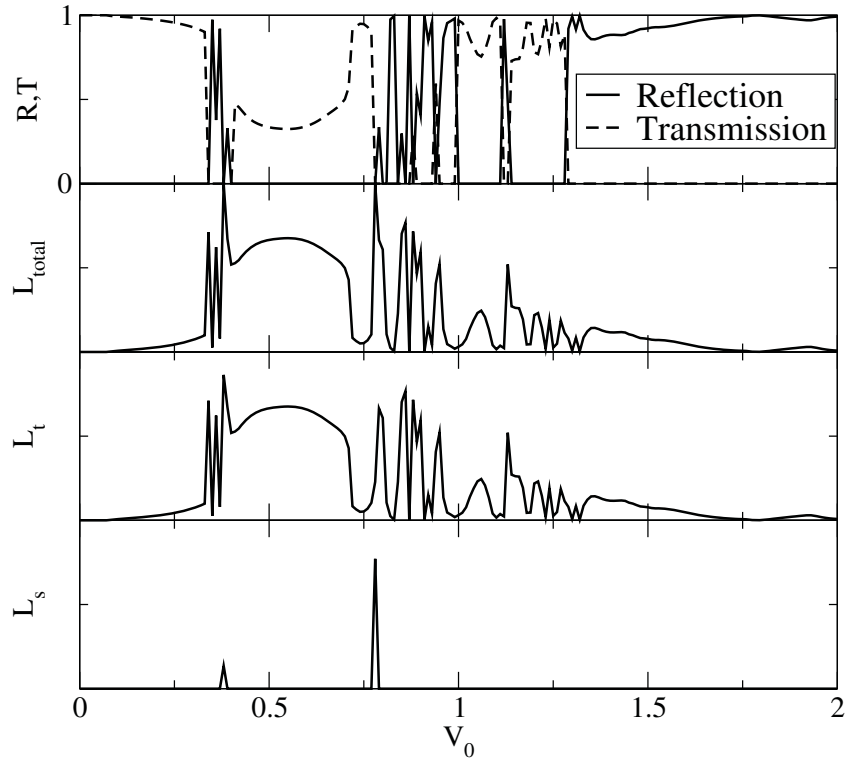


Figure 3.9: Results for soliton scattering on a quantum well from the collective coordinate Eq. (3.11). From top to bottom: Reflection R and transmission T versus V_0 , the total trapping L_{total} , fraction L_t in the trapping mode, fraction L_s in the soliton mode as a function of the potential depth V_0 .

CHAPTER 3. BRIGHT SOLITON SCATTERING WITH GROSS-PITAEVSKII

At all times we find that for a small phase difference the velocity does not change sign for all times, and therefore the soliton is transmitted or gets trapped. In the other case of $\Delta\Phi \approx \pm\pi$ the soliton is reflected from the well as the sign of the velocity can change. The reason for either trapping or transmission, however, is found in the potential depth that determines how fast the trapped mode can be populated, i.e. large values for V_0 result in a faster population as can be seen in Eq. (3.11) for \dot{A}_s and \dot{a}_t . Therefore, we can find a band between the reflection and the transmission regime where trapping can occur.

It is a well-known feature of collisions between bright solitons that a π -phase difference induces repulsion [131]. Further discussions can be found in Ref. [66]. In particular π -phase difference avoids trapping. Conversely, a resonant process with a small phase difference is responsible for the population of the trapped mode. This is consistent with the findings of the previous section where trapping was described as a resonant process.

To complete the comparison with the previous section, Fig. 3.9 shows the reflection R , trapping L and transmission T as a function of the potential depth V_0 . We see similar features as in Fig 3.3. For very small V_0 the soliton is almost completely transmitted (Fig. 3.10a) while for large V_0 full reflection (Fig. 3.10e) is observed. In-between both of these regimes we find a more complicated and interesting behaviour. Most of the time partial trapping of the soliton is observed after the scattering event. Furthermore, we find two different forms of trapping. In the first case, the trapping mode is populated by the incoming soliton as expected, while the remaining fraction in the soliton mode is moving away from the well to either positive or negative infinity (see Fig. 3.10b and 3.10c). In addition, another kind of trapping can be observed. In this situation the soliton mode oscillates around the delta potential (Fig. 3.10d). According to the numerical simulations this is the only event when full trapping occurs.

We conclude that the basic ideas from the previous section are still valid: For small V_0 there is full transmission, then (partial) trapping and for very large V_0 the soliton reflects completely.

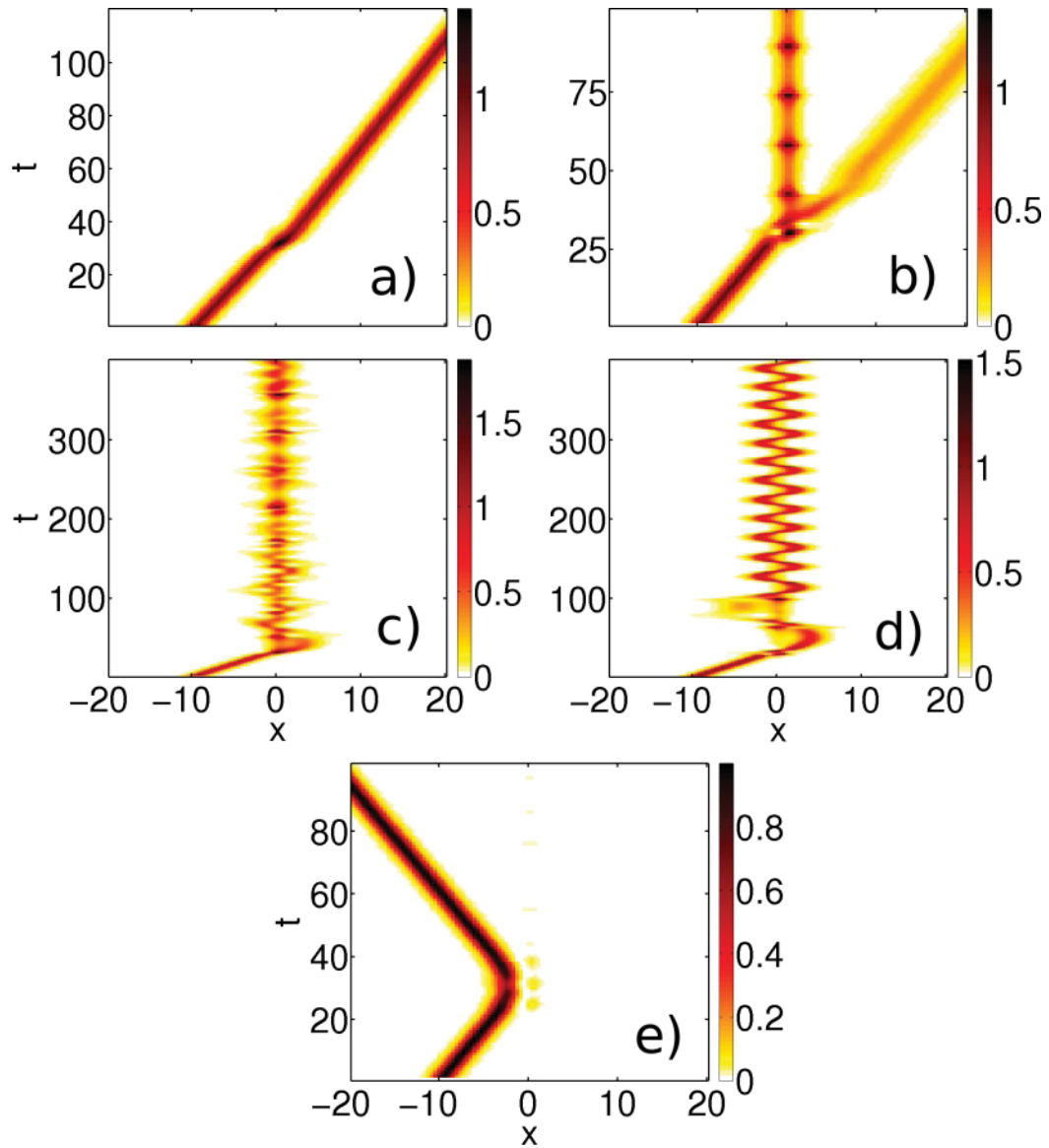


Figure 3.10: Condensate density as a function of time as a result of solving Eqs. (3.11), analogous to Fig. 3.5. For $V_0 = 0.2$ panel a) shows the typical situation of a fully transmitted soliton. Partial trapping at $V_0 = 0.7$ is shown in b). Panels c) and d) present the cases for $V_0 = 0.38$ and $V_0 = 0.78$. In c) the soliton is being trapped by population of the trapped mode. The soliton sloshes around the well for d) while populating the soliton mode only. The last plot for $V_0 = 1.75$ shows the whole soliton being completely reflected.

3.4 The trapping process

3.4.1 Analytical model

In order to study the role of energy conservation and radiation in the trapping process more closely, we consider the GP energy functional [46]

$$E[\psi(x)] = \int dx \left[\frac{1}{2} \left| \frac{\partial}{\partial x} \psi(x) \right|^2 + V(x) |\psi(x)|^2 + \frac{g}{2} |\psi(x)|^4 \right]. \quad (3.15)$$

We split this energy into different energy terms

$$E[\psi] = E_{kin}^d + E_{kin}^v + E_{int}. \quad (3.16)$$

These are defined as

$$\begin{aligned} E_{kin}^d &\equiv \int dx \left[\frac{1}{2} \left| \frac{\partial |\psi(x)|}{\partial x} \right|^2 \right] \\ E_{kin}^v &\equiv \int dx \left[\frac{1}{2} \left| \psi(x) \frac{\partial}{\partial x} \exp[i\theta(x, t)] \right|^2 \right] \\ E_{int} &\equiv \int dx \left[\frac{g}{2} |\psi(x)|^4 \right] \end{aligned} \quad (3.17)$$

with $\psi(x) = |\psi(x)| \exp[i\theta(x, t)]$. The first term gives the contribution to the kinetic energy from the density variations (E_{kin}^d) while the second term represents a contribution from the phase gradient (E_{kin}^v), which is connected to the superfluid velocity (see Eq. 2.14). E_{int} is the interaction energy. Specifically for the soliton solution ψ_s from Eq. (2.30) we find

$$E_{kin}^d = \frac{1}{3} \sqrt{-g} A^3, \quad E_{kin}^v = \frac{A}{\sqrt{-g}} v^2, \quad E_{int} = -\frac{2}{3} \sqrt{-g} A^3 \quad (3.18)$$

and hence for the total energy

$$E[\psi_s] = -\frac{\sqrt{-g}}{3} A^3 + \frac{A}{\sqrt{-g}} v^2. \quad (3.19)$$

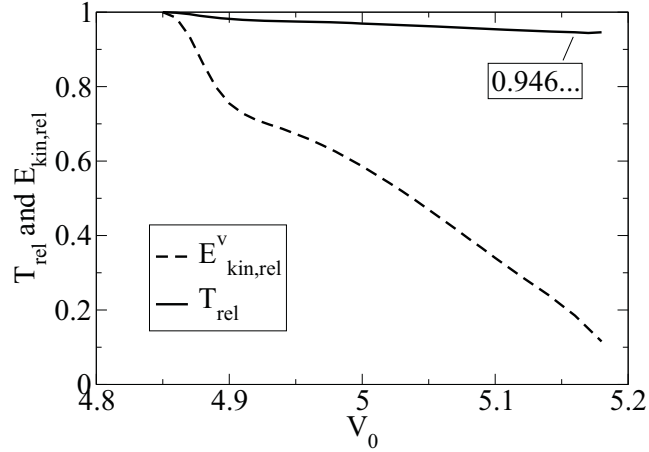


Figure 3.11: Transmission $T_{\text{rel}}(V_0) = T(V_0)/T(4.85)$ and velocity contribution to the kinetic energy $E_{\text{kin,rel}}^v(V_0) = E_{\text{kin}}^v(V_0)/E_{\text{kin}}^v(4.85)$ relative to the values at $V_0 = 4.85$ where transmission is maximal. As the transmitted fraction of the incoming soliton decreases for deeper wells, so does its velocity v_t .

In particular, we find the universal ratio

$$\frac{E_{\text{int}}}{E_{\text{kin}}^d} = -2 \quad (3.20)$$

for a soliton solution. If this ratio differs from -2 we know that the wave function can not have the same form as the soliton solution.

We now show that radiation loss during a scattering event leads to a decreased velocity due to energy conservation. We consider a soliton (2.15) with initial velocity v_i that, during a collision event, suffers a small loss in amplitude due to 'radiation', i.e. small amplitude waves spreading away from the soliton. The amplitude is reduced by the effect of radiation to $A_t = A - \epsilon$ with $0 < \epsilon \ll A$.

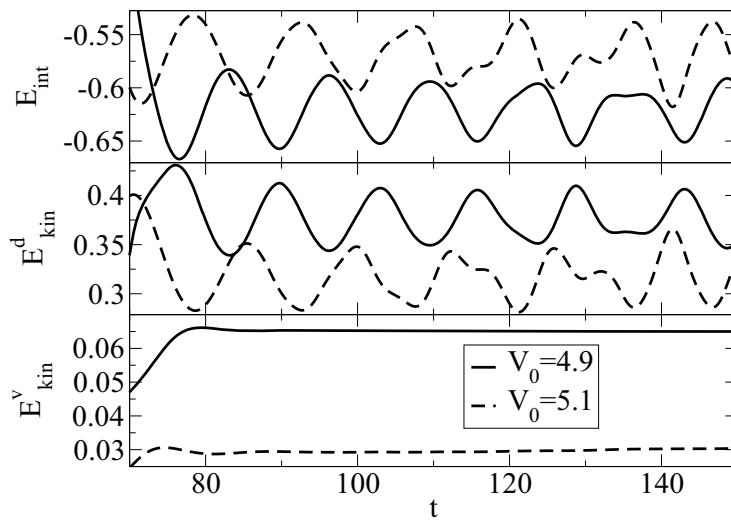


Figure 3.12: Time dynamics of different kinetic and interaction energies for the transmitted part of the soliton for $V_0 = 4.9$ (solid line) and $V_0 = 5.1$ (dashed line) well after the collision ($t \approx 45$). The soliton undergoes breathing oscillations after the scattering process that can be identified as oscillations in the energy. For deeper wells E_{kin}^v becomes smaller, i.e. the velocity of the transmitted soliton v_t is smaller.

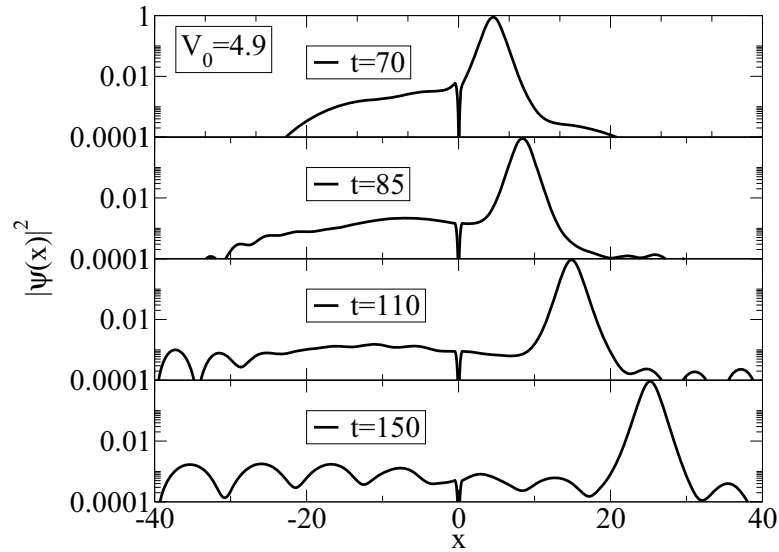


Figure 3.13: Logarithmic density plot of the condensate for different times at $V_0 = 4.9$. A reflected component (radiation) is clearly visible.

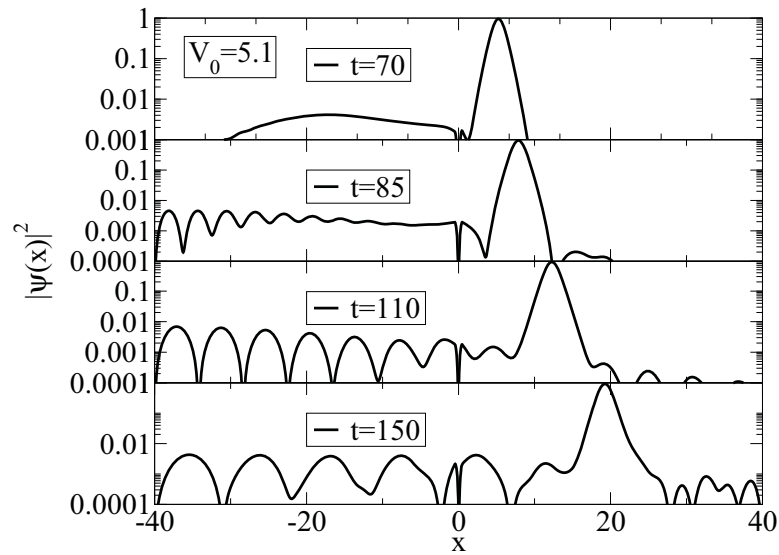


Figure 3.14: Logarithmic density plot of the condensate for different times at $V_0 = 5.1$. Compared to Fig. 3.13 the reflected part is clearly larger.

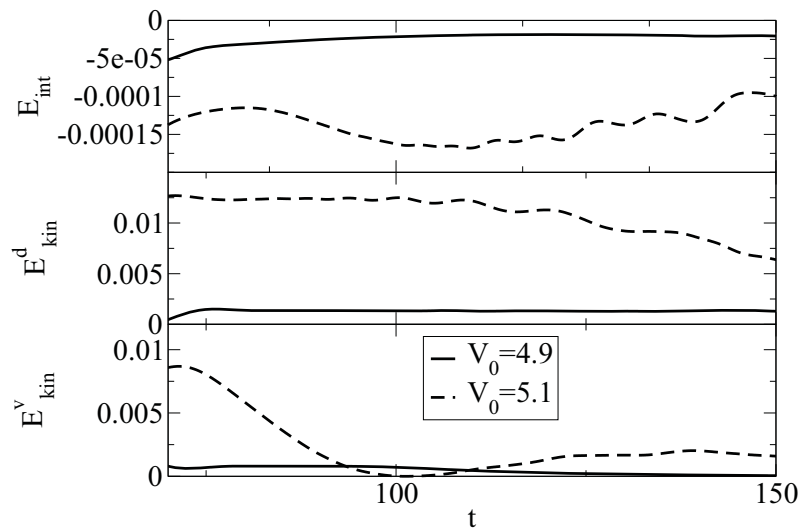


Figure 3.15: Time dynamics of different kinetic and interaction energies for the reflected part of the soliton for $V_0 = 4.9$ and $V_0 = 5.1$. The ratio $|E_{\text{int}}/E_{\text{kin}}^d| \ll 1$ is different to what one expects from a soliton. As the interaction energy is small the reflected part is mainly radiation. This is only valid in the regime where the soliton is almost fully transmitted or fully trapped. Once the reflected part becomes larger, the ratio becomes $|E_{\text{int}}/E_{\text{kin}}^d| = 2$ again.

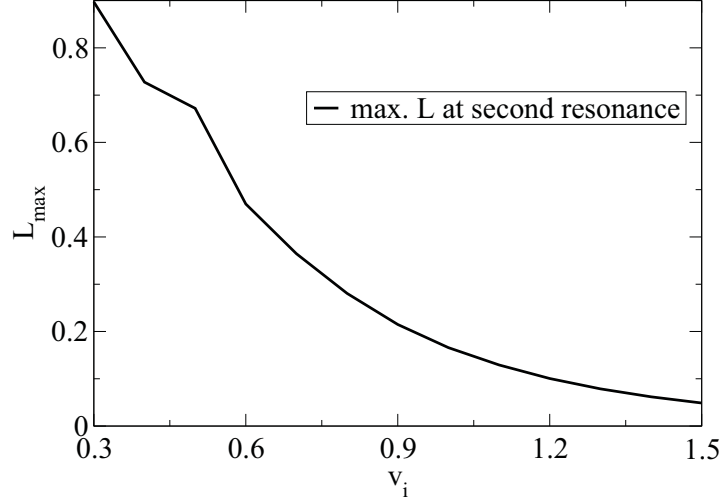


Figure 3.16: The plot shows the maximum fraction of atoms L_{\max} that can be trapped around the second transmission resonance. L_{\max} drops significantly with increasing velocity v_i as proposed by Eq. (3.21).

The energy of the transmitted soliton travelling with velocity v_t is given by

$$\begin{aligned}
 E_t[\psi] &= -\frac{\sqrt{-g}}{3}(A - \epsilon)^3 + \frac{(A - \epsilon)}{\sqrt{-g}}v_i^2 \\
 &= \left[-\frac{\sqrt{-g}}{3}A^3 + \frac{A}{\sqrt{-g}}v_i^2 \right] + \sqrt{-g}A^2\epsilon \\
 &\quad - \frac{A}{\sqrt{-g}}v_i^2\epsilon + \frac{2A}{\sqrt{-g}}v_i\delta v + O(\epsilon^2) + O(\delta v^2), \tag{3.21}
 \end{aligned}$$

where the result has been linearised in ϵ and $\delta v \equiv v_t - v_i$. Identifying the term in square brackets as the energy of the initial soliton and assuming that radiation loss carries away a positive amount of energy (since the only negative contributions to energy could come from the negative nonlinear term, which is negligible for small densities), we realise that the linear term in Eq. (3.21) must be negative due to energy conservation. For $v_i^2 < -gA$ (which is the case in our simulations), we can derive the relation

$$v_t \leq v_i + \frac{v_i}{2}\epsilon - \frac{-gA}{2v_i}\epsilon < v_i \tag{3.22}$$

CHAPTER 3. BRIGHT SOLITON SCATTERING WITH GROSS-PITAEVSKII

since $\epsilon > 0$. The slowing down of solitons after the collision can be seen in Fig. 3.11, which compares the velocity part of the kinetic energy $E_{kin}^v \propto v_t^2$ to the transmission.

The same parameters are used as in Fig. 3.3, where the transmission window was found between $V_0 = 4.85$ and $V_0 = 5.2$. Fig. 3.11 shows that a small change in the transmission ($\approx 5\%$) results in a strong decrease of the transmitted soliton's velocity v_t ($\approx 70\%$). Extrapolating Eq. (3.22) beyond the regime of small ϵ we find that

$$\epsilon \approx \left(\frac{-gA}{2v_i^2} - \frac{1}{2} \right)^{-1} \quad (3.23)$$

leads to $v_t \approx 0$, which allows the soliton to be trapped in the well.

For $v_i > \sqrt{\frac{-g}{2}(1+A/2)^{-1}A}$ we find that the right hand side of Eq. (3.22) is always positive as $\epsilon \leq A$. Therefore, we expect that trapping is reduced until it vanishes for very high velocities v_i when kinetic energy dominates over nonlinear energy contributions. Then the system becomes approximately linear and can be approximated by a non-interacting system of particles see (Fig. 3.7).

In Figs. 3.11-3.15 we show results for the energy contributions after the soliton-well collision. In particular, Fig. 3.12 gives energy contributions of the transmitted part of the soliton after the collision. There we can find that $\frac{E_{int}}{E_{kin}^d} \approx -2$. The curves show oscillations in energy which can be explained due to breathing excitations of the soliton after the collision with the well. In the bottom panel E_{kin}^v is given for two V_0 . We find again that the velocity v_t decreases for larger V_0 .

Pictures of the condensate density for different times are given in Figs. 3.13 and 3.14. The incoming soliton transmits almost completely through the well, only a small portion is reflected and can be described as radiation. Furthermore, both figures show once more that the radiation increases for deeper wells, i.e. the transmitted fraction is reduced.

Next, we look at the reflected part in Fig. 3.15. There the ratio between interaction and the density contribution to the kinetic energy is

$$\left| \frac{E_{int}}{E_{kin}^d} \right| \ll 1. \quad (3.24)$$

Comparing to Eq. (3.20) this clearly indicates that the reflected part in this regime

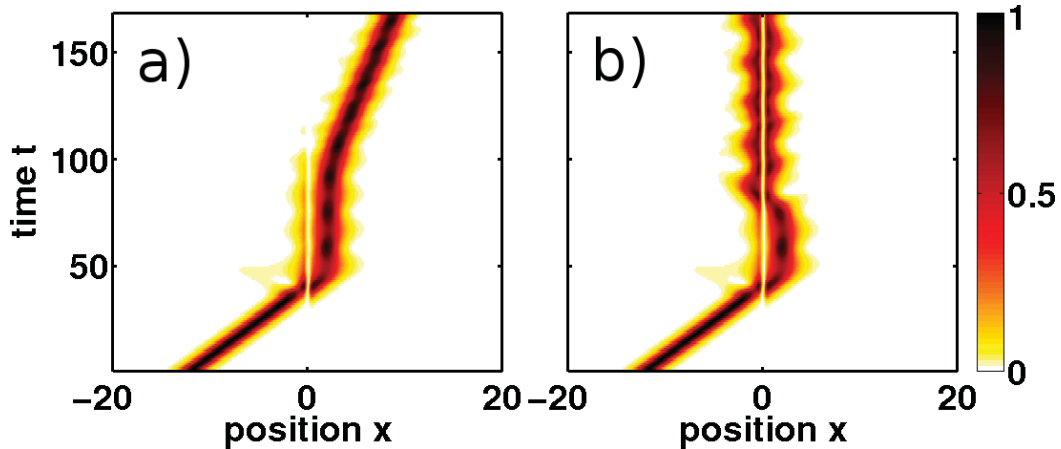


Figure 3.17: Density plot for $V_0 = 5.182$ in a) and $V_0 = 5.183$ in b) ($l_{box} = 40$). In part a) the soliton decelerates and remains at the edges of the well before it continues to move to the right hand side. In b) the soliton slows down and remains at the edges of the well before it moves back to get trapped by the well.

is not soliton-like. Instead, the almost vanishing absolute value for the interaction term shows that the main contribution, the kinetic energy, is being carried by radiation as proposed in [66].

The findings in this section help to understand the finite width of the transmission bands that we found in Sec. 3.2. If v_i decreases the width of the transmission bands decreases as well, because less radiation is needed to trap the soliton.

We illustrate the transmission and trapping behaviour at the critical point for V_0 in Figure 3.17.

Furthermore, we want to note that strictly speaking trapping is not a resonant elastic process. The reflected small amplitude waves with positive kinetic energy are clearly responsible for the trapping. Therefore, trapping is actually a “resonant energy loss” process.

3.4.2 Temporal trapping

In addition to the trapping process described above, there is a second mechanism to trap a soliton which is similar to the temporary trapping of a linear wave packet. It occurs at the boundary between reflection and transmission regions

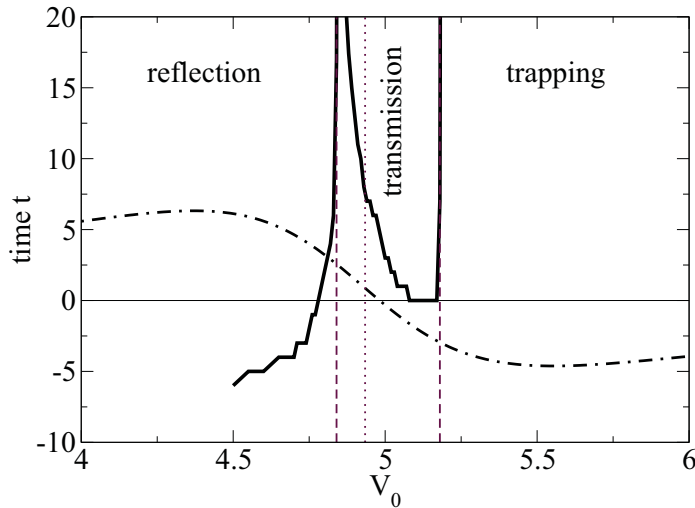


Figure 3.18: Time delay of the soliton due to the existence of the potential well (solid line). These are results for the simulations in Sec. 3.2. Near the transition point from full reflection to full transmission (left vertical dashed line) the time delay, given by Eq. (3.25), increases very fast and becomes very large. This means the soliton remains in the vicinity of the trap on a very long time scale. Within the transmission region it decreases again until the trapping mechanism kicks in (right vertical dashed line). This picture for the nonlinear regime differs from the analytically calculated time delay for the linear case (dashed-dotted line) not only in the position and value of its maximum but also for the non-existent negative time delay (right of the dotted vertical line).

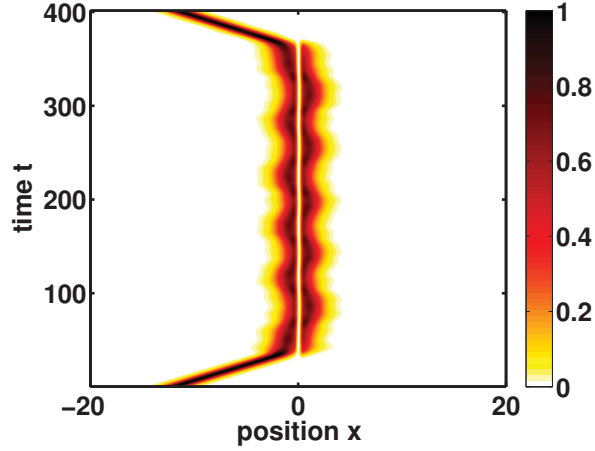


Figure 3.19: Density plot for $V_0 = 4.842$ ($l_{box} = 40$). The soliton decelerates and more than 99% of the initial soliton is trapped for a long time period (see also Fig. 3.18). This is connected to a temporary trapping of a linear wave packet.

where radiation is negligible. For this situation we find that the soliton remains in the well for some time t_d until it reflects. We can measure this time delay t_d as the time the centre of mass reaches the centre of the well for the first time until it leaves the centre again. Furthermore, we see that by carefully adjusting the potential depth, t_d can be large enough to observe a temporary trapped soliton in experiments. Fig. 3.18 shows the delay of the soliton during the transition through the well. It is remarkable that the whole soliton can be trapped with negligible losses due to radiation ($> 99\%$). The losses are indeed much smaller than for the first trapping mechanism described before. The time evolution of the density given in Fig. 3.19 shows an example of the temporal trapping of the soliton. This delay within the well is analogous to the interaction free case for a travelling wave packet with velocity v towards a well. There, an analytical expression for the time delay is known [130] as

$$t_d^{lin} = \frac{\partial}{\partial E} \left[\arctan \left(\frac{1}{2} \frac{\sqrt{E}}{\sqrt{E+V_0}} \tan \left(\sqrt{2(E+V_0)} \right) \right) \right]_{E=v^2/2}, \quad (3.25)$$

which is shown in Fig. 3.18. This delay can be explained as a temporary trapping of the linear wave packet. During the time the soliton is trapped, it oscillates between both ends of the well before it escapes again. However, due to the nonlinearity, the position and the value for the maximum time delay differ significantly from the linear case. Furthermore, the time delay of Eq. (3.25) becomes negative, which happens if the quantum well is deep enough to turn a quasi-bound state into a bound state which is in contrast to the nonlinear case. One should however note that in the linear case about 42% of the wave packet reflects at the point of maximal time delay. For smaller velocities this value seems to converge towards 50%. In addition, the maximum time delay for the linear case lies well below the one for the nonlinear case, where it seems to diverge at the critical value for V_0 . Therefore, the connection to the nonlinear case remains unclear and needs further investigations that go beyond the scope of this work.

We want to remark that, although this would be an elegant way for lossless trapping of a soliton, Fig. 3.18 also shows that the potential depth associated with a long delay time has to be chosen very accurately. Therefore this type of trapping is harder to realise and to observe experimentally. In a BEC experiment with a small enough number of atoms it should be expected that superposition states will occur in this region [28]. Hence, the other trapping method is favourable when it comes to experiments, even though one has to take into account minor losses.

3.5 Probing energy levels

Trapping of a soliton is sensitive to bound states in the well. Data presented in the previous sections has already suggested that trapping results from a resonant interaction of the soliton with a stationary defect mode. The relevant energy scale is the soliton's chemical potential. By exploiting this resonant relationship, we are able to extract the bound-state energy by analysing soliton scattering data. We proceed by comparing the scaled particle number of nonlinear bound state solutions with the trapped component after scattering a soliton with the same chemical potential.

In this section we model the defect as an attractive delta potential $V(x) = -V_0\delta(x)$, which has only one bound state at $E_b = -V_0^2/2$. We solve Eq. (2.15) for

$g = -1$ with a soliton initial wave function (2.30). We vary the amplitude A and thus the chemical potential $\mu = gA^2/2$. After the soliton has been scattered, we integrate the scaled particle number $N_L = \int_{-b}^b |\psi|^2 dx$ of the trapped component (choosing b such as to capture at least 99% of the initial soliton's normalisation). In Fig. 3.20 we compare this data with the normalisation $N_S = \int |\phi|^2 dx$ of a stationary localised solution $\psi(x, t) = \phi(x) \exp(i\mu_s t)$ of Eq. (2.15) with the same chemical potential $\mu_S = \mu$. We find the analytical expression

$$N_S = 2 \left(\sqrt{-2\mu} - V_0 \right), \quad (3.26)$$

as seen in Fig. 3.20. The energy E_b of the linear bound state [of Eq. (2.15) with $g = 0$] is found at the intersection of the line with the μ axis, i.e., $E_b = \mu$ at $N_S = 0$.

As expected, trapping is observed in the time-dependent simulation only for $\mu \gtrsim E_b$ (Figs. 3.20 and 3.21) with the scaled particle number increasing for decreasing μ , roughly following Eq. (3.26). As seen in Fig. 3.20, the trapped component is systematically about 20% larger than expected from the exact stationary solution. We have verified that the final state of the trapped component in the time-dependent simulations corresponds to a stationary solution with further reduced chemical potential compared to the initial μ . This behaviour can not be explained yet because of non-trivial time-dependent variations from nonlinear effects. We hope that in the future new methods make a systematic study of the differences in trapping accessible. Fortunately, we obtained enough important information from recording the trapped component as a function of μ to allow us to locate the bound-state energy E_b .

In Fig. 3.21 we have plotted the trapped component as a function of the soliton's initial chemical potential μ for different trapping potentials. Least square fits of the data (for convenience only data points with $N_L > 0.003$ were included) to the functional form $N_{\text{fit}} = \alpha \sqrt{\beta - \mu}$, where α and β have to be determined. This fit provides estimates β for the bound state energy $E_b = \mu$.

We expect that bound state energy levels of narrow potential wells of more general shape than the one studied here could be probed experimentally by scattering bright solitons using this scheme. For defects with more than a single linear

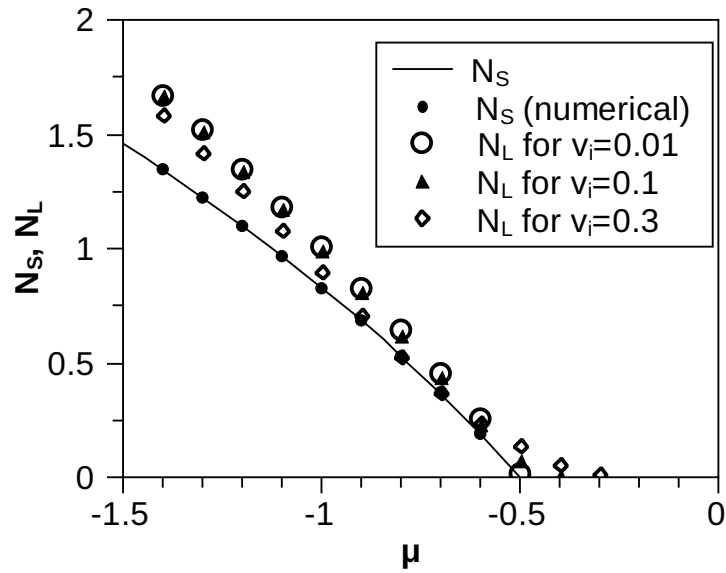


Figure 3.20: The scaled number of trapped atoms N_L versus μ from time-dependent simulations of Eq. (2.15) is compared with $N_S(\mu)$ for stationary solutions from Eq. (3.26). Stationary solutions were also found with our numerical code for checking numerical accuracy. Results taken over a range of initial velocities v_i show a consistent picture. The most significant deviations occur at the onset of trapping around the location of the linear bound state at $E_b = \mu = -0.5$. This feature is most clearly distinguished for the smallest velocities.

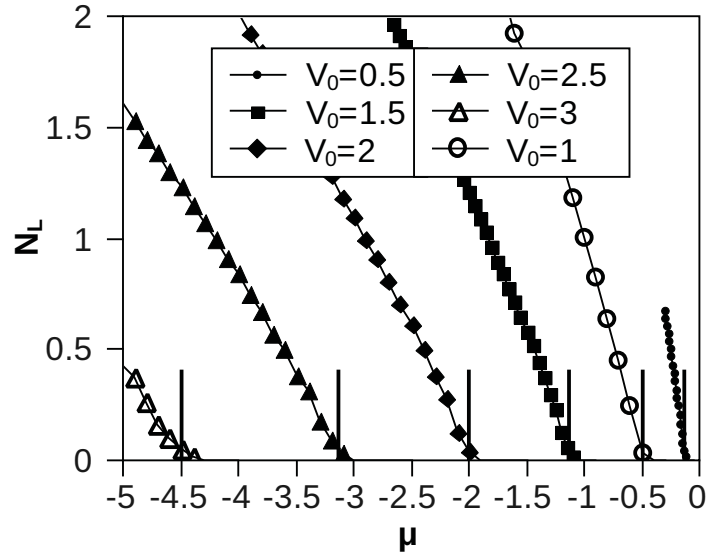


Figure 3.21: Scaled particle number of the trapped component N_L versus μ after soliton-defect scattering as in Fig. 3.20 for different values of the defect strength V_0 . Short vertical lines indicate the energy of the bound state E_b for each of the values of V_0 . Square-root fits (as explained in the text) provide estimates β for E_b from the scattering data. Values for β found are -0.120 , -0.505 , -1.12 , -1.97 , -3.08 , -4.43 , which correspond to the analytical values for E_b given by -0.125 , -0.5 , -1.125 , -2 , -3.125 , -4.5 , respectively.

bound state, we expect that only the least strongly bound one can be detected in this manner. This is supported by the results of Sec. 3.2 that were obtained with a well with multiple bound states.

3.6 Summary

In this chapter we investigated the scattering of a bright matter-wave soliton on a narrow linear defect within the mean-field Gross-Pitaevskii approach. We considered the regime of solitons with small velocity such that nonlinear energy scales dominate over the kinetic energy. From numerical simulations shown in Sec. 3.2, we found that solitons can be reflected, transmitted and trapped, which is strongly influenced by the energy level structure of the defect. This is analogous to the single-particle case, where the solutions of the linear Schrödinger equation show that a coupling of the incoming wave with (quasi-) bound states in the well lead to partial transmission and reflection. However, in contrast to the scattering of linear waves, the transitions between minimal and maximal transmission are not smooth, but we found that the nonlinear interactions lead to abrupt changes in the transmission instead. Even more importantly, part of the incoming soliton can now be trapped above the well by populating bound states or nonlinear localised modes in the well. The nature of these resonant processes were verified in Sec. 3.3 by solving a variational collective-coordinate two-mode model, which shows that the soliton transmits or is trapped once the eigenfrequency of the incoming soliton is in resonance with a bound state.

In addition, we derived an analytical expression in Sec. 3.4 to describe the trapping as a consequence of radiation of matter. The requirement of energy conservation then ultimately leads to the conclusion that the transmitted soliton's velocity decreases for increasing radiation which eventually leads to trapping. Therefore, during the trapping process occurs both, a resonant energy transfer to a bound state as well as a resonant energy loss process.

At last, an application for our findings was proposed for an experimental probing mechanism to find bound states of an unknown localised potential well.

The important thing is not to stop questioning. Curiosity has its own reason for existing.

Albert Einstein

4

MCTDH - simple improvements due to rescaling of the interaction

When tuning the interactions from weak to strong in a one-dimensional system, the bosons undergo a crossover from a Bose-Einstein condensate to the fermionised and strongly correlated Tonks-Girardeau (TG) gas (see Sec. 2.4.1). This system is well suited to benchmark computational many-body methods as exact results are available from integrable models in the limits of infinite interactions (TG) or a vanishing external potential (Lieb-Liniger model, see Sec. 2.4.2). Previous calculations of the ground state with exact diagonalisation in a fixed product basis [82, 132, 133] and with the MCTDH method [134, 135] have shown that for finite values of the interaction strength the results give a reasonable approximation of the completely fermionised state, which in exact theory is only reached for infinite interaction. Our calculations with the MCTDH method show that larger values of the interaction produce worse results in the calculation for the energy and lead to spuriously enhanced density oscillations.

This is due to the previously mentioned methods using a truncated Hilbert space. This leads to errors, and therefore elaborate schemes have previously been developed to generate effective Hamiltonians that remove this problem. However, these techniques are cumbersome and require careful application [31, 136–139]. A simpler, yet powerful method is desirable to accurately describe different interacting regimes for a variety of applications [140–143]. Here we present a rescaling method that increases the accuracy or decreases the required Hilbert space by

CHAPTER 4. MCTDH - SIMPLE IMPROVEMENTS DUE TO RESCALING OF THE INTERACTION

mapping the interaction in the simulations to the physical interaction. This approach is closely related to the known renormalisation of the two-body T matrix but extends this method into the strongly-interacting regime. Therefore, numerical simulations can be sped up and used to approach previously inaccessible regimes and systems.

Sec. 4.1 of this chapter studies the convergence properties and errors for calculations on a bosonic system with MCTDH (see Sec. 2.6). In Sec. 4.2 we demonstrate how the rescaling of the contact interaction can preserve the low-lying energy spectrum and long-wavelength structure of wave functions in one-dimensional systems. Its analytic expression is found for a two-particle system. Furthermore, we compare finite Hilbert-space calculations and exact results, obtained in the strongly interacting regime for up to five particles, and show that rescaling can significantly improve the accuracy of numerical calculations in harmonic and double-well confinements. In addition to ground-state energies, the low-lying excitation spectrum, density profile and correlation functions are studied. This shows that time-dynamical simulations can make use of the rescaling as well. An article on the results in Sec. 4.2 was published as Ref. [95].

4.1 Convergence studies

In this section we present studies on $N = 3$ bosons in a one-dimensional ring of length L using the Heidelberg MCTDH package [91]. The observables are scaled according to $\tilde{z} = L$ and $\tilde{E} = E_0 = 2\pi^2\hbar^2/(mL^2)$ (see Sec. 2.3). Here, E_0 is the energy of the first excited state for a single particle in the ring and $x = z/\tilde{z} \in [0, 1]$ (for the spatial coordinate z).

As already stated in 2.6, MCTDH is capable of simulating any kind of interaction potential between particles. However, unlike MCTDHB/QiwiB, there is no direct implementation of the specific contact interaction $V(x) = g\delta(x)$. Instead, it is approximated by a Gaussian function, which is given by

$$\delta_\sigma(x) = \frac{1}{\sqrt{2\pi}\sigma} e^{-x^2/2\sigma^2}. \quad (4.1)$$

Here, σ determines the width of the Gaussian function. For $\sigma \rightarrow 0$ the Gaussian

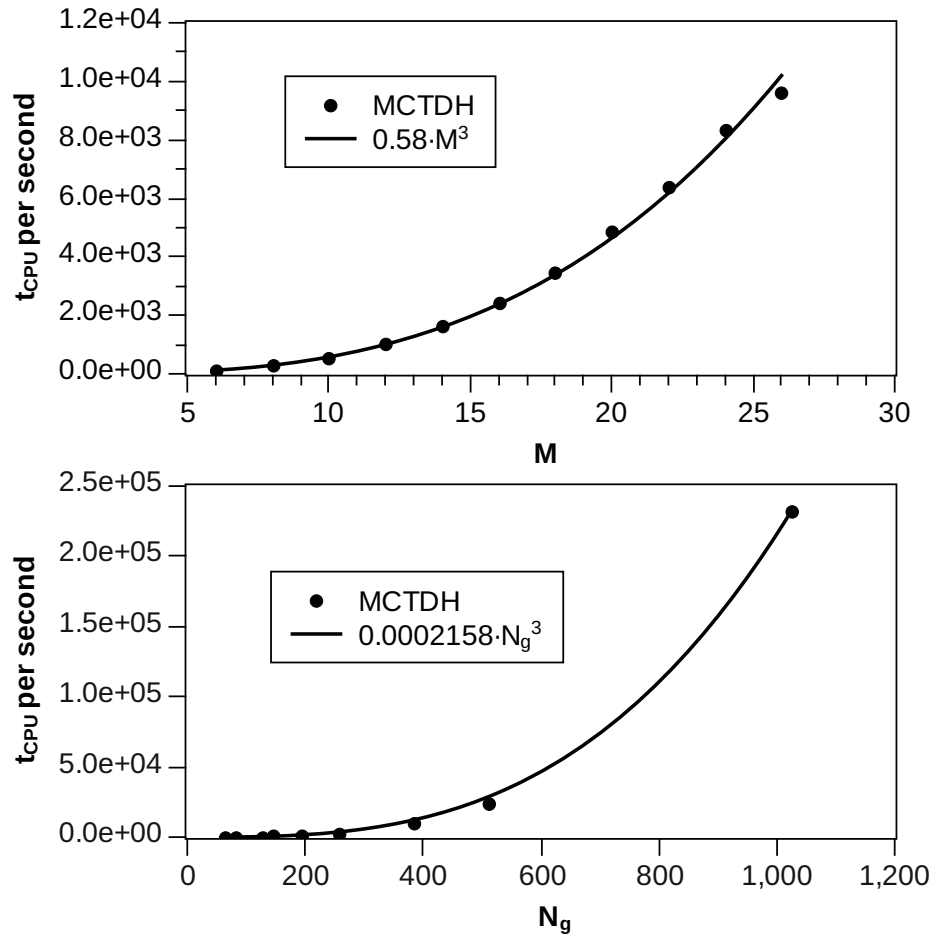


Figure 4.1: Top panel: This plot shows the total CPU time as a function of the number of single-particle functions M for $N_g = 256$, $g = 5.093$ and $\sigma = 0.05$. For the system under investigation a cubic dependence is found which highly limits the choice of M .

Bottom Panel: This plot shows the total CPU time t_{CPU} as a function of the number of grid points N_g for $M = 18$, $g = 5.093$ and $\sigma = 0.05$. For the system under investigation a cubic dependence is found which highly limits the number of grid points that can be used.

CHAPTER 4. MCTDH - SIMPLE IMPROVEMENTS DUE TO RESCALING OF THE INTERACTION

function δ_σ converges to $\delta(x)$. This approximation imposes inaccuracies. To obtain a reasonable approximation δ_σ has to be short-ranged compared to the system's spatial extension but also larger than the grid spacing $\Delta_{grid} = 1/N_g$ to be smoothly represented. The latter is necessary to avoid convergence problems arising from the specific numerical implementation of the MCTDH equations in the Heidelberg MCTDH program package. N_g is the number of grid points in the discrete variable representation (DVR) [144] as implemented in the Heidelberg MCTDH package. The mean inter-particle distance $1/n$, where n is the average density of particles, further restricts the choice of σ . However, it can be safely assumed that $\delta_\sigma(x)$ properly emulates $\delta(x)$ if σ is chosen to be smaller than the 1D scattering length. However, this constraint is not as important as the other two. Mathematically the constraints can be summarised as [90]

$$\begin{aligned}\sigma &\ll 1/n \\ \sigma &\gtrsim \Delta_g = 1/N_g \\ (\sigma &\ll 2/|g|)\end{aligned}\tag{4.2}$$

Hence, we have performed several convergence studies for three bosons in a one-dimensional ring to ensure the validity of our simulations.

For all the simulations in this section we used the plane wave fast Fourier transform (FFT) DVR which is equivalent to a spatial grid representation with equidistant grid points. We also performed an *improved relaxation* scheme to the ground-state solution via the implemented Davidson integrator (DAV) (see Ref. [89, 90] and App. B.3.3). We note, that other integration methods exist that are implemented into the Heidelberg MCTDH package, such as RDAV and RRDAV. They can be applied to real Hamiltonians only, but allow for a much larger number of single-particle function. However, for the real-time time-dependent simulations of the problems presented in this section the nonlinear terms in the equations of motion create a hermitian Hamiltonian. Therefore, we used the complex DAV integrator for the convergence studies to be able to generalise our results to the time-dependent case. For the propagation of the single-particle functions the built-in 8th order Runge-Kutta method has been used (see appendix B.1). The error estimate for the MCTDH propagators are chosen to be considerably small

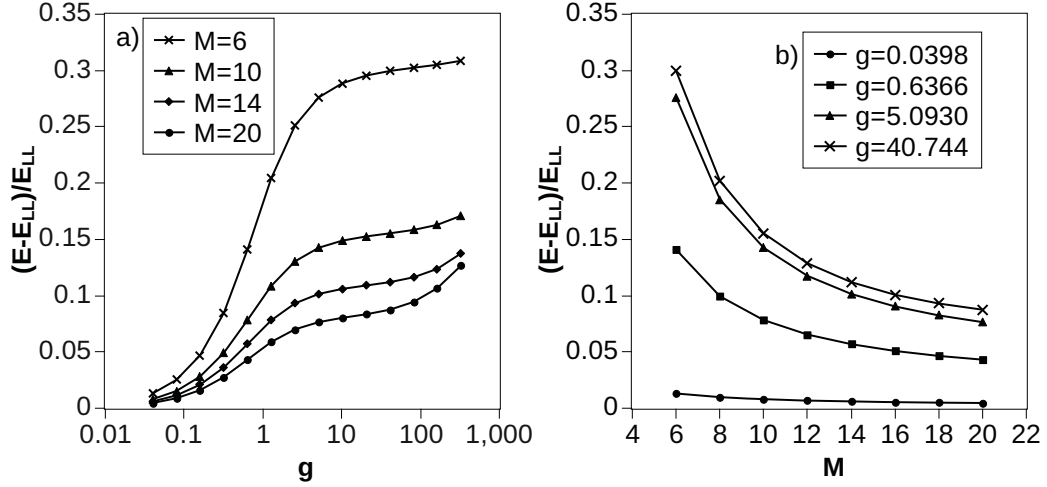


Figure 4.2: Relative energy difference $(E - E_{LL})/E_{LL}$ shown for a range of g for $N_g = 256$ and $\sigma = 0.05$. Clearly, for large values of M the accuracy of the simulations improves. At increasing values of g it is expected that the curves converge. Instead, the left graph shows an enhanced increase of the energy difference for $g \gtrsim 100$. This can be explained by the stronger effect of the finite width of the Gaussian function which was used to model a contact potential. For large g this interaction potential is no longer a good approximation of a delta function and the particles see a smoothly but already strongly increasing potential at non-zero interparticle distances which leads to higher energies. Furthermore, the right graph demonstrates that the convergence is very slow with respect to M .

($\sim 10^{-9}$).

4.1.1 Discussion on CPU times

The total CPU time until convergence of the simulations is reached is highly dependent on several factors: The number of single-particle functions M , the number of grid points N_g for the DVR basis and the number of particles. Here, convergence of the ground-state calculations is reached when the change in total energy is less than 10^{-7} . We already mentioned how the Hilbert space scales as a function of the number of particles. In this section we only focus on M and N_g , while we will briefly discuss the dependence on N in chapter 5. Increasing the number of single-particle functions increases not only the total number of grid points for the

CHAPTER 4. MCTDH - SIMPLE IMPROVEMENTS DUE TO RESCALING OF THE INTERACTION

whole system, $N_g \cdot M$, but also the size of the Hilbert space, M^N . The results in the top panel of Fig. 4.1 confirm that for $N_g = 256$ and $N = 3$, the total CPU time t_{CPU} mainly depends on the size of the Hilbert space $\propto M^3$. However, simulations for $M = 25$ already take 70 times longer until converged than $M = 6$ and almost five times longer than $M = 15$. Another aspect not mentioned yet is that a larger Hilbert space also demands more computer memory. The maximum amount available in today's computer generation is finite and in addition its bandwidth is limited as well. Taking all this into account we are clearly limited with our choice of M .

A larger number of grid points is needed to improve the interaction potential in Eq. (4.2) to accurately approximate a contact δ -potential. From the bottom panel in Fig. 4.1 we find that t_{CPU} for varying N_g shows an unfavourable scaling of $t_{CPU} \sim N_g^3$.

4.1.2 Convergence with respect to the number of single-particle functions

Fig. 4.2 gives an overview of the relative energy difference $(E - E_{LL})/E_{LL}$ for different M . E_{LL} is the exact many-body ground-state energy from the Lieb-Liniger theory in Sec. 2.4.2a. Clearly, for large values of g , when the system enters the TG regime and starts to fermionise, the errors become very large, up to 30% for $M = 6$. The shapes of the curves, however, seem to be independent of M , increasing from almost zero for small nonlinearities until they reach a plateau for larger values of g . We also find an additional increase for extremely large g . This behaviour has two main sources: First of all the finite width of the Gaussian interaction potential becomes important and numerical convergence of the calculations is not guaranteed anymore. Therefore, the results might become unphysical in this regime. For Fig. 4.2b we studied the convergence of $(E - E_{LL})/E_{LL}$ with regards to M for different interaction strengths. It is obvious from the graph that the MCTDH results converge towards the exact Lieb-Liniger results. Secondly, the convergence is very slow for increasing M . This makes it particularly hard to study properties that rely on high accuracy. In Sec. 4.2 we discuss the problem of finite M , i.e. finite Hilbert space, and propose a solution

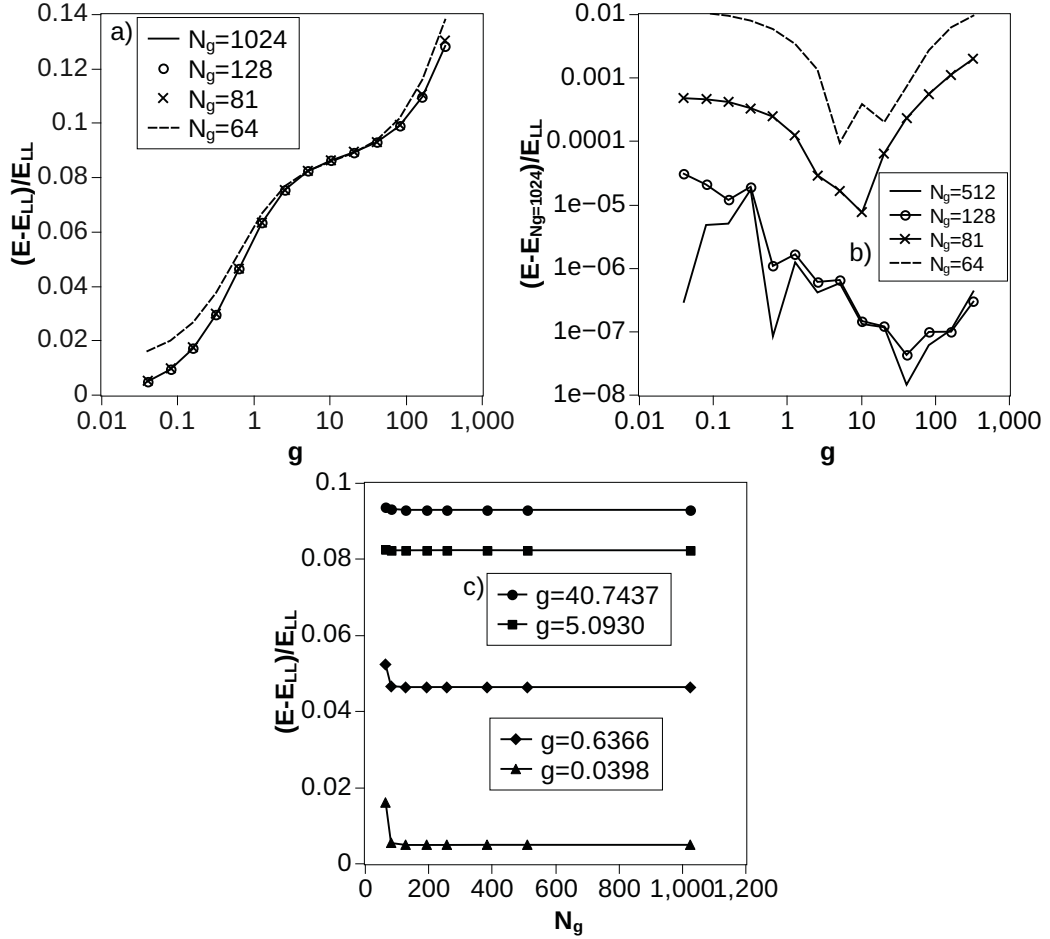


Figure 4.3: Relative energy difference $(E - E_{LL})/E_{LL}$ vs g (a), M (b) and N_g (c) for $M = 18$ and $\sigma = 0.05$. As expected, the energy difference shown in a) becomes larger for increasing interaction as a larger Hilbert space is needed to describe the many-body state. The differences between the energies for different N_g are small and only for $N_g = 64$ the curve is clearly distinguishable from the others. Plot b) shows a the differences between the energies compared to the ground-state energy for $N_g = 1024$ on a logarithmic scale. It is remarkable that for a grid with $N_g = 128$ the energy difference to the $N_g = 1024$ case is of the order of $\mathcal{O}(10^{-7})$. This is comparable to the overall accuracy in our calculations. Furthermore, plot b) again demonstrates that a small number of grid points is sufficient for accurate results as the graphs flatten out very quickly.

by rescaling the interaction.

4.1.3 Convergence with respect to the number of grid points

For the simple problem of three bosons in a ring, presented in this section, we find a small value of N_g to be sufficient (see Fig. 4.3). In Fig. 4.3 the relative energy difference does not change significantly for a large range of g . Only for very small grid point numbers, i.e. $N_g = 64$, the results become much worse compared to smaller grid spacings. However, the difference is only 1 – 2%, and therefore $N_g = 64$ can be considered to be large enough to give accurate results. In Fig. 4.3, however, the differences become more distinct. The graph shows that an increase from $N_g = 64$ to $N_g = 81$ gives one order of magnitude higher accuracy. We chose $N_g = 256$ for the calculations in this section because more grid points do not give a considerable improvement and the time t_{CPU} for the numerical calculations is still feasible. Overall, the effect of the grid spacing on the results is negligible compared to the restrictions given by truncation of the Hilbert space. Fig. 4.3 supports the previous finding, showing that the relative energy only weakly depends on $N_g > 64$.

4.1.4 Convergence with respect to the width of the interaction potential

We studied how the results are related to the finite width σ of the Gaussian function in Eq. (4.1). In Fig. 4.4 the convergence of the relative energy for different σ has carefully been investigated. It is obvious from the graphs that large interactions worsen the results dramatically for large values of σ . However, we find that a value of $\sigma = 0.05$ already gives accurate results, differing only by $\sim 1\%$ compared to $\sigma = 0.025$ for interactions strengths up to $g = 40$. We find that for these values of σ , the major source for the energy difference with respect to the exact energy originates from the truncation of the Hilbert space. Smaller values of σ would demand a smaller grid spacing and, hence, a larger number of grid points. This is, however, numerically not feasible for simulations on large time scales.

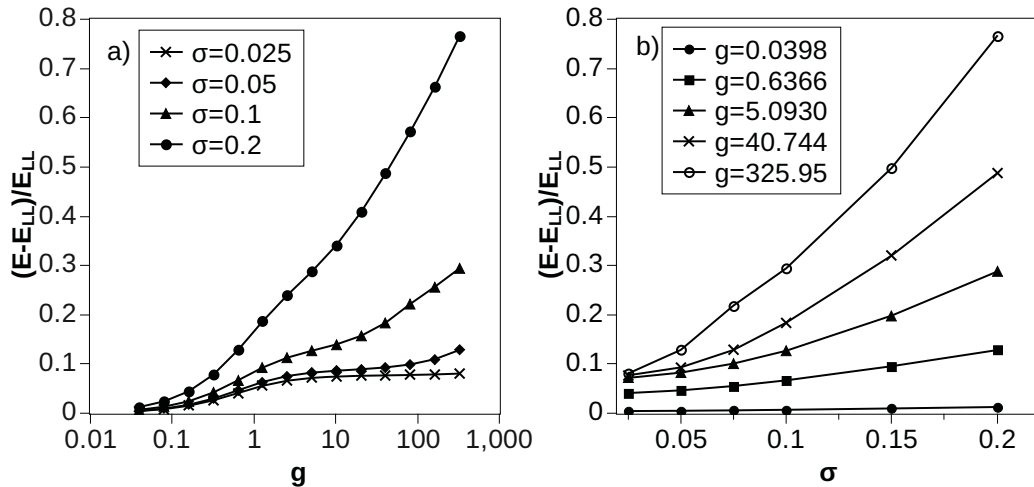


Figure 4.4: Relative energy difference $(E - E_{LL})/E_{LL}$ as a function of g (a) and σ (b) for $M = 18$ and $N_g = 256$. Smaller values of σ guarantee smaller energy differences. Also, the for large interactions and to large σ the energy differences become larger. However, results for $\sigma = 0.025$ and $\sigma = 0.05$ are near very close up to $g = 40$.

4.1.5 Conclusion

It has been shown that several factors have to be considered restrict the errors in our numerical simulations to a minimum. A reduced Hilbert space, i.e. finite value of M , is the major contribution to the errors. The dependence on the number of grid points and the width of the Gaussian function, used to approximate a contact potential, are negligible for the problems in this section. However, the next section introduces a simple and efficient method to reduce the errors by rescaling of the interaction.

4.2 Rescaling of the interaction

4.2.1 Theoretical background

The purpose of the work presented in this chapter is to improve the approximations for a given, finite, basis-set expansion (see Sec. 2.6.1) and to find improvements

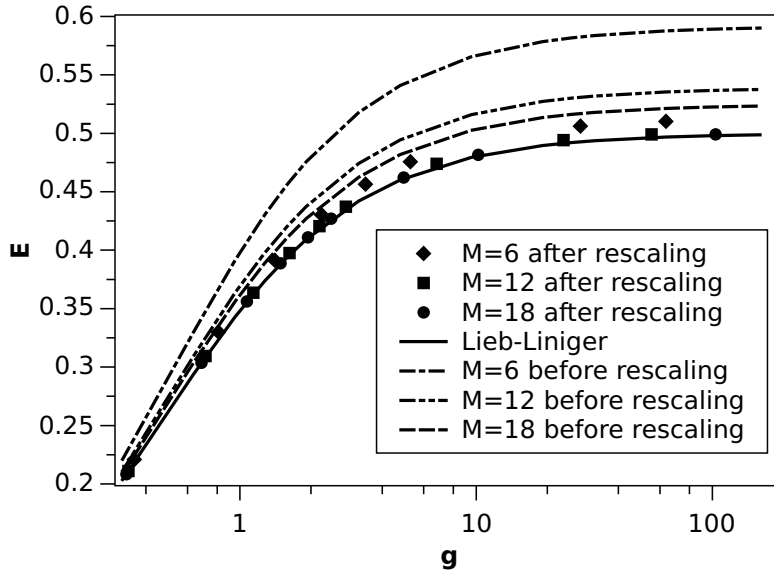


Figure 4.5: Ground-state energies for two interacting bosons in a periodic box before (lines) and after (symbols) rescaling according to Eqs. (4.9) and (4.13) compared with the exact (Lieb-Liniger) energy (solid line). The calculated energies have been obtained via exact diagonalisation of the truncated Hamiltonian matrix with different numbers of modes M . Clearly, rescaling of the interaction reduces the errors in the energies significantly.

on the slow convergence of our simulation as shown in the inset of Fig. 4.6. While previous works have explored elaborate procedures to approximate an effective finite Hamiltonian with the exact eigenvalues E_ν [136–139], we show that it is possible to obtain significant improvements by simply rescaling the interaction parameter g .

4.2.1.1 Two particles on a ring

For two particles without external potential an analytic expression for the rescaled interaction constant \tilde{g} can be found that reproduces the correct ground-state energy and the Fourier components of the wave function up to a cutoff. The rescaling procedure is thus exact for this case. Consider $N = 2$ bosons in a one-dimensional box with length L and periodic boundary conditions. We again use dimensionless

4.2. RESCALING OF THE INTERACTION

equations by setting $x = z/L$, $E = \epsilon/E_0$ and $g = g_{1D}/E_0L$ for the first excited single-particle energy $E_0 = 2\pi^2\hbar^2/(mL^2)$. This model might be realised with ultracold atoms in a tightly focussed ring trap. The Hamiltonian (2.37) simplifies to

$$H_{2p} = -\frac{1}{2} \left(\frac{\partial^2}{\partial x_1^2} + \frac{\partial^2}{\partial x_2^2} \right) + g\delta(x_1 - x_2) \quad (4.3)$$

where x_i is the spatial coordinate of atom i and g the physical interaction strength. A finite basis-set expansion for this system is

$$\psi(x_1, x_2) = \sum_{k_1, k_2 = -(M-1)/2}^{(M-1)/2} C_{k_1, k_2} e^{i2\pi k_1 x_1} e^{i2\pi k_2 x_2}. \quad (4.4)$$

For simplicity, we assume here an odd number of momentum modes M in the expansion. First consider the case for the full Hilbert space with $M = \infty$. To find the ground-state we substitute Eq. (4.4) and Eq. (4.3) into the Schrödinger equation $(E - H_{2p})\psi = 0$. Projecting to zero momentum solutions $k_1 + k_2 = 0$ and by multiplying with $\exp[-i2\pi k(x_1 - x_2)]$ and integrating over the particle coordinates we obtain

$$(E - 2k^2)C_{k, -k} = g \sum_{q=-\infty}^{\infty} C_{q, -q}. \quad (4.5)$$

The right hand side of Eq. (4.5) is independent of k . Therefore we find $C_{-q, q} \propto (E - 2q^2)^{-1}$ and

$$\frac{1}{g} = \sum_{q=-\infty}^{\infty} \frac{1}{(E - 2q^2)}, \quad (4.6)$$

which relates the exact energy E to the physical interaction strength g . Employing the finite basis-set expansion limits the sum over q to only M terms and thus yields a different, approximate, value \bar{E} for the energy. Here, we choose a different path

CHAPTER 4. MCTDH - SIMPLE IMPROVEMENTS DUE TO RESCALING OF THE INTERACTION

and introduce the rescaled interaction strength \tilde{g} by

$$\frac{1}{\tilde{g}} = \sum_{q=-(M-1)/2}^{(M-1)/2} \frac{1}{(E - 2q^2)}, \quad (4.7)$$

$$= \frac{1}{g} + \frac{1}{g_0}, \quad (4.8)$$

where the last equation defines the constant g_0 . While Eq. (4.7) guarantees that \tilde{g} yields the exact energy E , it is Eq. (4.8) that provides the rescaled interaction constant \tilde{g} as a function of g :

$$\tilde{g} = \frac{g}{1 + g/g_0}. \quad (4.9)$$

Therefore, solving the Schrödinger equation with this rescaled value \tilde{g} instead of g in the Hamiltonian (4.3) in the finite basis-set expansion gives the exact energy E for the physical interaction strength g . Also the finite number of expansion coefficients $C_{k,-k}$ is identical to the full Hilbert space expansion and, according to Eq. (4.5), is given by

$$C_{k,-k} = \frac{A}{E - 2k^2}, \quad (4.10)$$

where

$$A = g \sum_{q=-\infty}^{\infty} C_{q,-q} = g \sum_{q=-(M-1)/2}^{(M-1)/2} C_{q,-q}. \quad (4.11)$$

The value of g_0 is found by expanding the sums in powers of $1/M$ from

$$\frac{1}{g_0} = \frac{2}{M} + \frac{2E - 1}{2M^3} + O(M^{-5}). \quad (4.12)$$

For a large number of modes and sufficiently low energy E (with the approximate condition $M^2 \gg E/2$) we thus find to leading order that g_0 is independent of the energy and given by

$$g_0 \approx \frac{1}{2}M. \quad (4.13)$$

Figure 4.5 shows how the rescaling in the approximation (4.13) significantly improves the ground-state energy. For $M = 6$ the energy after rescaling is only 3% off the exact energy whereas before rescaling the difference was $\sim 20\%$, i.e. ~ 7

times larger.

The constant g_0 is readily interpreted from Eq. (4.9) as the value of the rescaled interaction \tilde{g} where the physical interaction g reaches infinity. Physically, this is the TG limit where the contact interactions are arbitrarily strong and the system is strongly correlated. Our results thus indicate that a finite basis-set expansion with a finite value of the rescaled interaction constant $\tilde{g} = g_0$ can produce exact results for infinite value of the physical interaction strength! Since the energies and wave functions in the TG limit can also be calculated by the Bose-Fermi mapping [36], this limit is an important reference point.

4.2.1.2 Empirical rescaling

The analytical results of the preceding section motivate us to extend the idea of rescaling to more than two particles and to problems with arbitrary external potential, which, generally, cannot be solved analytically. We propose to replace the Hamiltonian (2.37) by the rescaled version

$$\tilde{H}_{mb} = \sum_{i=1}^N h_i(x_i) + \sum_{i<j} \tilde{g} \delta(x_i - x_j), \quad (4.14)$$

where we have only changed the value of the interaction strength from the physical value g . Within a finite basis-set expansion we obtain a matrix with elements \tilde{H}_{IJ} , which is to be used for numerical simulation. The smallest eigenvalue is the approximate ground-state energy $\bar{E}_G(\tilde{g})$. For the rescaled interaction \tilde{g} we continue to use Eq. (4.9) and determine the value of g_0 by requiring that the approximate ground-state energy at g_0 equals the exact energy of the TG limit

$$\bar{E}_G(g_0) = E_{\text{TG}}. \quad (4.15)$$

A finite solution for g_0 can always be found since the approximate value of $\bar{E}_G(g)$ overestimates the real value and $\bar{E}_G(\tilde{g})$ is a monotonously growing function of \tilde{g} with $\bar{E}_G(0) \leq E_{\text{TG}}$. The value of E_{TG} is equal to the ground-state energy of a system of non-interacting fermions due to the Bose-Fermi mapping theorem [36]. It is given by the sum of single-particle energies, which can be determined analytically

CHAPTER 4. MCTDH - SIMPLE IMPROVEMENTS DUE TO RESCALING OF THE INTERACTION

or numerically to very high precision.

This rescaling procedure is very simple to implement, since only knowledge of the value of the single constant g_0 is needed. We assume here for simplicity that g_0 is independent of the energy of the wave function and can be used for any set of (low-lying) excited states as well as time-dependent processes involving such states. As an approximation, this is consistent with the analytic findings for two particles from the previous section.

Rescaling improves numerical calculations by either increased accuracy or decreased computational effort for a given desired accuracy (CPU time $\sim M^3$ for our five particle simulations). For $\tilde{g} > g_0$ we find unphysical results. Therefore, CPU times are further reduced as only results for $\tilde{g} \leq g_0$ are used in the rescaling. Further studies on CPU times were already presented in the previous section 4.1.

Before detailing our numerical results and benchmarking, we introduce the MCTDH method suitable for general trapping potentials.

4.2.1.3 Connection to T matrix renormalisation

The rescaling approach introduced in Sec. 4.2 is closely connected to the well-known renormalisation of the scattering T matrix (for a readable account see Ref. [32]). In this approach, the coupling constant of an effective many-body theory is renormalised to produce the correct T matrix for the two-body scattering problem, which is known exactly. Indeed, Eq. (4.9) for the rescaled interaction strength together with Eq. (4.13) for the value of g_0 are identical to the result of Ref. [32] for the renormalised T matrix of a high-momentum cutoff introduced there due to discretisation of space (identifying the computational volume of momentum space $2\pi M/L$ with the Brillouin zone of Ref. [32]). This result was rigorously derived for weak interactions and high cutoffs. In Sec. 4.2.1.1 we have extended the approach to the strongly interacting regime for two particles where now the rescaled interaction constant in principle becomes energy dependent. The extension to non-perturbative, strongly interacting multi-particle systems in Sec. 4.2 with Eq. (4.6) for the value of g_0 is heuristic in nature. The purpose of the numerical studies reported in the following section is to establish the usefulness and to quantify the accuracy of the this approach.

4.2.1.4 MCTDH

For the simulation presented in this chapter we used the Heidelberg MCTDH program package [88–91] if not stated otherwise. Eigenenergies and eigenstates can be obtained by the relaxation method [145], i. e., by propagation in negative imaginary time. Here we use a modification, *improved relaxation* [146] (see App. B.3.3), which can also be used in block form [147] to simultaneously compute a set of eigenvectors.

In practice, the single-particle wave functions in the MCTDH method are represented on a large number of primitive basis functions, the choice of which depends on the spatial geometry (typically 128 and 162 grid points in the harmonic oscillator discrete variable representation for the harmonic and the double-well potentials respectively and 155 points in the exponential discrete variable representation as per Ref. [89]). The set-up of MCTDH for ultracold atom calculations follows Ref. [134]. In particular, the contact potential is replaced by a narrow Gaussian for practical purposes. In Sec. 4.1, we have carefully studied the dependence of our calculations on the parameters of the primitive basis and the Gaussian interaction to make sure that the results presented here are converged and the influence of these further approximations is negligible.

4.2.2 Bosons in a ring

We first benchmark the rescaling method of Sec. 4.2.1.2 for the Lieb-Liniger model [38] of bosons in a box with periodic boundary conditions, where exact eigenstate energies are easily available for any values of the interaction strength and particle number. Fig. 4.6 shows the relative deviation from the exact ground-state energy obtained from MCTDH calculations before and after rescaling. Rescaling is seen to significantly reduce the error. The rescaled results reproduce the exact energy in the TG limit by construction but the improved accuracy for finite interaction strength is non-trivial. As expected, both the raw and rescaled data improve with increasing M . The maximal errors for, e.g., $M = 13$ can be reduced from $\sim 23\%$ down to $\sim 0.6\%$, i.e. a factor of 40. This is a significant improvement.

In order to test how well the wave function is approximated in the TG limit

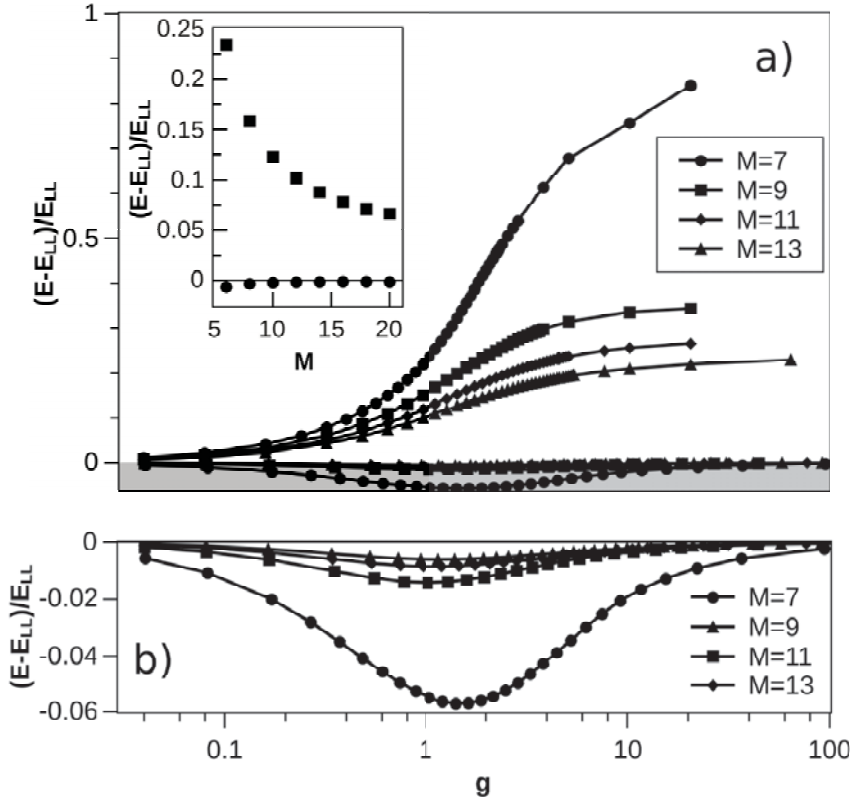


Figure 4.6: Relative deviation of the approximate ground-state energy from the exact Lieb-Liniger (LL) result [38] before rescaling (white area of panel a) and after rescaling (gray area of panel a and panel b) for five particles in a box of length L with periodic boundary conditions. Rescaling reduces the maximum errors from 23% to 0.6% ($M = 13$). The inset shows the relative energy deviation versus the number of modes M for three particles at $g = 1.9099$. Results for the truncated Hamiltonian without rescaling (squares) converge very slowly while rescaling (circles) significantly reduces the errors already for small M .

4.2. RESCALING OF THE INTERACTION

we investigate the reduced pair density

$$\rho_2^{(g)}(0, x) = \int \cdots \int dx_3 \dots dx_N |\Psi^{(g)}(0, x, x_3, \dots, x_N, t)|^2. \quad (4.16)$$

The results of MCTDH calculations are shown in Fig. 4.7 for different values of the interaction g along with the exact solution in the TG limit $\rho_2^{TG}(0, x) = [(2 + \cos x) \sin^2 \frac{x}{2}] / 3\pi^2$ [36]. Agreement between the finite basis-set expansion at the value of $g_0 = 5.3958E_0L$ and the exact solution is reasonable. The discrepancies can well be explained by the absence of short-wavelength modes in the finite expansion. Most importantly, the agreement between the approximate and exact functions clearly worsens for interaction strengths larger than g_0 , where the structure in the finite basis-set calculation overshoots.

In order to quantify the quality of the approximation, we define the overlap with the exact solution at the TG regime by

$$\begin{aligned} F^{(g)}(\rho_2^{(g)}, \rho_2^{TG}) \\ = \frac{\int \rho_2^{TG}(0, x) \rho_2^{(g)}(0, x) dx}{\sqrt{\int \rho_2^{(g)}(0, x) \rho_2^{(g)}(0, x) dx} \sqrt{\int \rho_2^{TG}(0, x) \rho_2^{TG}(0, x) dx}}, \end{aligned} \quad (4.17)$$

which is shown in the inset of Fig. 4.7. We find that the maximum of $F^{(g)}$ is reached near g_0 , which justifies the choice of g_0 through Eq. (4.15).

In order to study the scaling with particle number, we have performed exact diagonalisation calculations for $N = 2 \dots 6$ particles in a ring of length $L = N/\tilde{n}$, where the particle density \tilde{n} was fixed to the same value as in Fig. 4.7. Fig. 4.8 shows the maximal relative deviation of the rescaled energy as a function of particle number. A fitting of the numerical results shows that retaining $M = 2N - 1$ single-particle functions gives a maximal relative error bounded by $|E/E_{LL} - 1| \lesssim 1.5\%$ for any value of $g > 0$. Although for clarity only odd numbers of single-particle modes M are shown in Fig. 4.8, we have verified that these findings also hold for even M .

If we assume that the scaling $M = 2N - 1$ is sufficient to maintain accuracy uniformly over the whole range of interaction strengths also for larger particle numbers, we still find that the numerical effort of MCTDH or exact diagonalisation

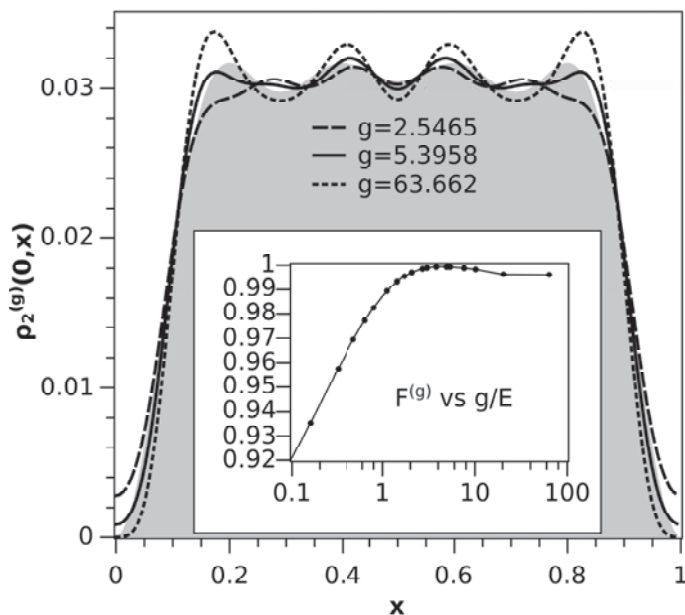


Figure 4.7: Density-density correlation function for five particles and $M = 13$ single-particle functions in a periodic box. This plot compares the reduced two-particle density $\rho_2^{(g)}$ of Eq. (4.16) for different interaction strengths from MCTDH calculations without rescaling with the exact TG expression (the area below this curve is shaded). We find a good agreement with the exact solution close to $g_0 = 5.3958$. This is shown in the inset, where the overlap $F^{(g)}(\rho_2^{(g)}, \rho_2^{TG})$ of Eq. (4.17) is plotted as a function of the interaction g . There, the maximum occurs close to g_0 .

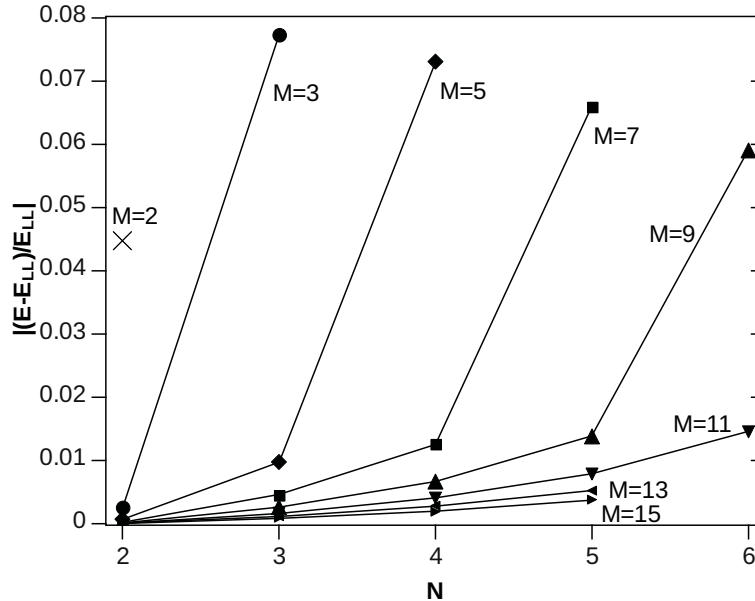


Figure 4.8: Maximal relative deviation of the energy after rescaling from the exact result E_{LL} over the range of interaction strengths $0 < g < \infty$. The particle number and box length L are varied while the density is kept fixed.

studies grows exponentially with N . This limits studies of this sort to fewer than 10 particles with current-day computers. We note that the scaling $M = 2N - 1$ was obtained empirically and verified in our simulations. However, it is only valid for the type of system described in this section. Different geometries and system parameters might lead to different scalings.

4.2.3 Bosons in a harmonic potential

In order to test the rescaling method in the presence of an external potential we consider a harmonic trapping potential

$$V_{\text{ext}}(x) = \frac{1}{2}x^2. \quad (4.18)$$

For this and the following section we solve the dimensionless equations according to the natural energy and length scales defined by the harmonic oscillator

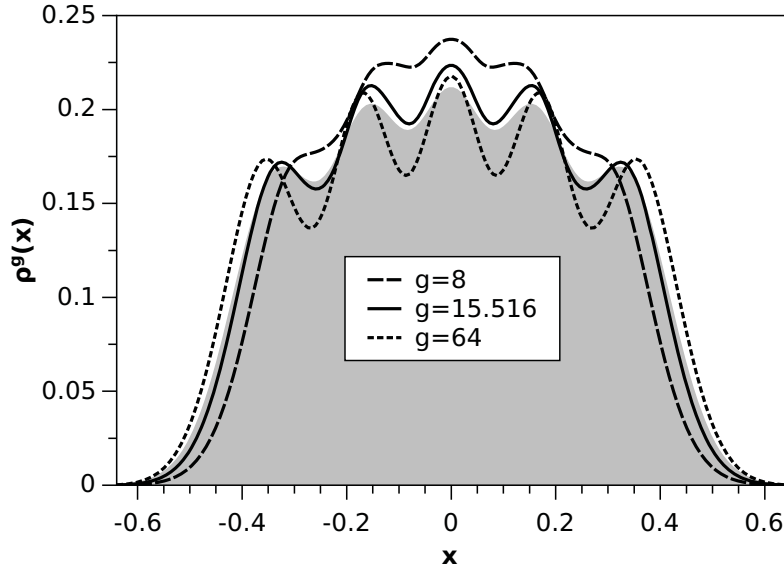


Figure 4.9: Density of five particles in a harmonic potential for different interaction strengths without rescaling and $M = 13$. Analogous to Fig. 4.7, the best agreement with the exact TG result, which is given by the shaded area, can be found at $g = g_0$, where $g_0 = 15.516$.

level spacing $E_{0,H} = \hbar\omega$ and $L_H = \sqrt{\frac{\hbar}{m\omega}}$, respectively, where ω is the harmonic oscillator frequency.

Figure 4.9 compares the single-particle density of the TG wave function with MCTDH simulations for five particles at different values of the interaction strength without rescaling. The agreement between the exact and the finite basis-set results at the value of the interaction strength $g_0 = 15.516\dots$ is much better than for larger values of g . This result is analogous to the ring case and supports our proposition that g_0 from Eq. (4.15) provides a good approximation for the wave function.

Full analytical solutions are available for two particles in a harmonic potential. The exact energies for the ground and excited states are found from the implicit equation [148]

$$g = 2\sqrt{2} \frac{\Gamma(-\frac{E}{2} + \frac{3}{4})}{\Gamma(-\frac{E}{2} + \frac{1}{4})}. \quad (4.19)$$

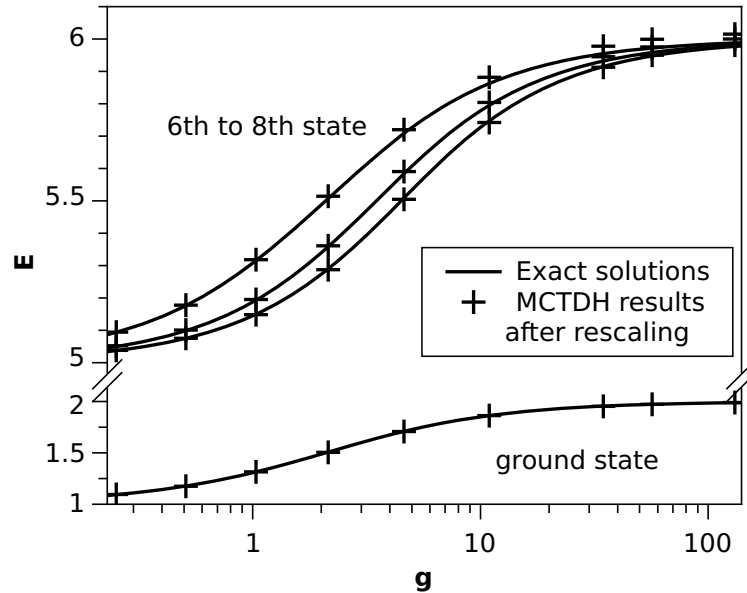


Figure 4.10: Energies of the ground state and the 6th to 8th excited states with $M = 15$ of two bosons in a harmonic well after rescaling compared to the exact results from Eq. (4.19). The results clearly show the high accuracy of the rescaled results. The largest error occurs for the 7th excited state where it is decreased from $\sim 2\%$ before rescaling (not shown on this graph) to $\sim 0.3\%$ after rescaling.

where Γ is the gamma function. Figure 4.10 compares the ground-state and a few excited-state energies with rescaled MCTDH results. The highest few states and the ground state have been chosen as they are more likely to show the largest errors within the block-diagonalisation scheme (see below). We emphasise that a single value of $g_0 = 29.75$ obtained from Eq. (4.15) was used for rescaling. The procedure not only maintains the correct order of excited states but also quantitatively describes the excited-state energies remarkably well.

4.2.4 Bosons in a double well

The rescaling method is further tested for the description of excited states of the TG gas in a double-well potential. Exact solutions are not available for interacting multi-particle systems in the double well except for the TG gas, where their

CHAPTER 4. MCTDH - SIMPLE IMPROVEMENTS DUE TO RESCALING OF THE INTERACTION

exact energies are simply found from sums of single-particle energies (which can be determined with great accuracy) due to the Bose-Fermi mapping of Ref. [36].

We consider the double-well potential

$$V_{\text{ext}}(x) = \frac{1}{2}(x)^2 + he^{-\frac{2}{3}(x)^2} \quad (4.20)$$

with varying barrier height h at the centre. Figure 4.11 shows the energies for the ground and excited states from rescaled MCTDH calculations and analytical results. All MCTDH results were obtained in the TG regime at $\tilde{g} = g_0$. The value of g_0 has been determined for each value of h from a dedicated ground-state calculation.

The results reported in Fig. 4.11 were calculated using the block-improved-relaxation method [147] to efficiently determine several states simultaneously. Since an identical set of single-particle functions is used for the finite basis-set expansion for all states, the result is not as well variationally optimised for each individual state as the single-state calculation that was used to determine g_0 . This explains the discrepancy of the numerical and exact ground-state energies seen in Fig. 4.11, which also provides a convenient order-of-magnitude estimate for the error of the block-improved-relaxation scheme. A shift to high energies for the whole set of numerical values compared to the exact ones of the same approximate magnitude is clearly observed in the data.

In addition, the second and third excited states in Fig. 4.11 should be degenerate at $h = 0$, which is not reproduced by the rescaled MCTDH results. By the Bose-Fermi mapping, these two states are identified as configurations $(1, 1, 1, 1, 0, 0, 1, 0, \dots)$ and $(1, 1, 1, 0, 1, 1, 0, 0, \dots)$ in the occupation number basis of fermions in the harmonic oscillator ($h = 0$) potential. The two states involve different modes in the fermionic description and thus have different sensitivity to the finite set of available single-particle functions in the block-improved-relaxation method. This is a problem that the proposed rescaling method cannot fix.

The problem vanishes when more single-particle functions are used, but this is costly. Single-state simulations indeed show that the energy difference approaches zero for an increasing number of single-particle functions. These problems do not affect the validity of rescaling which is shown to work adequately and to

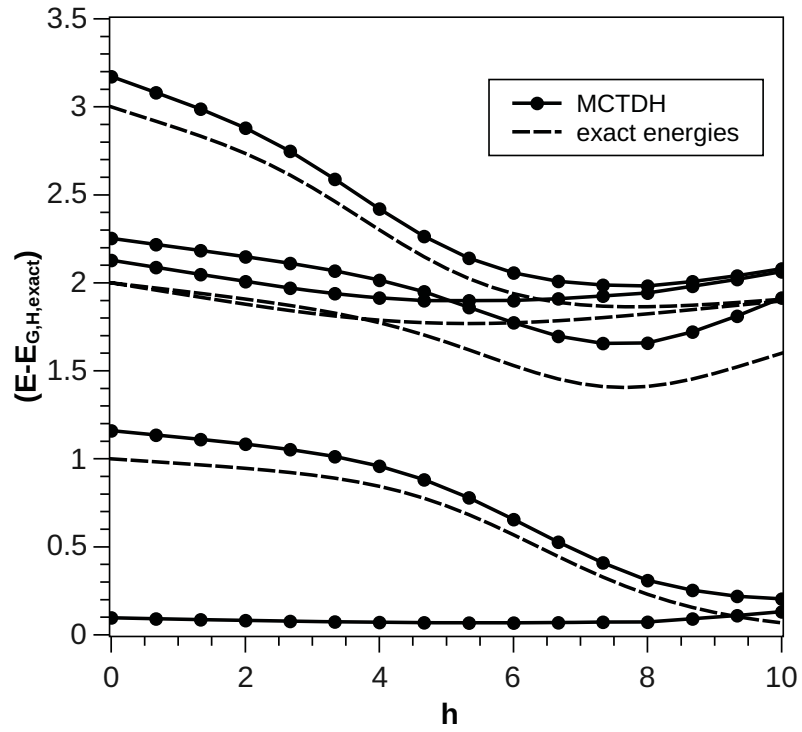


Figure 4.11: Excited states of the Tonks-Girardeau (TG) gas in a double-well trap. Shown are the energies of the ground state and the first four excited states minus the exact TG ground-state energy for five bosons in a double-well potential vs barrier height h . The graph compares rescaled MCTDH calculations with $M = 13$ single-particle functions (solid line with bullets) and exact TG energies (dashed line).

CHAPTER 4. MCTDH - SIMPLE IMPROVEMENTS DUE TO RESCALING OF THE INTERACTION

be independent of the shape of the external potential. The energy differences compared to the analytical results range around about 1%.

For $h = 10$ a near degeneracy between the third and fourth state emerges. In contrast to the previously discussed degeneracy at vanishing barrier, it is very well described by the simulation. For large enough barrier height the double well resembles two separated anharmonic wells. According to the Bose-Fermi mapping, we identify the degenerate states by the superpositions of $(1, 1, 1, 0, \dots)$; $(1, 0, 1, 0, \dots)$ and $(1, 0, 1, 0, \dots)$; $(1, 1, 1, 0, \dots)$, showing the fermionic configurations in the left and right-hand well, respectively. Since these two states involve similar fermionic modes, their degeneracy is well described by the truncated basis-set expansion with a limited number of single-particle functions.

Overall, we find good description of the excited states by the rescaled simulation in the double well for a large variation of barrier height h from a harmonic trap ($h = 0$) to almost completely separated wells.

4.3 Summary

In the first section of this chapter we presented convergence studies on possible numerical errors due to the discretisation of the spatial coordinate, the approximated contact interaction and the finite Hilbert space. We showed that the major contributions to deviations from exact results are related to the finiteness of the single-particle basis in the MCTDH approach.

In Sec. 4.2 we proposed a simple rescaling procedure to overcome this problem. It is suitable for many-body calculations with a contact interaction in 1D in a truncated Hilbert space based on Eqs. (4.9) and (4.15). The method requires knowledge of only a single parameter. This was found from the interaction strength where the numerical ground-state energy matches the TG energy, which can easily be found from single-particle calculations. For two particles in a ring geometry the rescaling exactly reproduces the correct energies and expansion coefficients of the wave functions. Empirical evidence suggests that the scheme can be extended to multiple particles, external trapping potentials, and low-lying excited states. In this chapter we tested the method against exact results for ring geometries and harmonic and double-well potentials and it was proved to significant improve the

accuracy of our calculations.

We also found that rescaling works for excited-state calculations and for arbitrary potentials. Therefore, it is expected to significantly improve time-dependent simulations as well, as long as the state of the system is well described by the low-lying part of the energy spectrum.

The rescaling method was already applied to the published work presented in App. A. There it was shown to be helpful in finding a method to create robust superposition states with bosons in a ring confinement.

CHAPTER 4. MCTDH - SIMPLE IMPROVEMENTS DUE TO RESCALING OF THE INTERACTION

*In physics, to be in two places
at the same time would be a
miracle;
in politics it seems not merely
normal, but natural.*

Charles Edison

5

Full quantum dynamics of soliton scattering

In this chapter we investigate the scattering of a soliton on a rectangular well in a full quantum many-body approach, i.e. by solving the MCTDHB equations (2.44). This extends previous mean-field Gross-Pitaevskii (GP) calculations reported in chapter 3. For this, we developed a program package designed to solve the MCTDHB equations, which we called QiwiB. QiwiB can be applied to one-dimensional systems for bosons interacting via a contact potential. It is an open source project and is freely available for download from [96]. Conceptual and numerical details can be found in App. D, and a numerical study on CPU times for different sizes of the Hilbert space is available in App. C.

Compared to the GP results from chapter 3, the many-body QiwiB calculations reveal new features around the transition regions, that is from the full reflection to the full transmission regime and from full transmission to full trapping. For the calculations in Sec. 5.2 with two single-particle functions, i.e. the two-mode MCTDHB model, we find effects of fragmentation of the condensate. This indicates a macroscopic occupation of both natural orbitals (see Sec. 2.6.3). Furthermore, we discuss resulting superposition states, in particular so-called *NOON* states. The multi-mode MCTDHB model presented in Sec. 5.3 shows deviations compared to the two-mode results, especially for small particle numbers. Therefore, this section is followed by a discussion of convergence properties of the MCTDHB method. We discuss the validity of the two-mode model for large

particle numbers, and investigate cases that are sensitive to small changes of the initial conditions.

5.1 Introduction to the problem

Analogous to chapter 3, in the following all observables will be scaled according to Sec. 2.3. The numerical calculations discussed in this chapter were performed for $N_g = 2001$ spatial grid points for a box of length $l_{box} = 80$, unless noted otherwise. Initially, the soliton is centred at $x \approx -7.5$ with a velocity of $v = 0.3$. In the QiwiB calculations, the single-particle functions was integrated via a seventh to eighth order Runge-Kutta method, while the \vec{C} vector was propagated by a Lanczos algorithm. The initial soliton was created by an improved relaxation method. For more details on the numerical methods we refer to App. B.

The notation used in this chapter is the same as in chapter 3. Likewise, the scattering object is again a rectangular well, as given by Eq. (3.1), with a width of $2a = 1$, and centred at $x = 0$. The reflected (R), transmitted (T) and trapped (L) part of the scattered soliton are now defined as

$$\begin{aligned} R &= \frac{1}{N} \int_{-\infty}^{-20a} dx \rho(x) \\ L &= \frac{1}{N} \int_{-20a}^{20a} dx \rho(x) \\ T &= \frac{1}{N} \int_{20a}^{\infty} dx \rho(x), \end{aligned} \tag{5.1}$$

with the one-body density $\rho(x)$. Similar to chapter 3, we define the TRL window as the range of V_0 for which the soliton does not fully reflect from the well. However, now we only focus on the TRL window around the second linear bound state inside the well. It is safe to assume that the results are similar for other resonances as well. For convenience we refer to this regime as the “second TRL ” window. In addition, the small region between full reflection and full transmission, as seen in Fig. 3.3, will now be identified as the RT window.

Furthermore, the many-body results depend on the particle number and the interaction strength. To relate the mean-field results of chapter 3 to the many-body

5.2. TWO-MODE MCTDHB MODEL

calculations, the interaction strength is defined as described in the following. In Sec. 2.6 it was mentioned that for $M = 1$ the full many-body approach effectively reduces to the GP approach. However, in MCTDHB the single-particle wave function is normalised to $\int |\phi|^2 dx = \mathcal{N} = 1$, while the normalisation of the GP wave function was given by $\mathcal{N}_{GP} = 2$. Therefore, to relate Eq. (2.15) to Eq. (2.44), and to keep the width of the initial soliton independent of N , the interaction has to take the form given by

$$g = -2N^{-1}. \quad (5.2)$$

According to Eq. 2.31 we find $A = 1/\sqrt{-g} = \sqrt{N/2}$. Hence, the soliton width is $l_s = 1$ and its energy per particle is

$$\frac{E}{N} = -\frac{1}{6} + \frac{1}{2}v^2 \quad (5.3)$$

[see Eq. (3.19)]. Both variables are independent of N , which ensures that the resonances of the soliton's eigenfrequency with a bound state in the well always appear for the same values of V_0 . A direct comparison of calculations for different N with the GP approach is now possible.

5.2 Two-mode MCTDHB model

Previous analytical [28] and numerical [29, 30, 76, 77] works studied the effect of fragmentation in an attractive condensate. In Refs. [28, 30] the authors investigated the splitting of a bright soliton into two distinguishable parts by the influence of a positive Gaussian barrier. More specifically, in Ref. [30] each one of the outgoing solitons occupies exactly one of the two available natural orbitals, which were shown to be localised and spatially separated. The final state was found to be a so-called *NOON* state, i.e. a binary superposition of the $|N, 0\rangle$ and the $|0, N\rangle$ state. Here, the numbers in the ket denote the population number of the two accessible natural orbitals, respectively. The realisation of macroscopic *NOON* states with bright solitons was discussed in Refs. [28–30]. However, *NOON* states are shown to be fragile, and therefore are limited to up to ten particles [149]. In App. A we present a different system that supports *NOON* states and discuss their

CHAPTER 5. FULL QUANTUM DYNAMICS OF SOLITON SCATTERING

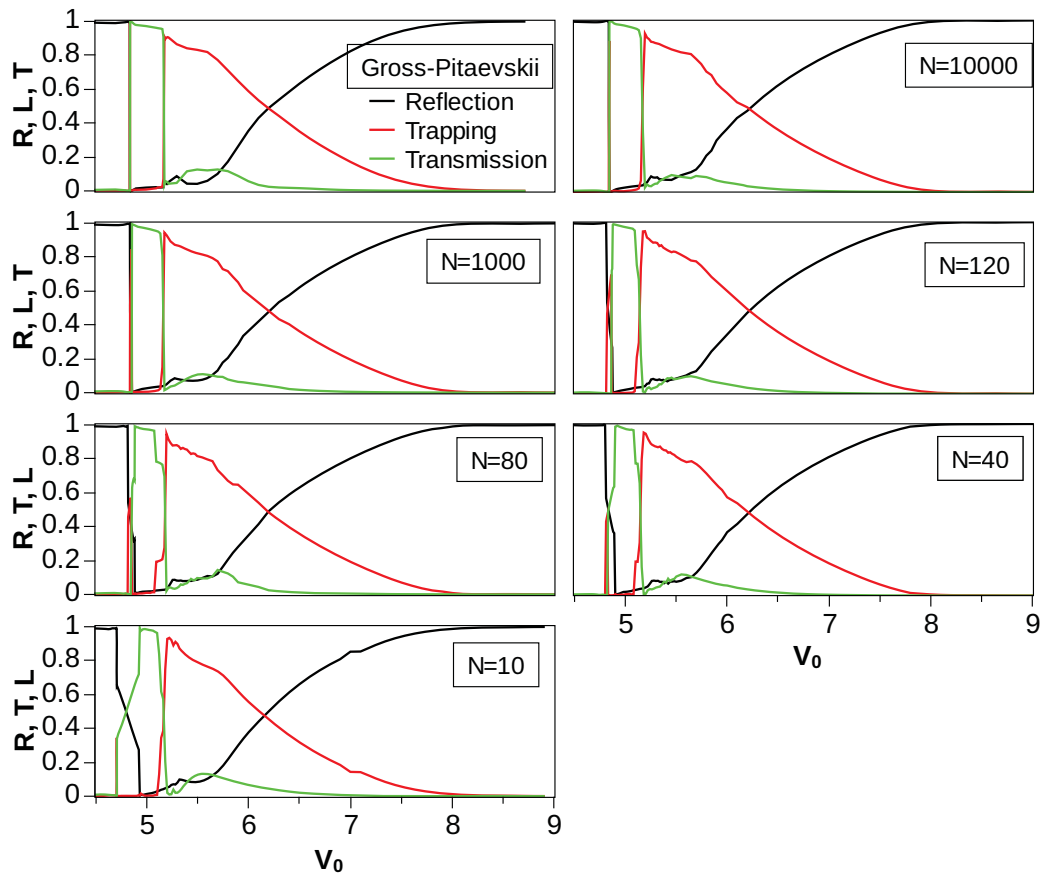


Figure 5.1: Reflection (R), trapping (T) and transmission (L) shown for the second TRL window. QiwiB calculations for different particle numbers and $M = 2$ are compared to the GP results. Differences mainly occur inside the transition regimes of reflection-transmission and transmission-trapping. Especially for low numbers of particles, i.e. $N = 10$, the changes are more significant.

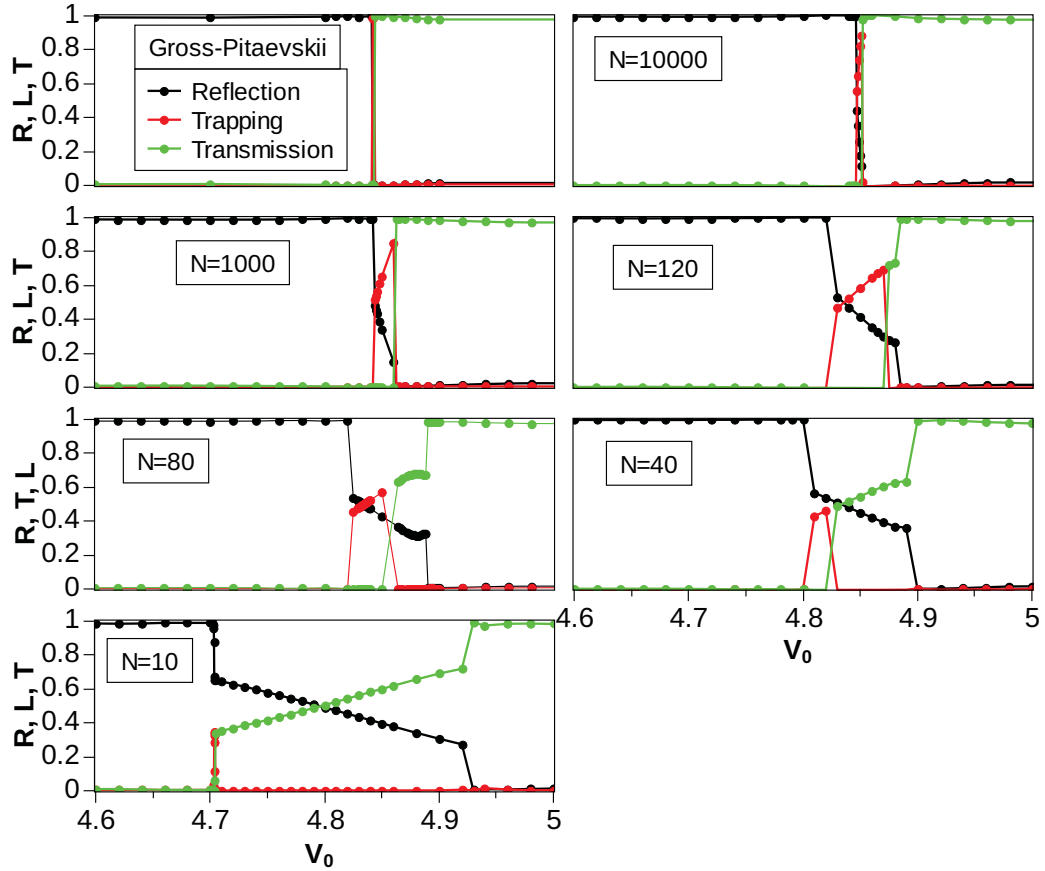


Figure 5.2: Reflection (R), trapping (T) and transmission (T) for the RT window inside the second TRL window. Qiwib calculations for different particle numbers and $M = 2$ are compared to GP results (this graph shows a section of Fig. 5.1 around the RT window). While for $N = 10000$ the GP results are very well matched, in particular its jumps in the reflection, trapping and transmission. Still, the full many-body calculations show enlarged RT windows with smoother transitions for smaller particle numbers. Notable is the reduced trapping for smaller particle numbers as well as the emergence of a splitting into a coexistence of reflection and transmission, particularly for $N = 10$.

robustness.

The work in this section was motivated by Ref. [30], where a model with two single-particle functions was shown to be sufficient to describe the splitting process. Furthermore, the full many-body approach system is expected to reveal additional interesting phenomena, e.g. fragmented condensates and binary superposition states. We note that, that those fragmented and superposition states are not accessible in the Gross-Pitaevskii approach, in contrast to a two-mode MCTDHB approach.

5.2.1 *TRL* window for the second bound state

Calculations on the second *TRL* window for different particle numbers are demonstrated in Fig. 5.1. The figure's panels reveal little difference compared to the Gross-Pitaevskii results for the vast majority of the potential depths. However, the graphs inside the transition regimes between full reflection and full transmission as well as full transmission and full trapping clearly deviate from the GP results, especially for smaller N . Considering Fig. 5.2, the *RT* window is shown to become significantly larger for decreasing N . Furthermore, a trapping mechanism similar to the one found in the GP approach, as described in Sec. 3.4.2, is only observed for a very small range of V_0 . However, the many-body approach shows that the range of V_0 , for which trapping occurs, is larger compared to the GP case, even for $N = 10000$. Smaller N increase this range, but also reduce the maximally possible trapping. This can be seen in the graph for $N = 120$. In this case, the *RT* window comprises cases of partial trapping and partial reflection as well as partial reflection and partial transmission. For a very small number of particles, i.e. $N = 10$, the trapping almost vanishes, despite a very narrow region around $V_0 = 4.704$, where still up to 30% of the particles can be trapped.

5.2.2 *NOON*-like superposition states inside the *RT* window

In Ref. [30] it has been shown that a soliton can split into a superposition state via scattering on a positive barrier. Similarly, this can also be achieved in our model with a well. We now consider the $N = 80$ case, mainly for numerical reasons (see App. B.3.6), but also because the new structures in the *TRL* window are

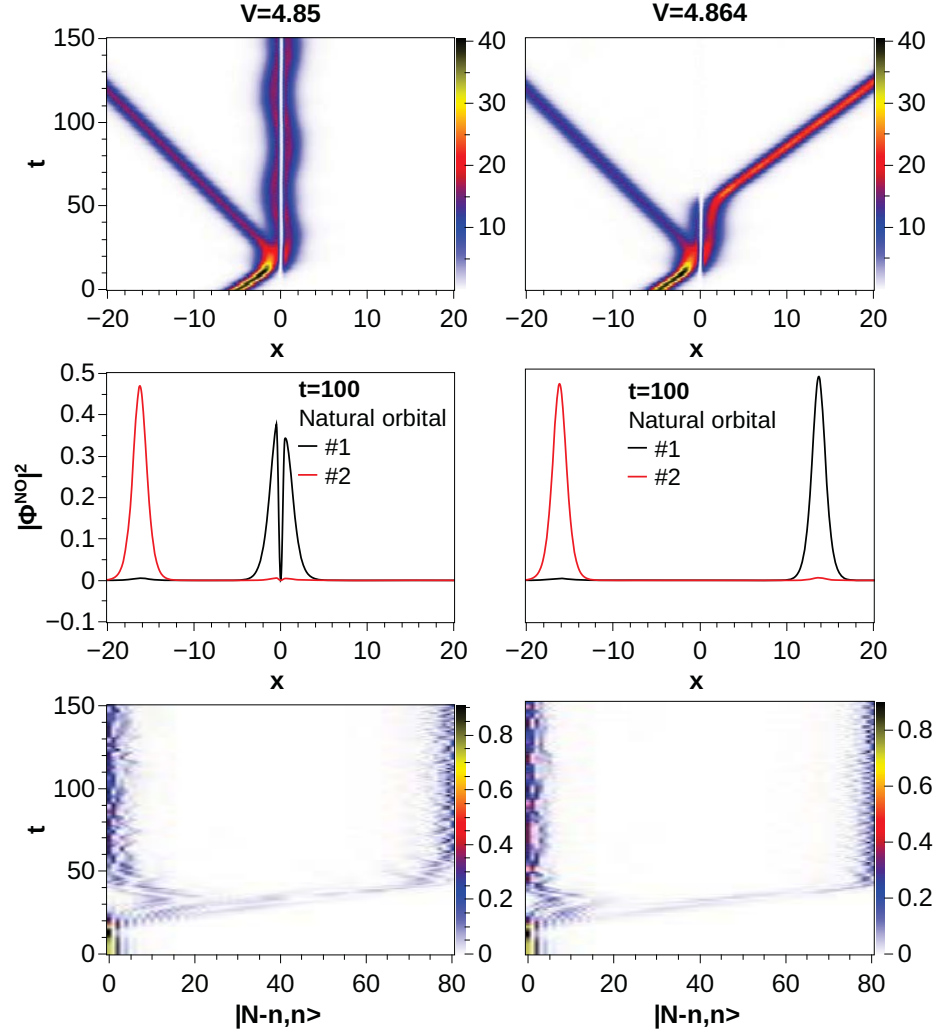


Figure 5.3: Top panel: Time evolution of the one-body density for $N = 80$ and $M = 2$. For $V_0 = 4.85$ the incoming soliton splits into a reflected ($\sim 43\%$) and a trapped part ($\sim 57\%$), while for $V_0 = 4.864$ the soliton splits into a reflected ($\sim 37\%$) and a transmitted ($\sim 63\%$) soliton. Middle panel: The absolute square of the natural orbital amplitudes $|\phi_i^{NO}|^2$. For both V_0 , the two natural orbitals are localised and well separated from each other. Therefore, the percentages given previously relate to the natural orbital population number. By definition the total state is a fragmented state. Bottom panel: population of the expansion coefficients $|C_{N-n,n}|^2$ for the Fock states $|N - n, n\rangle$ in the natural orbital basis. Only states close to $|N, 0\rangle$ and $|0, N\rangle$ are highly populated, and therefore the resulting state is approximately a *NOON* state.

CHAPTER 5. FULL QUANTUM DYNAMICS OF SOLITON SCATTERING

clearly visible. Fig. 5.3 presents studies for $V_0 = 4.85$ and $V_0 = 4.864$. The top panel in Fig. 5.3 shows the time evolution of the one-body density, the middle panel presents both natural orbitals $|\phi_i^{NO}(x)|^2$, and the bottom panel gives the populations of all expansion coefficients $|C_{N-n,n}|^2$ for its respective many-body Fock states $|N-n, n\rangle$ [see Eq. (2.40)] in the natural orbital representation. The graphs for $V_0 = 4.85$ show an example of a soliton being split into a reflected and a trapped part, while for $V_0 = 4.864$ the soliton is broken up into two counter-propagating parts. Furthermore, Fig. 5.3 clearly reveals that for both potential depths, the initial soliton splits into two parts, each one populating exactly one of the two natural orbitals. In addition, these natural orbitals are both localised and well separated from each other. Furthermore, the population of the expansion coefficients exhibits the final state to be close to a *NOON* state, i.e. a state defined as the superposition of $|N, 0\rangle$ and $|0, N\rangle$ states. However, we note that, in the two cases presented here, both states are not equally populated, i.e. the final state is not given by $\propto |N, 0\rangle + |0, N\rangle$, but by $\propto \alpha|N, 0\rangle + \beta|0, N\rangle$ with $|\alpha| \neq |\beta|$, instead.

Overall, it is remarkable that the formation of a *NOON* state can always be observed inside the *RT* window, independent from the particle number. However, for large N , only the trapping-reflection case survives (see also Fig. 5.2).

5.3 Multi-mode MCTDHB models

So far, the previous results for $M = 2$ single-particle functions are consistent with earlier observations from Ref. [30]. However, the case of $M = 2$ is only a low order approximation. Therefore, convergence properties of our results need to be studied to verify our findings.

We again investigate properties of the second *TRL* window. Considering the big changes in the *RT* window, studies on $N = 120$ and $N = 10$ particles with up to $M = 4$ and $M = 8$ modes, respectively, are presented. Later, a study on the natural orbital populations will be presented, which provides an extensive discussion of the limitations related to the truncation of the Hilbert space within the MCTDHB approach.

5.3.1 *TRL* windows for the two-mode MCTDHB

N=120 particles

Fig. 5.4 shows the *TRL* window for the number of single-particle functions $M = 2, 3$ and 4 . The panels for different M in Fig. 5.4 are very similar. Differences, however, can be found at the transition regimes. We notice that the range of potential depths, where full transmission occurs, decreases for increasing M . Furthermore, the sharp changes in transmission, reflection and trapping disappear and are replaced by smoother transitions from one regime into the other. Therefore, new scattering states emerge, for example the *NOON* states of two solitons propagating away from the well. This is, however, not entirely unexpected. Of course, the inclusion of more single-particle functions adds more degrees of freedom and produces non-trivial as well time-dependent shifts in the natural orbital population numbers.

N=10 particles

The Hilbert space increases exponentially with increasing number of modes M and particle number N . Therefore, in order for the numerical calculations to be feasible, a doubling of the maximal M from $M = 4$ to $M = 8$ requires a reduction of the number of particles to $N = 10$. Furthermore, we reduced the number of spatial grid points to $N_g = 881$ to reduce the CPU times (we checked that the differences to the calculations for $N_g = 2001$ are negligible). The panels in Fig. 5.5 for calculations with $N = 10$ particles show that the influence of additional single-particle functions is very strong. For $M = 8$ the *TRL* window is very rich of different combinations of reflection, trapping and transmission. To give an example, Fig. 5.6 shows a four-fold fragmentation into a superposition state of four separate solitons. Additionally, the maximal possible transmission and trapping are significantly smaller compared to results for $M = 2$. Even though the pattern seen in the graphs in Fig. 5.5 seem to converge, accurate results for $M \rightarrow \infty$ are still difficult to predict.

It is also worthwhile to study the time-dynamics of the natural orbital populations ρ_i . Fig 5.7 relates the occupation numbers of the three most significant

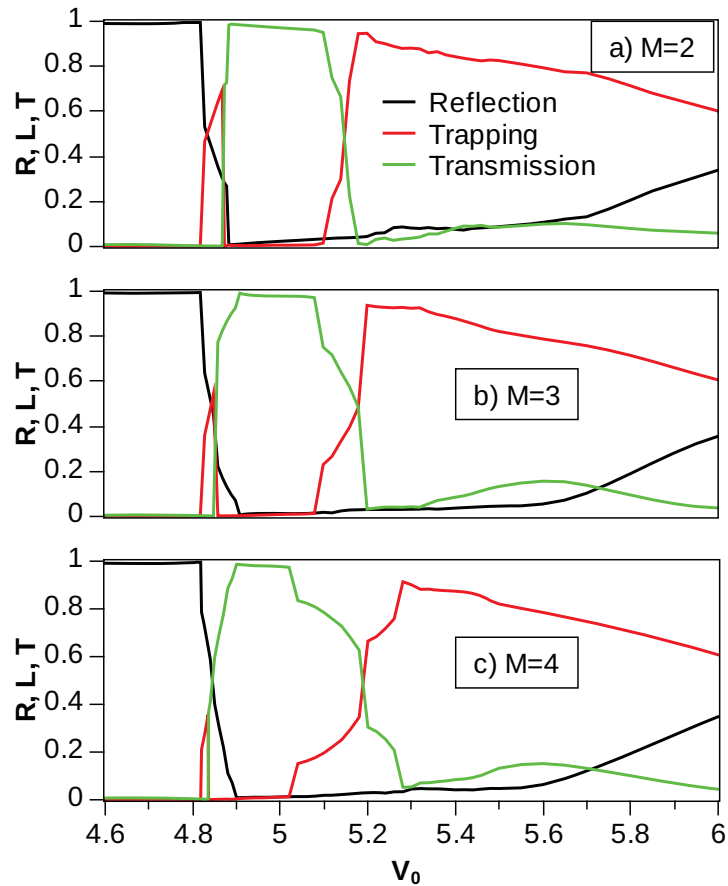


Figure 5.4: The second TRL window for $N = 120$ particles and $M = 2, 3, 4$ modes. Details around the transition regimes change, e.g. inside the RT window, for increasing M . For $M = 4$ the trapping inside the RT window is reduced compared to smaller number of modes. In addition, the soliton can now equally split into a reflected and transmitted part. The jumps in the curve for $M = 2$ between the full reflection, trapping and full transmission windows are replaced by smoother transitions in the $M = 4$ case.

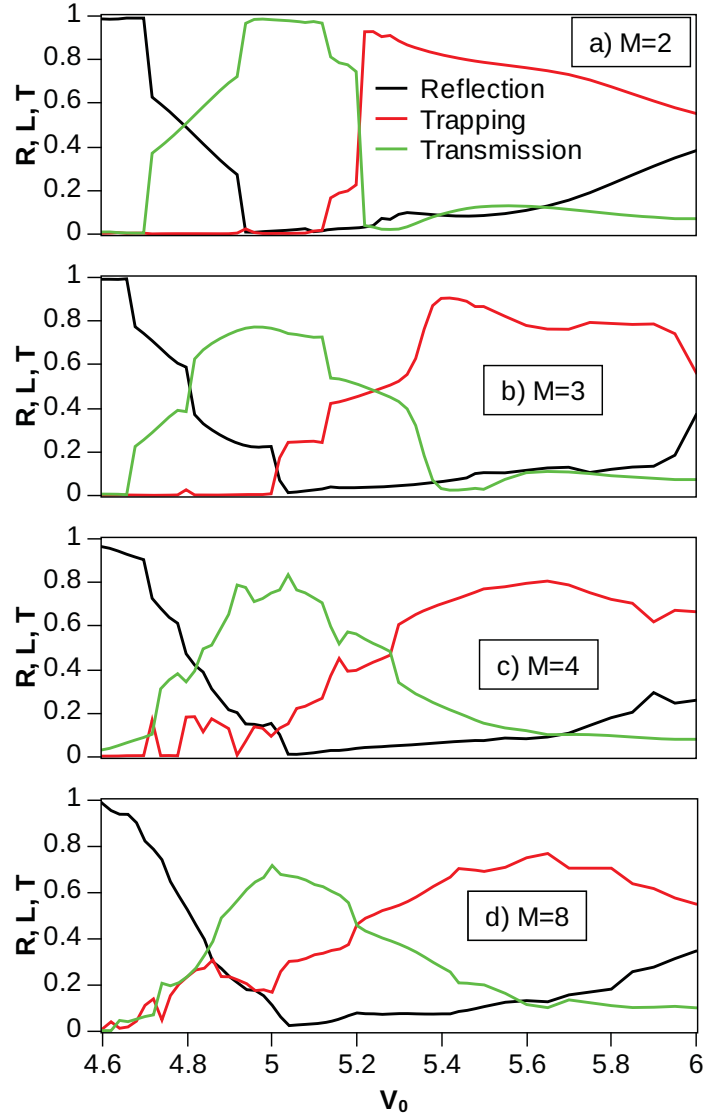


Figure 5.5: T , R and L in the second TRL window for $N = 10$ particles and $M = 2, 3, 4, 8$ modes. From top to bottom, we find that the maximal transmission and trapping are reduced ($\sim 100\% \rightarrow \sim 75\%$). The transitions resulting from our calculations are all flattened out and much smoother going from $M = 2$ to $M = 8$. We also find a new regime at $4.7 < V_0 < 5$, where trapping, transmission and reflection occur simultaneously. This was not found for calculations with $M = 2$. However, the results obtained for $M = 5$ and especially for $M = 6, 7$ (not shown here) are already very similar to the findings for the $M = 8$. This is an indication that the results will converge and may not change significantly if we increase M even further.

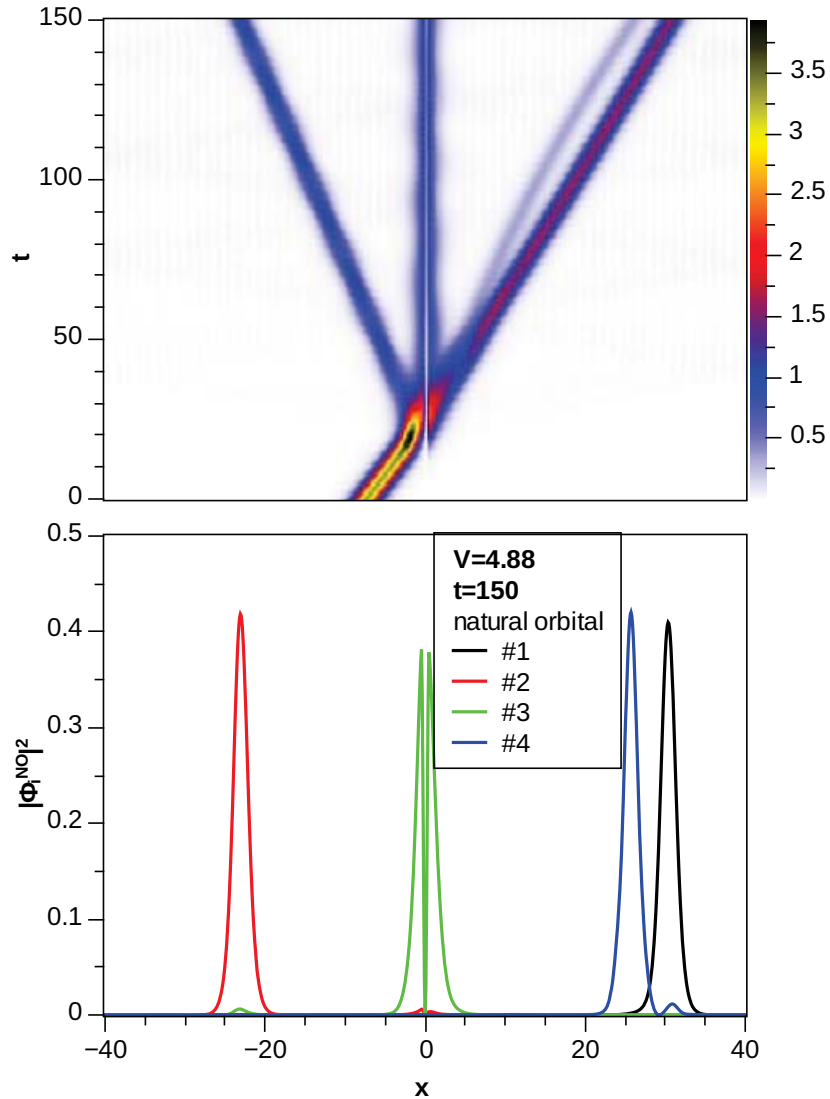


Figure 5.6: Top panel: Time evolution of the one-body density for $N = 10$ and $M = 8$. The initial soliton splits into 4 solitons after the collision with the well. Bottom panel: The four most populated natural orbitals. They are all localised and separated from each other and therefore describe a four-fold fragmented state. The natural orbital populations are 38%, 25%, 19%, and 8%, respectively.

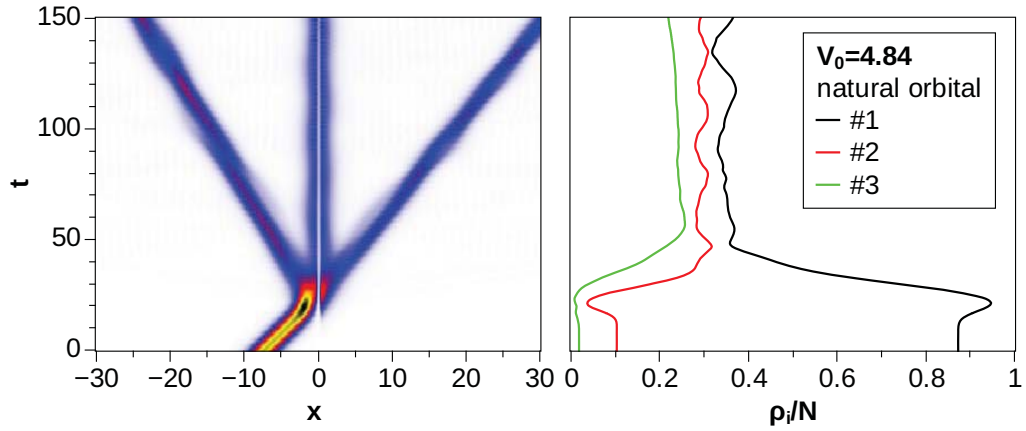


Figure 5.7: The time evolution of the populations ρ_i for the most important three natural orbitals (right graph) and the total density (left graph) for a calculation with $N = 10$, $M = 8$ and $V_0 = 4.84$. Initially most particles occupy the first natural orbital by $\sim 87\%$. After the scattering event, where ρ_1 increases to a maximal value of ~ 94.7 , the natural orbitals are approximately evenly populated with some oscillations still occurring.

natural orbitals for a calculation with $M = 8$ and a potential depth of $V_0 = 4.84$. It shows a very unusual behaviour. The initial population numbers are $\sim 87.3\%$, $\sim 10.3\%$, and $\sim 1.8\%$ for the first, second, and third natural orbital respectively. However, after $t = 21.5$ we find a peak value for $\rho_1/N = 0.947$. This is where the incoming soliton hits the barrier. Afterwards, the particles spread out and the occupation numbers converge to approximately 30%. Even though these results are somewhat unexpected, we note that the scattering event itself is a highly dynamical process and it is very difficult to track the resulting changes to the wave function. Therefore, it is no surprise to us that there are non-trivial mechanisms involved, and that the nonlinear terms in Eq. 2.44 can lead to unexpected behaviour.

5.3.2 Loss of coherence for multi-mode systems

In Sec. 5.2.2 we already discussed *NOON* states as a result of calculations for $M = 2$ modes. Yet, in the previous subsection it was shown that calculations for $M > 2$ lead to deviations and significant populations of more than two natural

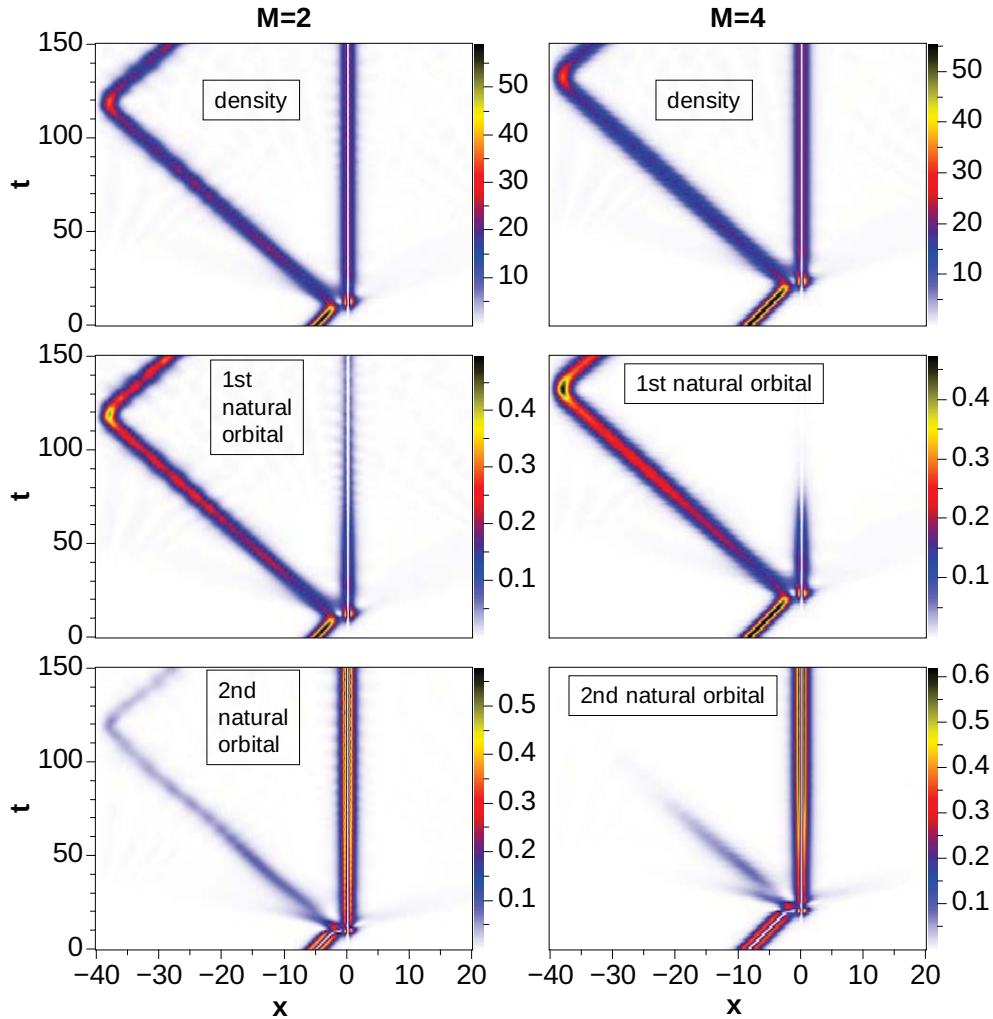


Figure 5.8: Time evolution of the density (top panel) and the two most populated natural orbitals $|\phi_i^{NO}|^2$ for $N = 120$ particles, the potential depth $V_0 = 6.5$ and $M = 2$ as well as $M = 4$ modes. Clearly, for $M = 2$ the two natural orbitals are delocalised at all times, even though a slight localisation is observable. For $M = 4$ the natural orbitals start out delocalised right after the scattering event but quickly converge to a localised shape.

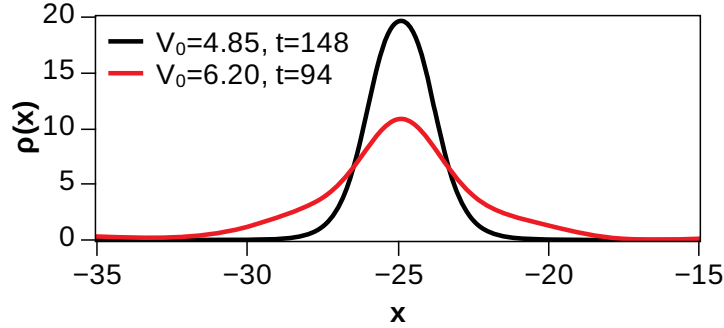


Figure 5.9: Density of the reflected part of the initial soliton for $V_0 = 4.85$ (*NOON* state regime) and $V_0 = 6.2$. This graph shows results from calculations for $N = 120$ particles and $M = 3$ modes. In both cases half of the particles are reflected and form the density humps shown in the figure. This figure shows that for $V_0 = 6.2$ the width of the reflected part is much larger compared to the case for $V_0 = 4.85$, and therefore the final state for $V_0 = 6.2$ is not a superposition anymore, but a fragmented state, as explained in more detail in the text.

orbitals, which hinders the creation of *NOON* state.

Consider now the regime of potential depths given by $5.2 \leq V_0 \leq 9$, which was not discussed in detail yet. In this window of potential depths, the GP wave function is delocalised, exhibiting two maxima in the amplitude, which is equivalent to two humps in the density function. One of those humps is moving to the left while the other one remains above the well (see Sec. 3). However, in Fig. 5.8, which demonstrates results obtained from QiwiB calculations for $N = 120$, $M = 2$, and $V_0 = 6.5$, it is obvious that not just one but both natural orbitals are delocalised. Both are significantly occupied with 67% of the particles populating the first natural orbital. Similar to the GP results, the total wave function is coherent, as can be seen from the one-body density matrix $\rho(x_1, x_2, t)$ given in Eq. (2.41). The off-diagonal elements of $\rho(x_1, x_2, t)$ are a measure for coherence. Interestingly, for $M = 2$, the time evolution of $\rho(x_1, x_2, t)$ shown in Fig. 5.10 reveals that the coherence between the two density humps reduces slowly over time. At the same time, we find in Fig. 5.8 that the natural orbitals are slowly localising with time.

For $M = 4$ the loss of coherence between the two density humps is much more pronounced. Just after the scattering event, both natural orbitals are still

CHAPTER 5. FULL QUANTUM DYNAMICS OF SOLITON SCATTERING

delocalised and macroscopically populated. Afterwards, they smoothly change their shape and become localised at $t > 80$, with one soliton moving to the left and the other one trapped in the well. This can be seen in Fig. 5.8. In addition, the off-diagonal elements of $\rho(x_1, x_2, t)$ disappear for $t > 80$ (see Fig. 5.10), which relates to a total loss of coherence between both density humps and therefore between both natural orbitals as well.

The final state now corresponds to two independent solitons, and not a *NOON* state anymore. This can be seen in Fig. 5.9, which compares the shapes of the reflected density humps for $V_0 = 4.85$ (*NOON* state regime) and $V_0 = 6.2$ for $N = 120$ and $M = 3$. We found a transmission amplitude of $\approx 50\%$ in both cases, i.e. ≈ 60 particles in each reflected density hump. We found in Sec 5.2.2 that the state for a potential depth of $V_0 = 4.85$ is approximately a *NOON* state, and therefore its reflected part is comparable to the shape of the initial soliton. Compared to this state, we find from Fig. 5.9 that width of the reflected density hump for $V_0 = 6.2$ is clearly larger and its amplitude is much smaller. We checked that this solution has a similar shape compared to a GP soliton with $\approx N/2$ particles. From this and Fig. 5.10, we conclude that the final state is not a superposition state, but a fragmented state of two solitons, which are incoherent to each other.

Furthermore, we note that a similar decoherence effect to one mentioned above was discussed in Ref. [150]. There, it was shown within the GP approach that the loss of coherence between spatially separated solitons in a so-called soliton train was related to an uncertainty in the relative phase difference between them. The authors derived an analytical expression for the decoherence time t_{coh} assuming that all solitons have equal particle numbers. Applied to our problem, this would lead to $t_{\text{coh}} \approx 88$. This is close to an estimated coherence time of ≈ 50 found in our calculations, which was measured as the time between the start of the splitting process at $t \approx 30$ and the total loss of coherence at $t = 80$. The difference between the two coherence times could be related to the fact that in our calculation for $V_0 = 6.5$ the initial soliton does not split up equally and that more than two natural orbitals are populated, even though their contribution is small. It appears that the model in Ref. [150] is consistent with our simulations data. For a different purpose, decoherence effects of solitons described by permanently delocalised natural orbitals have been previously discussed in Ref. [77].

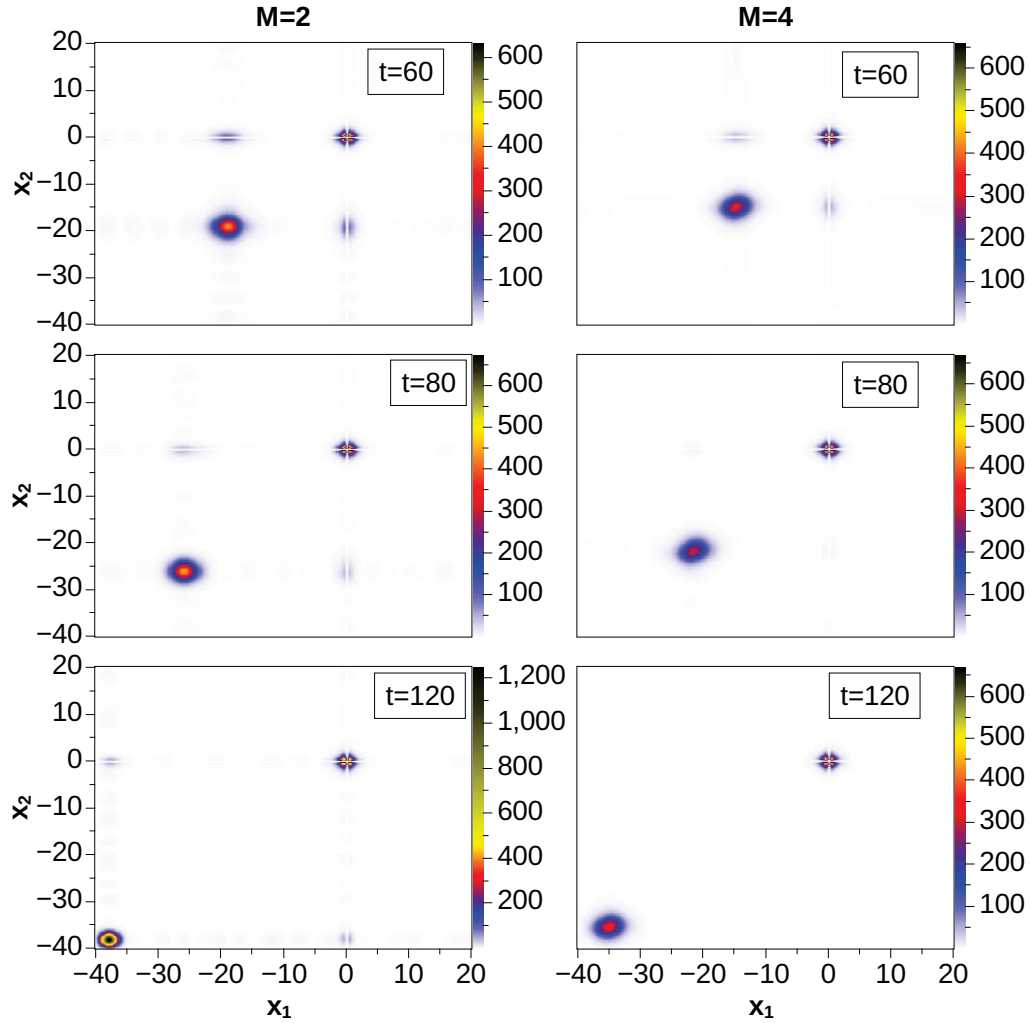


Figure 5.10: Absolute square of the one-body density $|\rho(x_1, x_2, t)|^2$ calculated for $N = 120$, $V_0 = 6.5$ and $M = 2$ (left column) as well as $M = 4$ (right column). Snapshots from top to bottom are for $t = 60, 80, 120$. In both cases the off-diagonal elements of $\rho(x_1, x_2, t)$ decrease. While for $M = 2$ they still remain finite for large times, they already vanish at $t = 80$ if $M = 4$.

After $t = 80$ the two highest occupied natural orbitals account for the vast majority of the particles, i.e. for 57% and 37%, respectively.

For an increased number of particles, i.e. $N = 10000$, the second natural orbital population for calculations with $V_0 > 5.2$ peaks at only 3% (see bottom panel of Fig. 5.12). It is therefore negligible, which is a clear indication that MCTDHB calculations reproduce the GP results for very large particle numbers, and that, after the splitting process, the two density humps maintain their global coherence.

5.4 Convergence properties

5.4.1 Motivation

In Sec. 5.3 several cases were presented, which demonstrated that the results of Qiwib calculations depend on the number of single-particle functions M . We found that a simple two-mode model is not sufficient anymore to model the system properly. This is especially true for small particle numbers as can be seen in Fig. 5.5. More single-particle functions lead to a better description of the full many-body system. Therefore, effects found in the two-mode model, that are very sensitive to changes of the initial parameters, may change or even disappear for calculations with $M > 2$.

To give an example, we present calculations for $N = 80$ and $M = 2$ in Fig. 5.11, right at the edge of the full reflection regime of the TRL window at $V_0 = 4.82$. The top panel in Fig. 5.11 shows the time evolution of the natural orbital populations. The initial total state in the Qiwib calculations was very similar to an exact soliton solution obtained from the GP approach, that is $\rho_1/N = 0.99$ at $t = 0$. After the scattering event, once the soliton is positioned at a distance of several soliton widths from the well, ρ_1 is still highly populated with $\sim 93\%$. However, during the impact with the well, ρ_1 drops to $\sim 56.4\%$. The magnitude of this drop is about the same as in calculations, which are not shown here, for $V_0 = 4.83$. There, we find that where after the collision the initial soliton splits into a reflected ($\rho_1 \approx 0.52$) and a trapped part ($\rho_1 \approx 0.48$). For $V_0 = 4.82$ similar results are found from the density plot in the bottom panel of Fig. 5.11, which reveals that during and shortly after the impact with the well, the initial soliton starts to split into

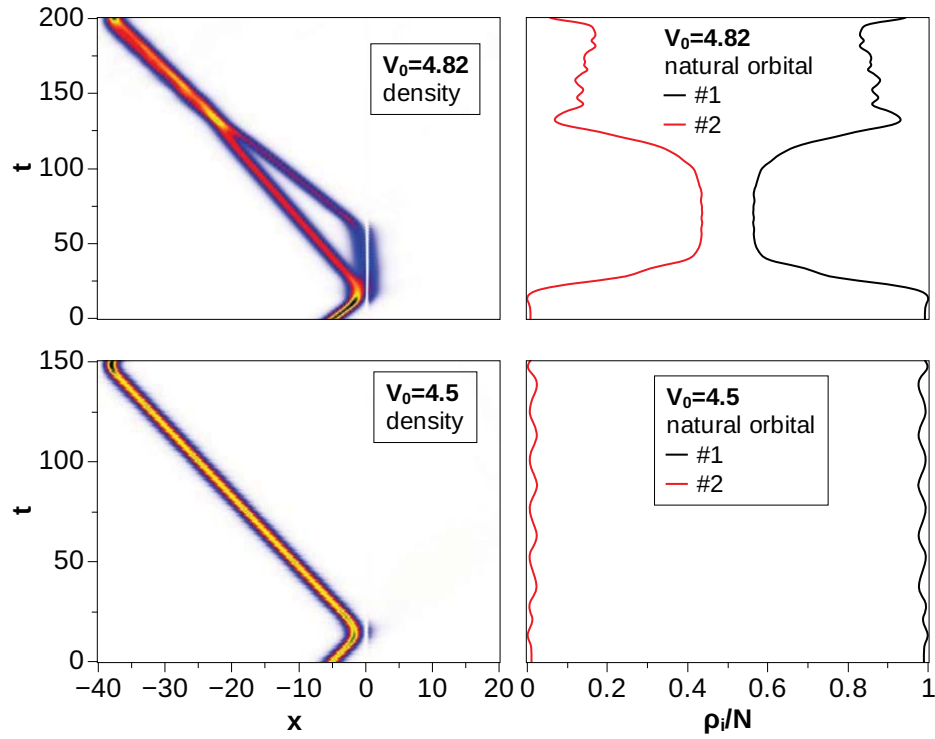


Figure 5.11: Density (left) and natural orbital populations (right) for $N = 80$ and $M = 2$ at $V_0 = 4.82$ (top graphs) and $V_0 = 4.5$ (bottom graphs). For the former, the initial soliton fragments into a reflected and a trapped part. After $t \approx 50$ the trapped soliton starts to escape from the well and moves towards the previously reflected part with a higher centre of mass velocity. At $t \approx 100$ the two solitons begin to merge and partially regenerate the initial state of one soliton. For $V = 4.5$ the interaction time of the incoming soliton with the well is negligible, and therefore reflects completely without fragmenting.

CHAPTER 5. FULL QUANTUM DYNAMICS OF SOLITON SCATTERING

	n=1	n=2	n=3	n=4
M=2	55%	45%	-	-
M=3	60%	32%	8%	-
M=4	59%	29%	11%	1%

Table 5.1: Population numbers for the n th natural orbital for $N = 80$ particles and $M = 2, 3, 4$ modes, and the potential depth $V_0 \approx 4.82$ at $t \approx 60$. For $M = 2$ a threshold of $\approx 45\%$ for the population of the second highest occupied natural orbital can be identified, above which the trapped soliton remains bound to the well until the end of our simulations. This threshold is significantly reduced for $M = 3$ and $M = 4$, and it remains unclear if the final state of two reflected solitons in Fig. 5.11 is still existent for $M \rightarrow \infty$.

two solitons, a reflected one and a trapped one.

To our knowledge, there is no clear explanation for the initial break-up during the impact on the well, but it may be related to the length of the time period during which it interacts with the well. For $V_0 = 4.5$ the soliton density barely enters the well and is reflected very quickly and we find $\rho_1 > 0.975$ at all times (see bottom panel of Fig. 5.11). This is in stark contrast to $V_0 = 4.82$, where the soliton almost completely covers the well for a finite period of time. This could lead to dynamical processes that allow for a coupling between several Fock states and therefore an increased population of natural orbitals other than the highest occupied one.

However, Fig. 5.11 also shows that a short amount of time after the scattering process, the trapped soliton escapes the well travelling into the same direction as the previously reflected soliton. The velocities of both solitons clearly differ, and therefore it is possible for the previously trapped soliton to catch up with the other one. Hence, they collide at $t \approx 120$ and the natural orbital populations, which are shown in the top panel of Fig. 5.11, change to form only one macroscopically populated natural orbital, i.e. only one coherent soliton.

For $M = 2$ modes we can identify a threshold on the population of the second natural orbital for the temporal trapping. Once the second natural orbital is occupied by more than $\sim 45\%$ of the particles, the initial soliton gets partially trapped

by the well for the remainder of our simulations, which usually run until $t = 200$. Increasing the number of modes M now alters this effect. For $M = 3$ and $M = 4$ the threshold on the second natural orbital population for the temporal trapping is significantly reduced, and even though the differences between the results for $M = 3$ and $M = 4$ are much smaller compared to those for $M = 2$ (see Table 5.1), it is still unclear whether the results are converged in this parameter regime and the splitting into two reflected solitons, as shown in Fig. 5.11, is physical.

This example, together with the results from Sec. 5.3, show that calculations for $M = 2$ can be misleading and a detailed study of the convergence properties is needed.

5.4.2 Discussion

Calculations based on finite basis sets are numerically limited to a certain size of the Hilbert space. Therefore, convergence studies are necessary to determine if a given basis set is sufficient to describe the physics of the system. In our case, if the addition of one single-particle function results in a negligible population of the additional natural orbital, the system is expected not to significantly change, even for larger M . Still, the conclusions drawn from those calculations might not properly represent the physical reality, but only give an indication of it. Therefore, the results have to be examined thoroughly and either compared with analytical considerations, experimental results or other numerical work based on different approaches.

For the system discussed in this chapter, to assess the convergence properties by numerical means, we present Fig. 5.12. It shows the relative natural orbital populations $\rho_{i \geq 2}^{\max}$ for different particle numbers and their respective numerically feasible maximal number of single-particle functions. For convenience the first natural orbital is left out of the graphs. For a specific V_0 , we define ρ_i^{\max} as the maximal natural orbital population number that is found during and after the scattering process.

Table 5.2 summarises the maximal population numbers inside the RT window, $\rho_i^{\max, RT}$, for all natural orbitals. Clearly, $\rho_i^{\max, RT}$ decreases significantly for a larger number of particles. We already find a relatively small population of only 9%

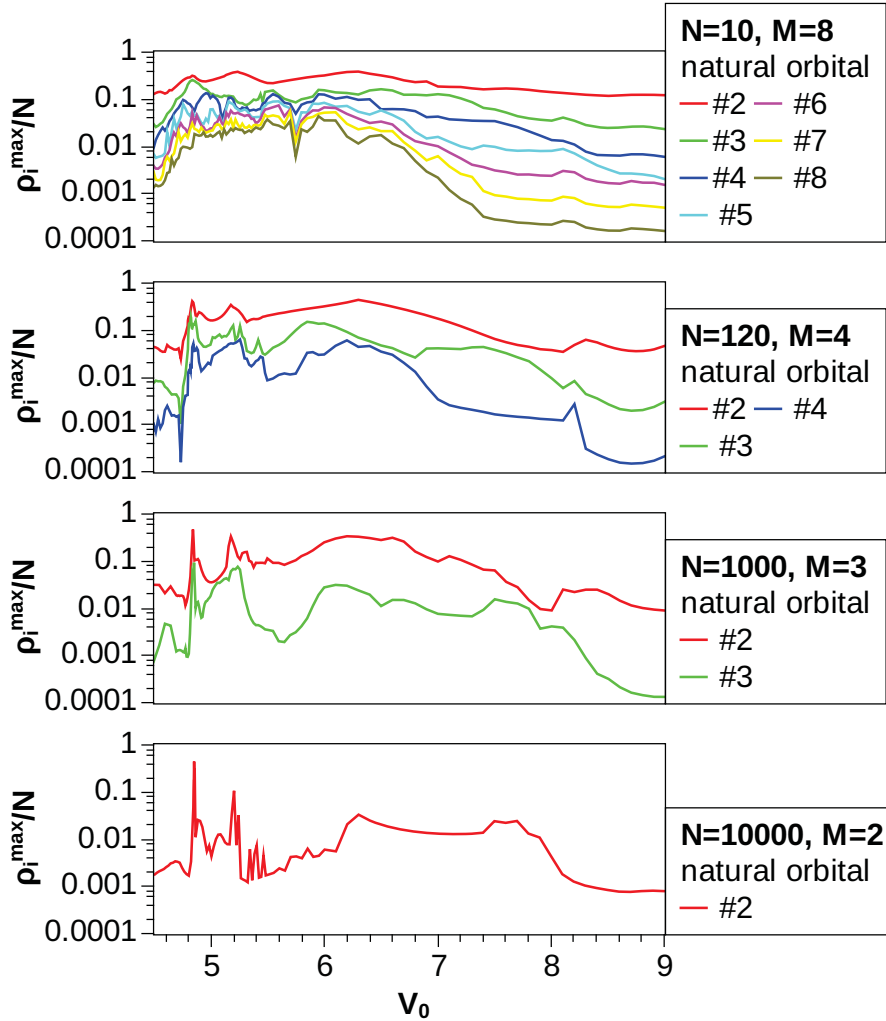


Figure 5.12: Maximal relative natural orbital populations ρ_i^{\max} found during simulation runs for each potential depth V_0 . For each N the calculations presented here were performed for the respective maximal numerically feasible M . The panels do not show ρ_1^{\max} for the first natural orbital as it is close to one for all cases. From top to bottom fewer natural orbitals are significant. In the case of $N = 10000$ the second natural orbital has a high population only for $V_0 \approx 4.847$ while for all other values of V_0 it does not exceed 10%. For $N = 1000$ the population of the third natural orbital is always below 10% while for $N = 120$ the maximal population of the fourth natural orbital is $\lesssim 5\%$. The convergence for large particle numbers is therefore much more rapid. More population numbers are given and discussed in Table 5.2.

5.4. CONVERGENCE PROPERTIES

	N=10	N=120	N=1000	N=10000
M=2	31%	41%	47%	45%
M=3	26%	19%	9%	-
M=4	13%	5%	-	-
M=5	8%	-	-	-
M=6	5%	-	-	-
M=7	3%	-	-	-
M=8	2%	-	-	-

Table 5.2: Maximal relative natural orbital populations $\rho_i^{\max, RT}$ inside the RT region taken from Fig. 5.12. For $N = 10$ the population numbers seem to converge with increasing number of modes M . There is also a rapid decrease in the population of the natural orbital $M = 3$ and $M = 4$ for increasing particle numbers. The numbers in this table show that a fifth single particle function is expected to result in the population of its respective natural orbital of $\ll 5\%$ and is therefore negligible. Likewise, for $N = 1000$, an extrapolated value for the population of a fourth natural orbital is given by $< 5\%$. We also expect a third natural orbital for the $N = 10000$ to only give a minimal contributions. However, the second natural orbital is still highly occupied. This is related to the splitting process found at the transition regime between full reflection and full transmission.

CHAPTER 5. FULL QUANTUM DYNAMICS OF SOLITON SCATTERING

for the third natural orbital and $N = 1000$, which is comparable to the result for $N = 10$ and $M = 5$. Therefore, two natural orbitals less are needed for the $N = 1000$ case as compared to $N = 10$ in order to reach a comparable accuracy. The same holds for the results with $N = 120$ and $M = 4$ as compared to $N = 10$ and $M = 6$. Table 5.2 as well as Fig. 5.12 show that the population numbers smoothly decrease, and therefore the expectation is, that for large M , they would eventually converge. Indeed, we find that for $N = 10$ the differences in our results for $M = 6$ and $M = 8$ are already rather small, and that all the features from the $M = 8$ results are present for $M = 6$ as well. This is not surprising, as the populations of the seventh and eighth natural orbital add up to just 5%. Therefore, we expect that it is not necessary to go beyond $M = 4$ for $N = 120$. Even though it is not possible (yet) to perform calculations with $M = 4$ and $N = 1000$, the results for smaller particle numbers suggest that $M = 3$ is sufficient and that a fourth natural orbital population is expected to not exceed 5%. Analogously, for $N = 10000$ a third natural orbital most likely does not surpass 5%.

The results presented above coincide with investigations on ground state solutions for bright solitons, obtained from relaxation calculations with Qiwib. They were used as the initial wave functions for the time-dependent simulations above. In the case of $N = 120$ and $M = 2$ the first natural orbital has a very high occupation number of $\rho_1/N \gtrsim 0.99 \hat{=} 99\%$, while for $M = 3$ this number is slightly decreased to $\sim 98.3\%$. Even though the many-body solution resembles the GP soliton extremely well, additional single-particle functions, and therefore a larger Hilbert space, show small deviations. For $N = 10$ the differences are even more noticeable, where the population of the first natural orbital decreases from $\sim 97\%$ ($M = 2$) and $\sim 94.8\%$ ($M = 3$) to $\sim 87.3\%$ ($M = 8$). Therefore, up to 13% ($M = 8$) of the particles occupy the remaining natural orbitals, a significantly high number. From results for $M = 2 - 10$ a fit curve for the highest occupation number is found and given by $\rho_1/N \approx 0.81 + 0.19 \exp(-(M - 1)/6.5)$. Therefore, it is expected that $\rho_1/N \rightarrow 0.8$ for $M \rightarrow \infty$. This is a rough estimate, but it shows the order of fragmentation due to the reduced ρ_1 . Nevertheless, it is expected that for larger particle numbers $\rho_1/N \approx 1$ a smaller number of natural orbitals would sufficiently describe the system, e.g. $M = 3$ for $N = 1000$ where $\rho_1/N \approx 1$.

However, even though many interesting many-body effects are involved in the

scattering process, we found that, at least for large particle numbers, the Gross-Pitaevskii approach is still valid and gives meaningful results. Only at the transition regimes does the full quantum dynamics become important and leads to interesting phenomena, e.g. fragmentation and binary superposition states.

5.5 Summary

In this chapter we explored the full quantum many-body physics of the scattering of a soliton on a well, from which two main results can be extracted.

First of all, for large numbers of particles, i.e. $N = 10000$, the results from Qiwib calculations closely match those obtained from the GP theory. Hence, in this regime, the GP approach is still valid, and therefore the results discussed in chapter 3 as well.

Very small particle numbers, however, lead to enhanced quantum effects and the population of additional natural orbitals. Therefore, few-particle systems are not adequately described by a $M = 2$ model. However, for increasing particle numbers, in particular $N \geq 120$, a rapid drop of the population numbers was found, and therefore fewer single-particle functions already describe the many-body physics sufficiently. For $N = 10000$, it is expected that a third natural orbital gives a negligible contribution. Differences to the GP results always occur inside the RT window, and for small particle numbers $N \leq 1000$ for potential depths $V_0 > 5.2$. The RT window is rich with features for particle numbers as small as $N = 10$, showing superposition states and up to 4-5 significantly occupied natural orbitals.

This leads to the second main finding derived from of this chapter: The observation of $NOON$ states of a reflected soliton and a trapped one. They corresponds to the proposed macroscopic superpositions of BECs with repulsive interactions from Refs. [20–27, 31]. However, the $NOON$ states observed in this thesis are novel as they differ to previously reported $NOON$ states of counter-propagating solitons [28–30]. Experimental realisations of these states with solitons were previously discussed in Refs. [28, 30]. However, it should be noted that $NOON$ states of solitons are very fragile to particle loss and therefore difficult to create in an experimental environment.

CHAPTER 5. FULL QUANTUM DYNAMICS OF SOLITON SCATTERING

Furthermore, we performed simulations at $V_0 > 5.2$, for which the scattered soliton results in two localised humps in the density. We observed a loss of global coherence between the two density humps, which is consistent with previous mean-field results on decoherence in soliton trains [150].

The conclusions drawn in this chapter partially originate from an extrapolation of our data. We showed in sections 5.3 and 5.4.1 that the convergence of the results with respect to M is not always guaranteed. In particular, regimes that are very sensitive to the initial parameters, or small changes to the system, are more likely show unphysical effects. From the discussion in Sec. 5.4.1, however, we are confident that our data is sufficient to show that the observed *NOON* states are physical, and increasing the Hilbert space would only slightly alter the results. For instance, we believe that the splitting of the soliton into a binary superposition state, as shown in Fig. 5.13 for $N = 1000$ and $M = 3$, is expected to be achievable in experiments.

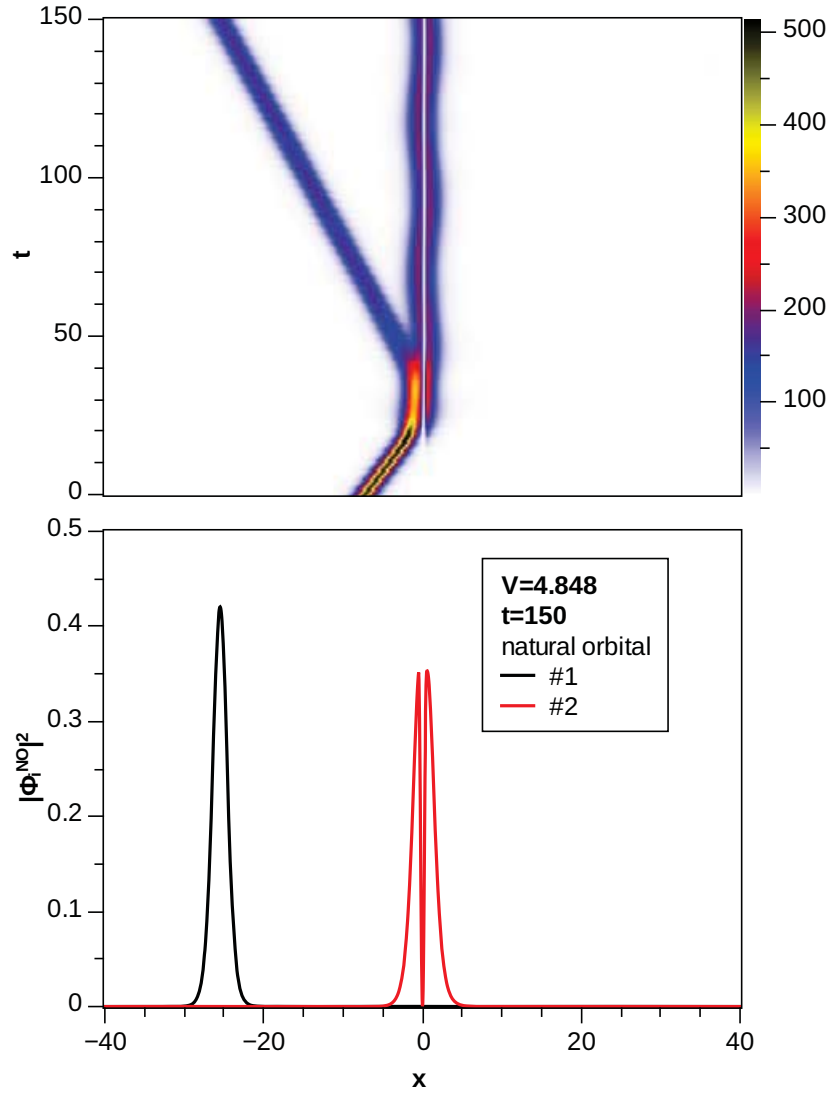


Figure 5.13: Top panel: Time evolution of the one-body density for $N = 1000$ and $M = 3$. Bottom panel: $|\phi_i^{NO}|^2$ for the natural orbitals. Similar to Fig. 5.3 the resulting state is a fragmented and again a *NOON*-like state with 55.5% of the particles in the first natural orbital and 41.5% in the second one.

The most beautiful thing we can experience is the mysterious. It is the source of all true art and all science. He to whom this emotion is a stranger, who can no longer pause to wonder and stand rapt in awe, is as good as dead: his eyes are closed.

Albert Einstein



Conclusions and Outlook

6.1 Conclusions

In this thesis we investigated the interplay of particle and resonant wave scattering including nonlinear effects. Those systems expose diverse and interesting quantum many-body physics. A better understanding of the physics in these systems could lead to new and exiting theoretical work and inspire experimentalists to further investigate these systems.

As an example of such a system, we discussed in this thesis the scattering of a bright matter-wave soliton on a narrow well. For the first time, we explained in detail the mechanism that leads to soliton trapping. Numerical and analytical work on a variational two-mode model within the Gross-Pitaevskii approach showed that a resonant coupling with a linear bound state in the well leads to transmission. We observed an additional particle loss of only a few per cent in the form of “radiation”, which slows down the transmitted soliton until it eventually gets trapped. Lastly, we derived an analytical expression to further explain the trapping.

Additionally, we investigated the soliton scattering problem within the full many-body description of the MCTDHB method by using the QiviB program. This program was developed in the course of this thesis and forms an essential part of it. We then verified the results documented above for large particle numbers and showed that for small numbers of particles quantum effects became dominant, and scattering outcomes were changed significantly. Furthermore, we observed for two separated scattered density humps at various parameter regimes a loss of global

coherence, which we were able to relate to an increasing uncertainty of the relative phase between the humps.

More interestingly, we found in our calculations novel *NOON* states, i.e. binary superposition states, of a trapped soliton and a reflected soliton. Convergence studies showed that those *NOON* states exist for a large range of particle numbers. Furthermore, we discussed the limits and the validity of the MCTDHB approach.

Since the MCTDH/MCTDHB methods are based on a finite basis set expansion, the numerical results are expected to differ from the exact results, especially in the strongly interacting regime. For this reason, we investigated convergence properties for the MCTDH/MCTDHB approaches. To improve the results, we proposed an efficient scheme to correct for the truncation of the Hilbert space. This was done by a rescaling of the interaction strength, for which we found an exact expression for a two-particle system. We furthermore demonstrated that this scheme is extendible to multiparticle systems. In that regime, the rescaling only depends on one parameter, which can be obtained by comparing the results of numerical and exact calculations. If the rescaling is applied, the numerical results presented in this thesis showed impressive improvements, for ground-state as well as excited-state calculations. This was tested for a range of systems, such as bosons in a ring system and confined to a harmonic well or a double well. Note that our proposed rescaling scheme is not restricted to the MCTDH/MCTDHB approaches, but is based on methods using finite basis sets, and therefore it can easily be applied to existing works on similar approaches, such as exact diagonalisation.

We believe that the work in this thesis will spark a significant interest in this field of research and may lead, theoretically as well as experimentally, to further advancements as well as new discoveries.

Main results:

We briefly summarise the novel research outcome presented in this thesis:

- A travelling soliton can be trapped by a well due to radiation effects. For the first time, this trapping was discussed and explained by numerical and analytical work done in this thesis.

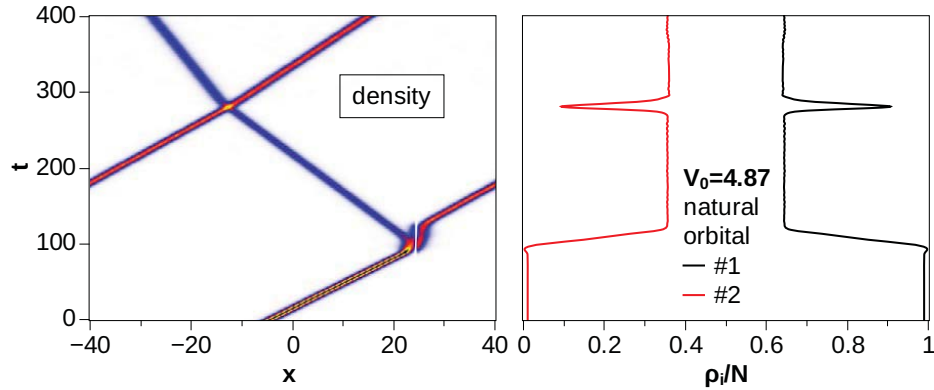


Figure 6.1: Qiwib calculations with $N = 80$ and $M = 2$ showing the density (left) of a travelling soliton in a ring of length $L = 80$, by employing periodic boundaries in the calculations. The incoming soliton splits up into two counter-propagating solitons (described by two separated localised natural orbitals) forming a *NOON* state, as seen from the natural orbital populations (right). At $t \approx 280$ the two solitons collide and almost completely merge into one coherent soliton by mainly populating only one natural orbital. After the collision they form almost the same *NOON* state as prior to the collision. However, a very small energy transfer occurred because the final velocities are slightly different now.

- Many-body theories based on finite basis set expansion become very inaccurate for large interactions. We derived a simple, yet powerful, scheme to improve the results by rescaling the interaction.
- The investigated well and its bound states lead to interesting many-body physics. In particular, novel *NOON* states were observed, which consist of reflected and trapped parts, and exist for a large range of particle numbers.

6.2 Outlook

Fig. 6.1 presents an outlook to possible future studies on the subsequent scattering of two or more solitons. It was discussed before in Ref. [28] to use *NOON* states of solitons for precision measurements. For this, the authors propose a method for observing density fringes during the collision: For an experiment, the soliton has to be brought close to its collapse threshold by increasing the density, and there-

CHAPTER 6. CONCLUSIONS AND OUTLOOK

fore the effective nonlinear interaction energy. Because this is treatable with the MCTDH/QiwiB programs, especially in combination with the rescaling scheme, future calculations could examine this proposal in more detail and assist in the interpretation and design of potential experiments. Furthermore, future studies may investigate the creation of more robust superposition states with solitons, which may be easier to realise and observe in experiments. In addition to this, it would also be of interest to study solitons in a fully three-dimensional approach to investigate the stability of the solitons and the loss of coherence due to excitation in the additional two dimensions.

We furthermore emphasise that with the MCTDH/MCTDHB methods a broad range of systems and problems can be treated. Besides the soliton scattering problem presented in his thesis, the MCTDH/MCTDHB method could be applied to problems, such as the creation of superposition states in double-wells [24, 26, 27, 31]. Furthermore, studies can be performed on self-trapping effects, interferometry of colliding condensates and Josephson junctions on a full many-body level [128]. In addition, to study problems that go beyond 1D systems and contact interactions, such as dipolar gases [151] and double ring systems [152, 153], QiwiB could be extended to solve more general problems.

A

Robust mesoscopic superposition of strongly correlated ultracold atoms - an application of the rescaling method

In Sec. 4.2 we proposed a rescaling scheme to correct for errors arising for finite Hilbert spaces. This was applied to our work in Ref. [84] where we proposed a scheme to create coherent superpositions of a flow of interacting bosons in a one-dimensional ring. The calculations have been performed via an exact diagonalisation method (see Sec. 2.6.1). Therefore, the rescaling method is suitable to improve the calculations, and helps to correctly interpret the results. In this section we only briefly summarise the main aspects of the work carried out and refer the reader to our publication in Ref. [84] for a more detailed discussion.

A.1 Motivation

Generating robust quantum superpositions of macroscopically distinct states can help to enhance precision measurements [154] as well as improve our understanding of quantum mechanics [155]. Previously, it has been shown that so-called *NOON* states create a superposition between two many-body states $|N, 0\rangle$ and $|0, N\rangle$, where the numbers in the ket denote the occupation number of the accessible single-particle modes (i.e. spin states, eigenmodes ...). However, *NOON* states are fragile and therefore limited to up to ten particles in current experiments [149]. On

APPENDIX A. ROBUST MESOSCOPIC SUPERPOSITION OF
 STRONGLY CORRELATED ULTRACOLD ATOMS
 - AN APPLICATION OF THE RESCALING METHOD

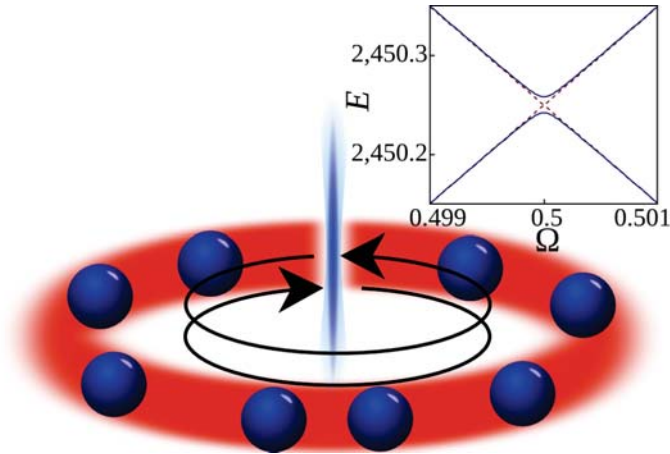


Figure A.1: N Strongly correlated bosons in a very tight ring-shaped trap. The rotating barrier is shown as a blue vertical beam. For $N = 99$ particles and no barrier the dashed lines in the inset show the energy as a function of the angular velocity Ω for the states with total angular momentum $K_1 = 0$ and $K_2 = N$. For a finite barrier the solid line reveals an avoided level crossing.

the other hand, it has been shown that a large macroscopic superposition of flux states in superconducting rings are much more robust [156, 157]. However, their microscopic nature is still debated [158–161]. Earlier works, that use ultracold gases for the creation of mesoscopic *NOON* states [28, 30, 162–165], suffer from decoherence effects [166] and therefore demand for small time scales in experiments [167, 168]. Hence, we proposed a scheme [84] to overcome this problem by creating robust superpositions due to strong interactions.

A.2 Results

Assume N bosons confined in a quasi-one-dimensional ring being stirred by a delta-like barrier. The Hamiltonian in dimensionless units (see Sec. 2.3) for this system in a co-rotating frame of reference is given by

$$H = \sum_{i=1}^N \left[\left(-i \frac{\partial}{\partial x_i} - \Omega \right) + b \delta(x_i) + g \sum_{i < j}^N \delta(x_i - x_j) \right] \quad (\text{A.1})$$

where b is the height of the stirring barrier and g is the interaction strength of the contact potential. The tangential stirring velocity is given by Ω , and therefore in the chosen frame the barrier is always stationary.

In the case of $b = 0$ the Hamiltonian in Eq. (A.1) can be solved analytically for all Ω via the Lieb-Liniger model introduced in Sec. 2.4.2. In particular, the solutions show an energy crossover at $\Omega = 0.5$ (see Fig. A.1). In contrast, an avoided energy level crossing appears for $b > 0$. This is due to the coupling of modes of different angular momentum. An adiabatic change of Ω of the first excited state from initially either $\Omega = 0$ or $\Omega = 1$ towards $\Omega = 0.5$ results in a superposition of the $K_1 = 0$ and $K_2 = N$ total angular momentum states with an equal probability of 50%. A sudden change to $\Omega = 0.5$, however, leads to coherent oscillations between both states.

Our simulations were performed for $N = 5$ particles and $M = 20$ single-particle functions, unless explicitly noted otherwise. Applying our rescaling method from Sec. 4.2 leads to errors of $\approx 3\%$ in the Tonks-Girardeau regime, improving results by a factor of 8 as compared to without rescaling.

Figure A.2 shows the energy gap ΔE between ground and first excited state at $\Omega = 0.5$. Three important regimes will now be discussed separately in the following.

Non-interacting atoms

In Fig. A.2 a dash on the left figure margin shows the energy gap ΔE at $\Omega = 0.5$ if there is no interaction between the particles. It is given by the energy that is needed to excite a single particle from its ground state to its first excited state. This can be calculated analytically for this system for different barrier heights. We find that the states with total momentum $K_1 = 0$ and $K_2 = N$ are degenerate for $b = 0$. However, this degeneracy is lifted for finite barrier heights due to coupling between states of different angular momentum. This leads to an energy gap, i.e. an avoided level crossing, at $\Omega = 0.5$. Hence, the probability $P(K)$ of the system having a total angular momentum K , as defined in Ref. [84], follows a binomial distribution [see Fig. A.2(a)]. This does not suit our purpose of finding a binary distribution where mainly the momentum states $K_1 = 0$ and $K_2 = N$ are highly

APPENDIX A. ROBUST MESOSCOPIC SUPERPOSITION OF
 STRONGLY CORRELATED ULTRACOLD ATOMS
 - AN APPLICATION OF THE RESCALING METHOD

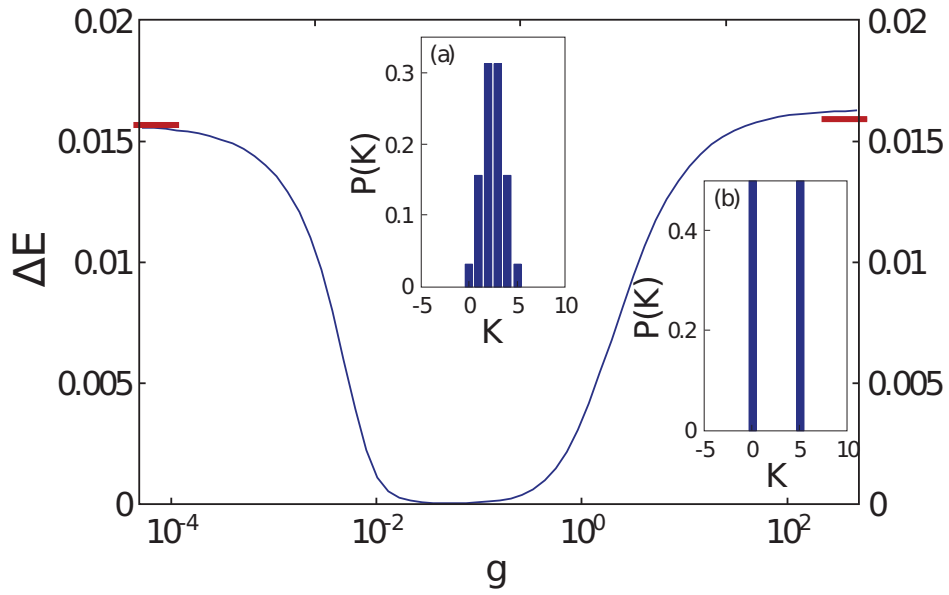


Figure A.2: Energy level splitting ΔE between the lowest two states at $\Omega = 0.5$ as a function of g after rescaling. These are results for $N = 5$ and $b = 0.008$. The dashes on the figure margins show the exact results from analytical models for $g = 0$ and $g = \infty$. The two insets represent their corresponding total angular momentum distributions K . Clearly, for $g \rightarrow \infty$ the binomial distribution from the non-interacting case (a) turns into a binary distribution (b), i.e. a superposition of $K_1 = 0$ and $K_2 = 5$.

probable.

Tonks-Girardeau regime (TG)

At the other extreme, the TG regime (see Sec. 2.4.1) of strong interactions differs dramatically to the previous case. The interaction removes all ground-state degeneracies except for $K_1 = 0$ and $K_2 = N$. Figure A.2(b) clearly shows a binary distribution of two total angular momentum states. However, for both, the $K_1 = 0$ and the $K_2 = N$ state, we find that their single-particle momentum distributions are spread out and have a significant overlap. Therefore, the superposition is much more robust to particle detection which is equivalent to the loss of a particle. This is because it is not clear which state the removed particle initially occupied. This improves the robustness of the superposition as we will show in App. A.3.

NOON state

The minimum of the curve in Fig. A.2 can be found at $g \approx 0.1$. This is a particularly interesting regime where the ground state takes the form similar to $|N, 0\rangle + |0, N\rangle$. This is a superposition of each particle having an angular momentum of $k = 1$ and an angular momentum of $k = 0$. The energy gap is very small and decreases faster than exponentially with particle number. This causes problems for its experimental realisation because long coherence times are required to form the state [10]. Therefore, a more convenient way is to create a robust superposition in the TG regime and then adiabatically change the interaction to create the *NOON* state.

A.3 Particle loss

The quality of a superposition can be measured with the normalised quantity $Q = 4P(K_1)P(K_2)$. The dashed line in Fig. A.3 shows Q as a function of the interaction strength g . We find a critical interaction at around $g = 0.1$, above which the superposition becomes nearly perfect, i.e. $Q \approx 1$, and where the distribution of total momentum states does not change anymore.

APPENDIX A. ROBUST MESOSCOPIC SUPERPOSITION OF STRONGLY CORRELATED ULTRACOLD ATOMS - AN APPLICATION OF THE RESCALING METHOD

In typical experiments, however, there are particle losses from the trap due to collisions with other particles or interactions with a thermal cloud. This can be modelled as a particle detection mechanism, which gives the most destructive form of loss. To quantify the effect, we define a superposition quality after the loss of one particle $\bar{Q}^{[-1]} = \sum_k Q_k^{[-1]} n_k / N$ [84]. Here, $Q_k^{[-1]} = 4P^{[-1]}(-k)P^{[-1]}(N - k)$ is the quality after the loss of a single particle with momentum k , and n_k is the probability to find an atom with momentum k . The solid line in Fig. A.3 shows $\bar{Q}^{[-1]}$ as a function of g . For the *NOON* state regime at $g \approx 0.1$ the superposition vanishes after particle loss, while in the strongly interacting regime the superposition quality is still approximately one. The inset of Fig. A.3 presents $\bar{Q}^{[-1]}$ for varying particle numbers in the TG regime. It shows that the robustness is increased for large particle numbers because the single-particle momentum distribution becomes more spread out. This means that the probabilities that a detected particle contributed to the total angular momentum states K_1 or K_2 are of the same order of magnitude. This is in contrast to the *NOON* state, where it is clear that the angular momentum of a detected particle automatically tells you the total angular momentum state it contributed to.

A.4 Summary

We investigated bosons in a one-dimensional ring being stirred by a thin barrier. We have shown that there is a critical interaction, above which the state of the system is a superposition of two total angular momentum states. However, after particle losses *NOON* states get destroyed because of their fragile nature. The TG regime, on the other hand, can maintain the superposition because the single-particle momentum distribution is much more spread out. This is important for experiments and might lead to new research for creating superposition states in the strongly interaction regime. For a more detailed discussion we refer the reader to our publication Ref. [84].

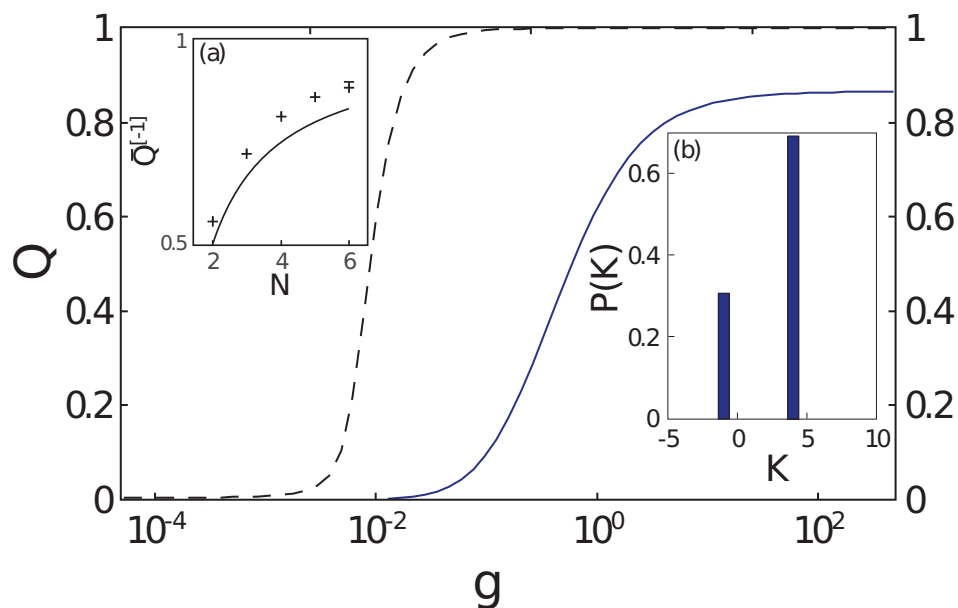


Figure A.3: The quality Q of the superposition before (dashed line) and after (solid line) the loss of one particle. The upper left inset shows the quality after particle loss as a function of total particle number. For $N = 6$ only results for $M \leq 14$ were accessible, and therefore an extrapolation to $M = 20$ is indicated by a dashed line. The lower right inset gives the distribution of total angular momentum states after removal of a particle with momentum $k = 1$. Particle loss does not destroy the binary distribution, it only shifts amplitudes.

APPENDIX A. ROBUST MESOSCOPIC SUPERPOSITION OF
STRONGLY CORRELATED ULTRACOLD ATOMS
- AN APPLICATION OF THE RESCALING METHOD

B

Numerical methods

B.1 Wave propagation

There are different ways to numerically implement the propagation of a wave function $\psi(x, t)$ in one spatial dimension over time. In this section we only cover two of them that are relevant for this thesis. In the following, we focus on solving the nonlinear Gross-Pitaevskii (GP) equation given by

$$\begin{aligned} \frac{\partial}{\partial t} \psi(x, t) &= F(x, t, \psi(x, t)) \psi(x, t). \\ F(x, t, \psi(x, t)) &= -i \left[-\frac{1}{2} \frac{\partial^2}{\partial x^2} + V(x, t) + U |\psi(x, t)|^2 \right] \end{aligned} \quad (\text{B.1})$$

Numerically, the spatial axis and time are represented on a discrete grid. This leads to the following spatial and temporal replacements:

$$\begin{aligned} x &\rightarrow x_i \quad \text{with } dx = x_{i+1} - x_i, \quad i = 1 \dots N_g, \\ t &\rightarrow t_k \quad \text{with } dt = t_{k+1} - t_k, \quad k \in \mathbb{N}_0 \end{aligned}$$

We introduced x_0 and x_{N_g} , the positions of the left and right wall of the box for a grid of N_g points, and define t_0 as the initial time. The system's boundaries are usually chosen to be infinitely high hard walls or periodic, i.e. $\psi(x_0, t) = \psi(x_{N_g}, t)$.

The first derivative of the wave function over time can be written as

APPENDIX B. NUMERICAL METHODS

$$\frac{\partial}{\partial t}\psi(x, t) \rightarrow \frac{\psi_{i,k+1} - \psi_{i,k}}{dt},$$

where $\psi_{i,k} = \psi(x_i, t_k)$. The most commonly used propagation method is the Runge-Kutta (RK) method [169]. The first order RK method, also known as the Euler method, performs the following update

$$\psi_{i,k+1} = \psi_{i,k} + F(x_i, t_k, \psi_{i,k}).$$

The truncation error is proportional to dt^2 . The midpoint approach, also known as second order RK, already improves the accuracy to an error of dt^3 . It is given by

$$\begin{aligned} a_1 &= F(x_i, t_k, \psi_{i,k}), \\ a_2 &= F(x_i, t_k + \frac{dt}{2}, \psi_{i,k} + \frac{1}{2}a_1), \\ \psi_{i,k+1} &= \psi_{i,k} + a_2. \end{aligned}$$

This scheme can be extended to higher orders. The error for the n th order Runge Kutta is proportional to $\mathcal{O}(dt^{n+1})$. In addition, more advanced algorithms have been developed that include adaptive time steps. There, an additional correction is calculated and from this, an estimate of the error in the propagation can be obtained. A predefined step error chosen by the user controls the length of next time step. For the propagations with MCTDH in chapter 4, a built-in adaptive 8th order RK method has been used. Qiwib implements the *ode78* routine from the octave-forge *odepkg* package [170]. It is a variation of the Runge-Kutta method, the so-called the Runge-Kutta-Fehlberg method, which is an adaptive 7th-order method with an 8th-order estimate that gives a total accuracy proportional to $\mathcal{O}(dt^9)$.

Another popular method is the implicit Crank-Nicholson scheme used for the GP simulations in chapter 3. An implicit method calculates the next time step by including a “predicted” wave function while in so-called explicit methods, e.g. Runge-Kutta methods, the new wave-function is calculated with just the inform-

ation from the previous time step:

$$\begin{aligned}\psi_{i,k+1} &= \psi_{i,k} + F(x_i, t_k, \psi_{i,k}) \quad \text{explicit,} \\ \psi_{i,k+1} &= \psi_{i,k} + F(x_i, t_k, \psi_{i,k}, \tilde{\psi}_{i,k+1}) \quad \text{implicit.}\end{aligned}\tag{B.2}$$

The prediction $\tilde{\psi}$ can be obtained by an explicit method which does not necessarily have to be very accurate. Implicit methods are usually more stable, i.e. the errors are bounded for stiff problems, which are cases where an explicit method would need infinitely small time steps. My experience with implicit methods is generally good as the results are typically of high accuracy. In the Crank-Nicholson scheme the idea is to rewrite Eq. (B.2) in a matrix and vector notation. We define the vector $\vec{\psi}_k = (\psi_{k,0} \dots \psi_{k,N_g})$ and a Hamiltonian matrix $\mathbf{H}_k(\vec{\psi}_k)$ so that Eq. (B.2) can be written as

$$\begin{aligned}\vec{\psi}_{k+1} &= \vec{\psi}_k + \frac{1}{2} \left[\mathbf{H}_{k+1}(\vec{\psi}_{k+1})\vec{\psi}_{k+1} + \mathbf{H}_k(\vec{\psi}_k)\vec{\psi}_k \right] \\ \Rightarrow \left[\mathbf{1} - \frac{1}{2}\mathbf{H}_{k+1}(\vec{\psi}_{k+1}) \right] \vec{\psi}_{k+1} &= \left[\mathbf{1} + \frac{1}{2}\mathbf{H}_k(\vec{\psi}_k) \right] \vec{\psi}_k \\ \Rightarrow \vec{\psi}_{k+1} &= \frac{\mathbf{1} + \frac{1}{2}\mathbf{H}_k(\vec{\psi}_k)}{\mathbf{1} - \frac{1}{2}\mathbf{H}_{k+1}(\vec{\psi}_{k+1})} \vec{\psi}_k.\end{aligned}$$

Because of the appearance of $\vec{\psi}_{k+1}$ on the right-hand side, representing the non-linear term in the Gross-Pitaevskii equation, we perform two calculations for each time step. The first calculation, the so-called predictor step, gives a “prediction” for the wave function:

$$\tilde{\vec{\psi}}_{k+1} = \frac{\mathbf{1} + \frac{1}{2}\mathbf{H}_k(\vec{\psi}_k)}{\mathbf{1} - \frac{1}{2}\mathbf{H}_{k+1}(\tilde{\vec{\psi}}_k)} \vec{\psi}_k.$$

This is followed by the “corrector” step given by

$$\vec{\psi}_{k+1} = \frac{\mathbf{1} + \frac{1}{2}\mathbf{H}_k(\vec{\psi}_k)}{\mathbf{1} - \frac{1}{2}\mathbf{H}_{k+1}(\tilde{\vec{\psi}}_{k+1})} \vec{\psi}_k$$

to obtain the final wave function $\vec{\psi}_{k+1}$. For the simulations in chapter 3 we used a fixed time step of 0.01. However, convergence has been verified by using smaller

time steps and by comparison with a Cash-Karp method [171], which is a variant of an adaptive 4th- to 5th-order RK algorithm.

B.2 Imaginary time propagation

In order to simulate travelling solitons one has to create an initial soliton first. This can either be done by using the analytical formula in Eq. (2.30) or by a method called imaginary-time propagation [145]. The latter is an established method to find ground-state wave-functions that minimise the total energy for an arbitrary system. The idea behind this is the following: Assume we can expand a random wave function in terms of eigenfunctions of the system

$$\psi(x, t) = \sum_{i=0}^{\infty} \phi_i(x) e^{-iE_i t} \quad (\text{B.3})$$

where E_i determines the energy of the i th function, and $E_0 < E_1 < \dots < E_{\infty}$. By switching to imaginary time with $\tau = it$ we obtain $\psi(x, \tau) = \sum_{i=0}^{\infty} \phi_i(x) e^{-E_i \tau}$. Treating τ as real we can rewrite Eq. B.1 and find

$$-\frac{\partial}{\partial \tau} \psi(x, \tau) = F[x, \tau, \psi(x, \tau)] \psi(x, \tau). \quad (\text{B.4})$$

Forward propagation with respect to τ will result in an exponential decay of all terms in the expansion Eq. (B.4). However, the term $\phi_0 \exp(-E_0 \tau)$ becomes dominant for $\tau \rightarrow \infty$. Subsequently, the wave function will converge to the eigenfunction with the smallest energy E_0 . However, this scheme does not conserve the normalisation of ψ , and therefore the wave function has to be normalised after each time step. For smooth functions and potentials this typically gives accurate results. However, for more complicated systems this convergence scheme might end up in a local minimum. For example, if the state energies are nearly degenerate, the scheme might converge to a higher lying state. Therefore, imaginary time propagation has to be applied with care.

B.3 Numerical implementation of Qiwib

B.3.1 Single-particle functions

Forward propagation of the single-particle function is done via a built-in Runge-Kutta scheme as mentioned in App. B.1. However, compared to the Gross-Pitaevskii equation, the full MCTDHB equations (2.44) are more complicated to solve. For instance, they include a projector P to ensure orthonormalisation of the single-particle functions. We used a scheme proposed in Ref. [126] where the usual projector

$$P = \sum_i |\phi_i\rangle\langle\phi_i|$$

is being replaced by

$$P = \sum_{i,j} |\phi_i\rangle O^{-1}\langle\phi_j|$$

with $O_{kl} = \langle\psi_k|\psi_l\rangle$. This improves the orthonormalisation significantly and reduces the errors in the whole propagation scheme by giving different weight to the terms in the sum.

B.3.2 Propagation of prefactor \vec{C}

The propagation of the \vec{C} -vector according to Eqs. (2.44) can be performed with different methods. Similar to the problem in App. B.1, the Runge-Kutta method can be used. This gives accurate results but is numerically slow and does not preserve the normalisation $\sum_i C_{\vec{n}_i} = 1$. However, the equation of motion for \vec{C} is linear. Due to this and for practical reasons, an Arnoldi/Lanczos algorithm [89, 172, 173] is much more efficient and will be introduced now. Assume an initial vector $\vec{A}_0 = \vec{C}(t)$. To obtain $\vec{C}(t + dt)$ for a time step dt , a set of vectors \vec{A}_i with $i = 1 \dots N_K$ is created recursively. These vectors span a so-called Krylov space where the projected Hamiltonian $\mathbf{H}_{\vec{C},\mathbf{P}} = \mathbf{P}\mathbf{H}_{\vec{C},\mathbf{P}}\mathbf{P}$ is tridiagonal. \mathbf{P} is the

APPENDIX B. NUMERICAL METHODS

projector onto this space. The recursion is given by

$$\begin{aligned}\beta_{n+1} \cdot \vec{A}_{n+1} &= (\mathbf{H}_{\vec{C}, \mathbf{P}} - \alpha_n) \cdot \vec{A}_n - \beta_n \cdot \vec{A}_{n-1}, \\ \alpha_n &= \langle \vec{A}_n | \mathbf{H}_{\vec{C}, \mathbf{P}} | \vec{A}_n \rangle \\ \vec{A}_{-1} &= 0.\end{aligned}$$

The resulting tridiagonal matrix \mathbf{M} is given by

$$M_{nm} = \begin{cases} \alpha_n & \text{if } n = m \\ \beta_n & \text{if } n = m + 1 \text{ or } n = m - 1 \\ 0 & \text{else.} \end{cases}$$

It can easily be diagonalised by $M_{nm} = \langle C_n | \mathbf{H}_{\vec{C}, \mathbf{P}} | C_m \rangle = \sum_k V_{nk}^\dagger E_k V_{km}$. The columns of $\mathbf{V} = \{V_{nk}\}$ contain the eigenvectors of \mathbf{M} and E_k are its eigenvalues. The resulting time evolution

$$\vec{C}(t + dt) = \sum_{kj} V_{kj} e^{-iE_j dt} (\mathbf{V}^{-1})_{j0} \vec{A}_k$$

is unitary and for our problem much faster than an ordinary RK method. The size of the Krylov space N_K is determined at every time step during the recursion via an error estimate given by

$$\epsilon \approx \frac{\beta_0 \dots \beta_{N_K-1}}{N_K!} dt^{N_K}.$$

In QiviB a maximal value of N_K and an error estimate are defined in the input file. This way the size of the Krylov space, and therefore the speed of the simulations, can be controlled. An error message is displayed if the accuracy can not be reached with the given N_K .

B.3.3 Improved relaxation

It is possible to calculate the ground state in QiviB by imaginary time propagation of both the single-particle functions and the \vec{C} -vector. A more sophisticated

B.3. NUMERICAL IMPLEMENTATION OF QIWIB

method is given by the so-called *improved relaxation* scheme [90, 146]. It is not only faster but also allows for relaxation into excited states.

The scheme works as follows: The single-particle functions are still relaxed via imaginary-time propagation. However, for the \vec{C} -vector we solve the eigenvalue equation

$$\mathbf{H}_{\vec{C}}\vec{C} = E_i\vec{C}.$$

Depending on the state that we want to relax to, we have to choose a suitable initial eigenvector and continue the improved relaxation iteratively. This way the single-particle functions are forced to converge to the state of interest as well. However, the wrong choice of the initial eigenvector or numerical inaccuracies may lead to a convergence into the wrong eigenstate [90]. In particular, this is the case for nearly degenerate states. However, for the systems studied in this thesis these problems do not appear.

B.3.4 Implementation of the whole propagation scheme

Now we consider again the real-time propagation. The two MCTDHB equations of motion (2.44) are coupled and therefore have to be integrated simultaneously. In order to increase the accuracy, a propagation scheme has been proposed [92, 126] that is implicit and calculates errors for an adaptive mean-field time step. Starting with initial values at $t = t_0$ for the observables in Eqs. (2.39) and (2.44), the propagation runs for an initial time step Δt , which is referred to as the mean-field time step. The propagation scheme is now split into several steps:

1. Use $h_{kq}(t_0)$ and $W_{ksql}(t_0)$ to propagate $\vec{C}(t_0) \rightarrow \vec{C}(t_0 + \Delta t/2)$
 \rightarrow Calculate $\rho_{kq}(t_0 + \Delta t/2)$ and $\rho_{ksql}(t_0 + \Delta t/2)$.
2. Use $\rho_{kq}(t_0 + \Delta t/2)$ and $\rho_{ksql}(t_0 + \Delta t/2)$ to propagate $\phi_n(x, t_0) \rightarrow \phi_n(x, t_0 + \Delta t/2)$.
3. Use $\rho_{kq}(t_0)$ and $\rho_{ksql}(t_0)$ to propagate $\phi_n(x, t_0) \rightarrow \tilde{\phi}_n(x, t_0 + \Delta t/2)$.
4. Use $\rho_{kq}(t_0 + \Delta t/2)$ and $\rho_{ksql}(t_0 + \Delta t/2)$ to propagate $\phi_n(x, t_0 + \Delta t/2) \rightarrow \phi_n(x, t_0 + \Delta t)$
 \rightarrow Calculate $h_{kq}(t_0 + \Delta t)$ and $W_{ksql}(t_0 + \Delta t)$.

APPENDIX B. NUMERICAL METHODS

5. Use $h_{kq}(t_0 + \Delta t)$ and $W_{ksql}(t_0 + \Delta t)$ to propagate $\vec{C}(t_0 + \Delta t/2) \rightarrow \vec{C}(t_0 + \Delta t)$
 \rightarrow Calculate $\rho_{kq}(t_0 + \Delta t)$ and $\rho_{ksql}(t_0 + \Delta t)$.
6. Use $h_{kq}(t_0 + \Delta t)$ and $W_{ksql}(t_0 + \Delta t)$ to back-propagate $\vec{C}(t_0 + \Delta t/2) \rightarrow \tilde{\vec{C}}(t_0)$.

The differences $C(t_0) - \tilde{\vec{C}}(t_0)$ and $\phi_n(t_0 + \Delta t/2) - \tilde{\phi}_n(t_0 + \Delta t/2)$ are used to estimate the error ϵ for the propagation and to adjust the mean-field time step dynamically:

$$\begin{aligned} \Delta t_{\text{new}} &= B \Delta t_{\text{old}} \sqrt[4]{\epsilon/\delta}, \\ \epsilon &= \|\vec{C}(t_0) - \tilde{\vec{C}}(t_0)\| + |\text{tr}(\mathbf{O}\boldsymbol{\rho}^T)|, \\ O_{kl} &= \langle \Delta\phi_k | \Delta\phi_l \rangle, \quad \Delta\phi_n = \tilde{\phi}_n(t_0 + \Delta t/2) - \phi_n(t_0 + \Delta t/2). \end{aligned}$$

Here $\boldsymbol{\rho} = \{\rho_{kq}\}$ and δ is a predefined error. If $\epsilon < \delta$, the new values are accepted. Otherwise they are rejected, and a new calculation is done with all the initial values at $t = t_0$ but for a smaller time step. In order to avoid too many rejections we introduced a prefactor B . For $\epsilon < \delta$ we set $B = 0.8$, and $B = 0.5$ otherwise. This scheme has been proven to be stable and therefore suitable for the work presented in this thesis.

This propagation scheme can also be applied to the *improved relaxation* scheme from App. B.3.3. However, only the previously defined steps 1-3 are required now. Furthermore, in step 1 the \vec{C} -vector is now obtained from a diagonalisation of $\mathbf{H}_{\vec{C}}$. As described in App. B.3.3, the correct eigenvector is taken as the new \vec{C} -vector. Here, only the difference $\phi_n(t_0 + \Delta t/2) - \tilde{\phi}_n(t_0 + \Delta t/2)$ accounts for the error estimate.

B.3.5 Calculation of $\mathbf{H}_{\vec{C}}$ and the mean fields ρ_{kq} and ρ_{ksql}

The numerical implementation of the calculations of the matrix $\mathbf{H}_{\vec{C}}$ as well as the mean-fields ρ_{kq} and ρ_{ksql} from Eqs. (2.41) and (2.42) is straightforward. QiwiB follows Ref. [92]. Essentially, the main numerical work is related to the calculation of

$$\begin{aligned} H_{ijkq} &= \langle \vec{n}_i | b_k^\dagger b_q | \vec{n}_j \rangle, \\ H_{ijksql} &= \langle \vec{n}_i | b_k^\dagger b_s^\dagger b_q b_l | \vec{n}_j \rangle \end{aligned}$$

B.3. NUMERICAL IMPLEMENTATION OF QIWIB

with $|\vec{n}_x\rangle = |n_{x,1}, n_{x,2}, \dots, n_{x,M}\rangle$. However, while the computation of H_{ijkq} is numerically fast, we found that determining H_{ijksql} is very CPU demanding, in particular for a large number of single-particle functions M . The fact that these variables have to be recalculated every time-step makes the whole algorithm unnecessarily slow. In order to overcome this problem we developed a method that reduces the computational amount for each time step by creating an additional matrix dH_{mn} . It contains all the necessary information about all non-zero elements of H_{ijksql} . The elements of each row contain i and j for the states \vec{n}_i and \vec{n}_j and all indices $y = 1 \dots M$, ordered with respect to the magnitude of $n_{i,y} - n_{j,y}$. In addition, dH_{mn} includes a number that represents the symmetry of H_{ijksql} , for example whether any of the k, s, q, l are equal. The matrix dH_{mn} can be calculated separately and saved on hard disk. Therefore, it can be reused for different simulations. This method allows to do simulations for $N = 120$ and $M = 4$ in the same amount of time as simulations for $N = 40$ and $M = 4$ when calculating H_{ijksql} at each time step. However, the amount of memory needed increases with the size of dH_{mn} as the size of the Hilbert space increases dramatically for increasing M and N . Therefore, Qiwib simulations on a typical desktop machine with 4-8 GB of RAM are currently limited to $N \approx 150$ and $M = 4$.

B.3.6 Transformation to natural orbital basis

The natural orbital (NO) basis for MCTDHB is defined by Eq. 2.45

$$\rho(x, y, t) = \langle \Psi^\dagger(x) \Psi(y) \rangle = \sum_{k,q=1}^M \rho_{kq} \phi_k^*(x_2) \phi_q(x_1) = \sum_{k=1}^M \rho_k [\phi_k^{NO}(x)]^* \phi_k^{NO}(y).$$

where ϕ_i are the single-particle functions. Numerically, the natural orbitals ϕ_j^{NO} are given by the eigenvectors of the discretised one-body density matrix $\rho(x, y, t)$. Furthermore, the eigenvalues ρ_k represent the population of their respective natural orbitals. Hence, calculation of these quantities is trivial. However, it is numerically very demanding to transform the \vec{C} vector in the single-particle basis to the \vec{C}^{NO} vector in the NO basis. To our knowledge, this is only feasible for two natural orbitals. Consider a total many-body wave function $|\psi\rangle$ with the \vec{C}^{NO} vector

APPENDIX B. NUMERICAL METHODS

given by

$${}^{NO}\langle\mu|\psi\rangle = {}^{NO}\langle\mu|\sum_{\nu=0}^N C_{\nu}^{NO}|\nu\rangle^{NO} = C_{\mu}^{NO}.$$

$|\psi\rangle$ can be expanded as given by Eq. 2.40. For $M = 2$ the transformation of the operators \hat{b}_i^{\dagger} to the corresponding operators \hat{d}_i^{\dagger} in the natural orbital basis is given by

$$\begin{pmatrix} \hat{b}_1^{\dagger} \\ \hat{b}_2^{\dagger} \end{pmatrix} = \mathbf{T} \begin{pmatrix} \hat{d}_1^{\dagger} \\ \hat{d}_2^{\dagger} \end{pmatrix} = \begin{pmatrix} t_{11} & t_{21} \\ t_{12} & t_{22} \end{pmatrix} \begin{pmatrix} \hat{d}_1^{\dagger} \\ \hat{d}_2^{\dagger} \end{pmatrix}.$$

The elements of matrix \mathbf{T} are given by the eigenvectors of ρ_{kq} . Using Eq. 2.40, this leads to the representation of $|\psi\rangle$ in the natural orbital basis given by

$$\begin{aligned} |\psi\rangle &= \sum_{n=0}^N \frac{C_n}{\sqrt{n!}\sqrt{N-n!}} \sum_{k=0}^n \binom{n}{k} (t_{11}\hat{d}_1^{\dagger})^k (t_{21}\hat{d}_2^{\dagger})^{n-k} \\ &\quad \times \sum_{l=0}^{N-n} \binom{N-n}{l} (t_{12}\hat{d}_1^{\dagger})^l (t_{22}\hat{d}_2^{\dagger})^{N-n-l} |vac\rangle. \end{aligned}$$

From this, the μ th element of the \vec{C}^{NO} vector can be calculated as

$$\begin{aligned} C_{\mu}^{NO} &= {}^{NO}\langle\mu|\psi\rangle \\ &= \sum_{k=0}^{\mu} \sum_{n=k}^{N-\mu+k} \sqrt{\binom{N}{n} / \binom{N}{\mu} \binom{N}{n} \binom{N-n}{\mu-k}} t_{11}^{n-k} t_{21}^k t_{12}^{N-n-\mu+k} t_{22}^{\mu-k} C_n. \end{aligned}$$

This sum causes numerical problems because some terms are very small and others very big, with tens and hundreds of orders of magnitude difference. Therefore, the resulting C^{NO} vector becomes incorrect for very large numbers of particles N . In particular, on our systems we found that the results for up to $N \approx 80$ are still reliable.



Qiwib - Influence of \mathbf{N} and \mathbf{M} on CPU times

Analogous to Sec. 4.1, we first present CPU times for Qiwib calculations by varying the number of particles N and the number of single-particle functions M . Consider a box of length $L_{Box} = 80$ with a soliton initially being placed at $x = -7.5$. The inter-particle interaction strength was chosen to be $g = 2/N$. We measured the CPU time it takes to simulate 50 time units, during which the soliton travels to the right with a velocity of $v = 0.3$.

Varying number of particles

It is expected that the CPU time t_{CPU} scales proportionally to the size of the Hilbert space \mathcal{H} , i.e. the number of configurations, which is given by

$$S_{\mathcal{H}}(N, M) = \binom{N + M - 1}{N} = \frac{(N + M - 1)!}{N!(M - 1)!}. \quad (\text{C.1})$$

Fig. C.1 shows results obtained from numerical calculations performed for $M = 4$ on a numerical grid with $N_g = 2001$ grid points inside a box from $x = -40$ to $x = 40$. The findings agree very well with Eq. (C.1). A constant contribution to the total CPU time can be accounted for by the propagation of the single-particle wave functions that only depend on M but not N . In addition, a considerably small amount of time in Qiwib is spent for performing general tasks, for example copying and saving data. Furthermore, the nonlinear increase in computation time clearly

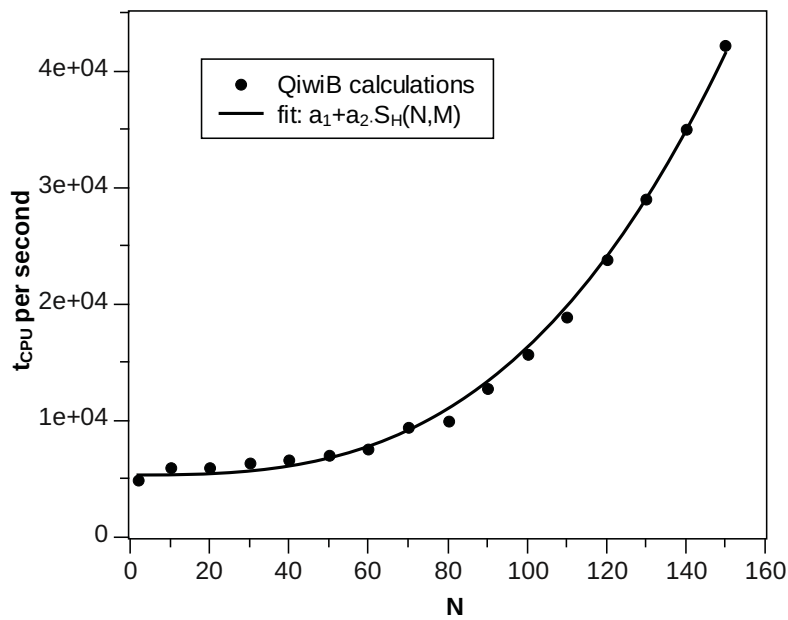


Figure C.1: CPU time as a function of the number of particles N . The fit parameters are $a_1 = 5339$ and $a_2 = 0.08237$. The CPU time clearly increases with the size of the Hilbert space. The constant contribution is mainly related to the propagation of the single-particle function, a calculation that does not depend on N .

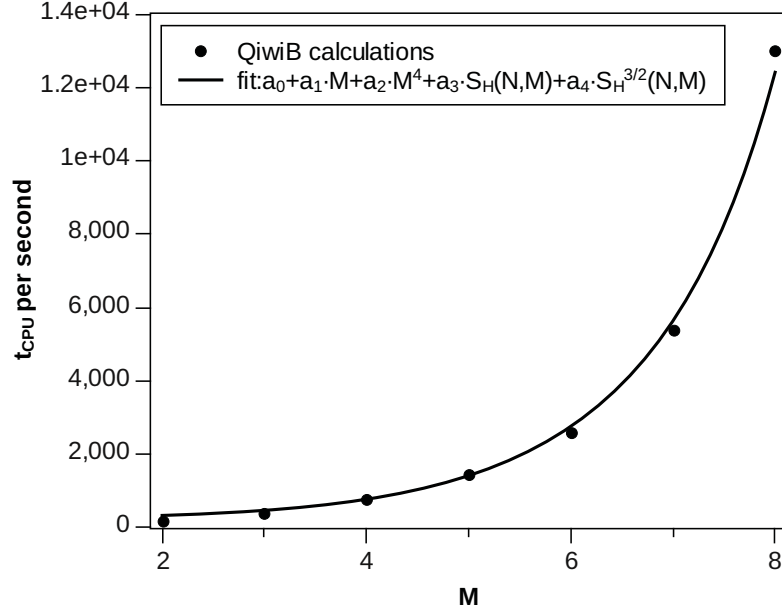


Figure C.2: CPU time as a function of the number of single-particle functions M . The fit parameters are $a_0 = 219.8$, $a_1 = 37.29$, $a_2 = 1.455$, $a_3 = 0.05405$ and $a_4 = 0.002264$. The different terms in the fit function were determined from CPU times for different parts of the Qiwib program, i.e. propagation of single-particle functions (a_1 and a_2), propagation of the \vec{C} vector (a_3) and calculation of \mathbf{H}_C and ρ_{ksql} (a_4). A constant time a_0 is spent on other tasks, e.g. saving data.

gives an upper limit for the numerically feasible number of particles. Indeed, for the calculations presented in chapter 5, it was not feasible to go beyond $N \lesssim 150$ particles for $M = 4$. Of course, smaller values of M allow for up to $N = 1000$ ($M = 3$) or $N = 10000$ ($M = 2$) particles.

Varying number of single-particle functions

Considering a very small number of particles of $N = 10$ results in a much reduced Hilbert space, even for larger numbers of single-particle functions M . However, to ensure that the propagation of the single-particle functions to be numerically feasible for up to $M = 8$, the number of spatial grid points was now reduced to $N_g = 881$. Fig. C.2 shows the resulting correlation between CPU times and M .

APPENDIX C. QIWIB - INFLUENCE OF N AND M ON CPU TIMES

The fitted graph contains different terms which have been obtained separately from CPU times for different parts of the Qiwib program. For instance, one term is shown to be proportional to $\binom{N+M-1}{N}^{3/2}$. This is related to the calculation of ρ_{ksql} and $\mathbf{H}_{\vec{C}}$ (see App. B.3.5 for the method used in Qiwib). Moreover, a contribution $\propto S_{\mathcal{H}}(N, M) = \binom{N+M-1}{N}$ is related to the propagation of the \vec{C} vector. The linear and quartic dependencies with respect to M originate from the propagation of the single-particle functions and the calculation of the nonlinear term in the second line of Eq. 2.44. For the case of $M \leq 8$, the contributions $\propto M$ and $\propto M^4$ to the total CPU time are largest. However, due to the exponential increase of $S_{\mathcal{H}}(N, M)$, this relation is interchanged for $M \geq 9$. We also note that a small amount of time is spent in Qiwib performing trivial tasks, e.g. saving data.

Therefore, the CPU times scale worse with respect to M compared to N . This is different to MCTDH, where simulations are usually restricted to $N \sim \mathcal{O}(1)$ and $N < M$. MCTDHB/Qiwib, however, is capable of performing calculations with few single-particle functions but for large N , i.e. $N \gg \mathcal{O}(1)$ and $N \gg M$.



The QiwiB program package

D.1 Background

QiwiB is an open source project being developed in our group to integrate the MCTDHB equations (2.44) for bosonic systems. The current version can be downloaded from Ref. [96]. So far it was successfully tested and run on *GNU Linux* and *MacOSX*. It is mainly written in *GNU Octave* [170, 174] which is an open source high-level programming language. Its syntax is highly compatible with the commercial *MATLAB*. The reasons why we did not choose to implement the program in a faster low-level language, such as C/C++ or Fortran, are manifold:

- First of all, *Octave/Matlab* code is much easier to write and to maintain. The code itself is much more readable as well, which might result in new collaborators joining the development of QiwiB. Furthermore, human readable error messages assist in the debugging process, which is a general feature of high-level languages and greatly helps in the debugging process.
- *Octave* includes many useful built-in functions that have been thoroughly tested by the *Octave* community. Amongst many other functions, *Octave* includes several integration methods (e.g. Runge-Kutta and Adams-Bashfourth) as well as eigenvalue problem solvers. Having these readily available reduced the coding effort for *QiwiB* significantly. Often, those functions are just templates for widely used and established numerical libraries, i.e. *LAPACK*, *BLAS* or *ATLAS*. These libraries already include optimised routines for

APPENDIX D. THE QIWIB PROGRAM PACKAGE

many problems and *Octave* takes advantage of that knowledge.

- *Octave* provides several features for user input and output, including plotting functions that are independent from the operating system. It provides tools that allow the development of a user-friendly interface for *Qiwib*.
- We note that programs written in *Octave/Matlab* have the reputation of being slow and wasting a lot of memory. However, for the problems presented in this thesis, and *Qiwib* in its current state, this is not a critical issue. First of all, there are only very few computationally demanding parts in the *Qiwib* program. In addition, *Octave* provides an API to use C/C++ code for time-critical parts of the code. In *Qiwib*, especially for problems involving a large Hilbert space, most of the CPU time is spent inside those C/C++ functions. An estimate of the memory consumption shows that it could roughly be halved by using purely C/C++ instead of *Octave*. However, this would not be very helpful considering the exponential increase of the Hilbert space for increasing number of particles or single-particle functions. Therefore, not much would be gained, at least in the current state of *Qiwib*.

The main numerical implementations are presented in the appendix B.3.

D.2 Summary of key features

At the time writing this thesis, *Qiwib* was developed to solve many-boson systems in one dimension. Their inter-particle interaction, approximated by a contact interaction, was implemented into *Qiwib* via a delta potential.

For users

- *Qiwib* solves one dimensional systems.
- *Qiwib* is best suited for weak interactions but can also handle strong interactions.
- Time-dependent as well as ground- and excited-state calculations are possible.

D.2. SUMMARY OF KEY FEATURES

- QiviB is capable of calculating hundreds and even thousands of bosons (e.g. 120 particles and 4 single-particle functions or 1000 particles and 3 single-particle functions).
- The QiviB program package includes command line scripts to install and run QiviB as well as to analyse data (including creating images and animated films).
- All scripts are described in a comprehensive html manual that is included in QiviB. The manual also includes installation instructions and information about writing input files and output files generated by QiviB.
- The input file specifies all parameters for a calculation. The creation of those files was implemented to be straightforward and simple, even for non-programmers. In addition, *Octave* commands can be used inside the input file in order to define more sophisticated potentials, wave-functions and so on.
- QiviB implements several numerical integrators to choose from, e.g. Runge-Kutta methods and the Lanczos integrator. It is possible to include different boundary conditions, complex absorbing boundaries and rotating frames.
- QiviB can be run in a batch mode and, therefore, is able to run on computer clusters.
- Parts of the program can be parallelised.
- QiviB and *GNU Octave* are both open source, and therefore no hidden costs are attached to the usage of this software.

For developers

- QiviB is an open source project released under the so-called MIT license.
- QiviB is written with *Octave*, a package of libraries and templates with its programming language being as close as possible to *MATLAB*. Therefore, the code is much easier to understand than any low-level language.

APPENDIX D. THE QIWIB PROGRAM PACKAGE

- Time-consuming functions were rewritten in C/C++ to increase the speed of the program significantly.

Planned extensions to Qiwib

- 2D and 3D systems.
- Improvements in the integrators, e.g. by finite-element methods.
- Other forms of inter-particle interactions.
- Parallelising larger parts of the code.
- And many more...

D.3 Examples

In this section two example calculations are presented to familiarise the reader with the usage of Qiwib. For installation instructions, we refer to the *README* file and the *html* documentation which are both included in the downloadable Qiwib package.

D.3.1 Particles in a well

We start with the simple problem of 20 particles confined in a one-dimensional harmonic well. First, an input file in the form of a text document, i.e. *well.inp*, is created. Included comments start with “%” and the font for new definitions is coloured blue. The first six lines of this file are shown below.

```
% well.inp  
  
pa.relaxation = 0; % relaxation process into the ground state  
pa.N=20; % 20 particles  
pa.M=3; % 3 single-particle functions  
pa.Ng=101; % numerical grid with 101 points  
pa.L=8; % box-boundary conditions with a box of length L  
pa.xpos0=-4; % position of the box's left wall  
:  
:
```

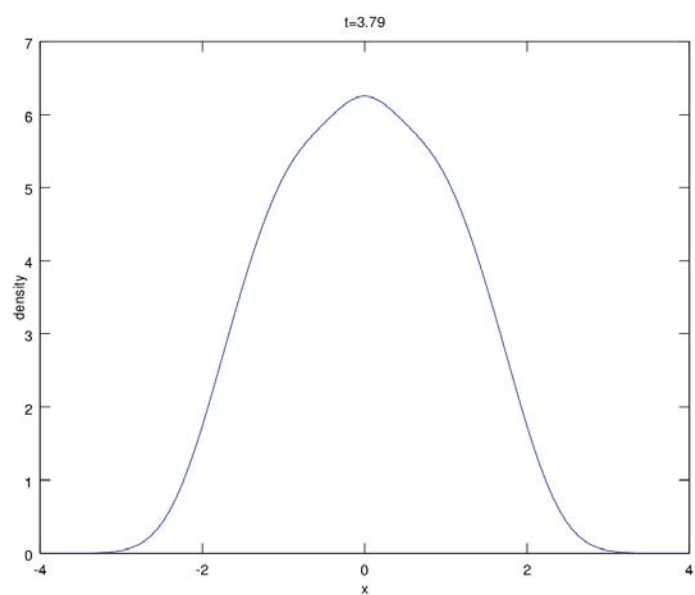


Figure D.1: Density plot for 20 particles confined in a harmonic well (see text) after being relaxed to the ground state. This picture is an exact copy of the image generated by one of the plotting tools that are integrated in QiviB.

APPENDIX D. THE QIWIB PROGRAM PACKAGE

The variables defined above represent the minimum amount of information needed to start a simulation. All variable definitions start with “*pa.*” and each definition should end with a semicolon. So far, the example file would initiate a relaxation into the ground state for 20 non-interacting particles in a box of length $L = 8$. The remaining lines are given by:

```
⋮
pa.dE_limit = 1E-6; % criterion on energy convergence to stop
pa.save_step = 0.01; % saves data every 0.01 time units
pa.save_options = [1,1,1,1,1]; % saves all data

function hamiltonian_t(t) % defines a Hamiltonian
mlock(); global pa
pa.V = ([pa.xpos0:pa.L/(pa.Ng-1):pa.xpos0+pa.L]').^2; % the harmonic well: V(x) = x^2
pa.g = 1.0; % the inter-particle interaction strength
endfunction
```

The first line ensures that the relaxation process stops once the energy is sufficiently converged. The next two lines regulate the storage of the output data, i.e. the single-particle wave functions, densities, natural orbitals and so on. It is also possible to alter the Hamiltonian, as shown in the last five lines of the input file. In this case a harmonic well and the interaction strength were specified. For most simulations, the definition of the potential is the only case where a few *MATLAB* commands may be required. However, it is always possible to create an array of numbers $[a_1, a_2, \dots]$ which explicitly defines the potential value on each and every spatial grid point.

The simulation can then be started on a command line, i.e. *bash* interface, with

```
$ qiwb -i well.inp -d well -scr
```

All output files are saved into the directory *well*. The option “-scr” is non-obligatory and turns on additional output to be written onto the screen. Once the simulation has finished, the data can be analysed. The output files contain all the necessary information, such as the population of the natural orbitals (*pop_nat*), spatial populations (*spatial_populations*), energies (*log*) and CPU

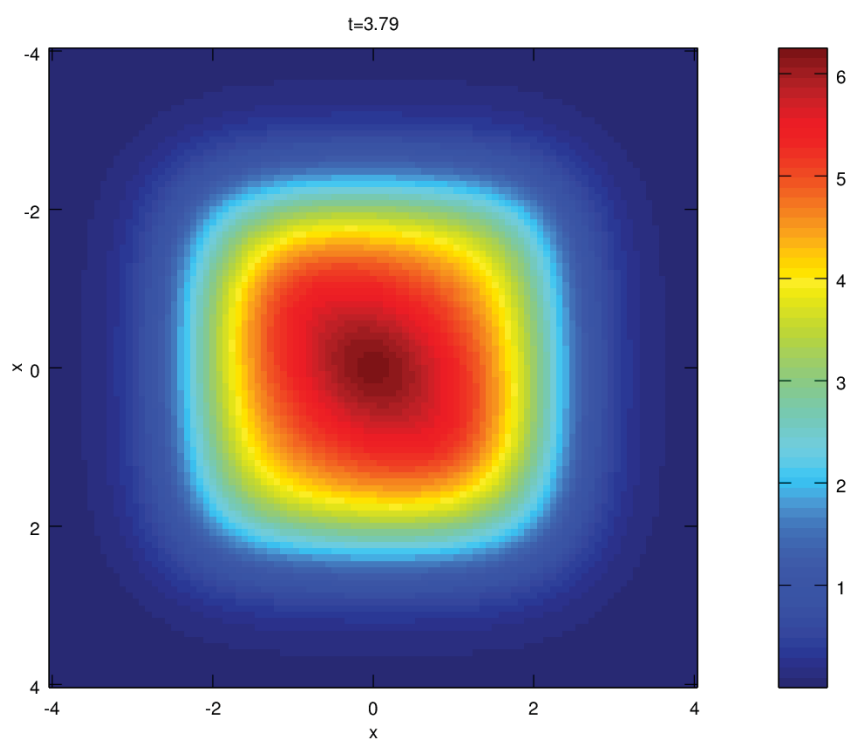


Figure D.2: Reduced one-body density matrix $\rho(x, y)$ for 20 particles confined in a harmonic well (see text) after being relaxed to the ground state. This picture is an exact copy of the image generated by one of the plotting tools that are integrated in QiwiB.

APPENDIX D. THE QIWIB PROGRAM PACKAGE

times (*steps*). The subdirectory *time_dep* contains the densities, single-particle wave functions and other relevant information needed by some of the Qiwib analysis tools. Most of the files are human-readable and mainly contain columns with numbers. Therefore, they can be loaded and processed in text editors, spreadsheets or similar programs. Other data, such as the one-body or two-body density matrices have to be generated first by the provided analysis tools.

To give an example, Figs. D.1 and D.2 have been generated by the following two commands:

```
$ plot_density -i well -t 3.79
$ plot_g1 -i well -ri real -t 3.79
```

These commands create a plot showing the one-dimensional density and the reduced one-body density matrix at $t = 3.79$. Both pictures are snapshots of the system at $t = 3.79$. To get a list of all options, for actions such as the creation of animations, both commands can be started without any parameters to get short help output. Furthermore, the data can be extracted from the pictures and saved into an *ASCII* file, which can be loaded and processed by other third-party programs.

All available scripts are explained in the *Usage* section of the *html* documentation.

D.3.2 Travelling bright soliton

We now demonstrate how to initiate a time-dependent simulation. First, an initial soliton is created via a relaxation process defined in the input file *soliton_relax.inp*:

```
% soliton_relax.inp
pa.relaxation = 0;
pa.N=90;
pa.M=2;
pa.Ng=71;
```

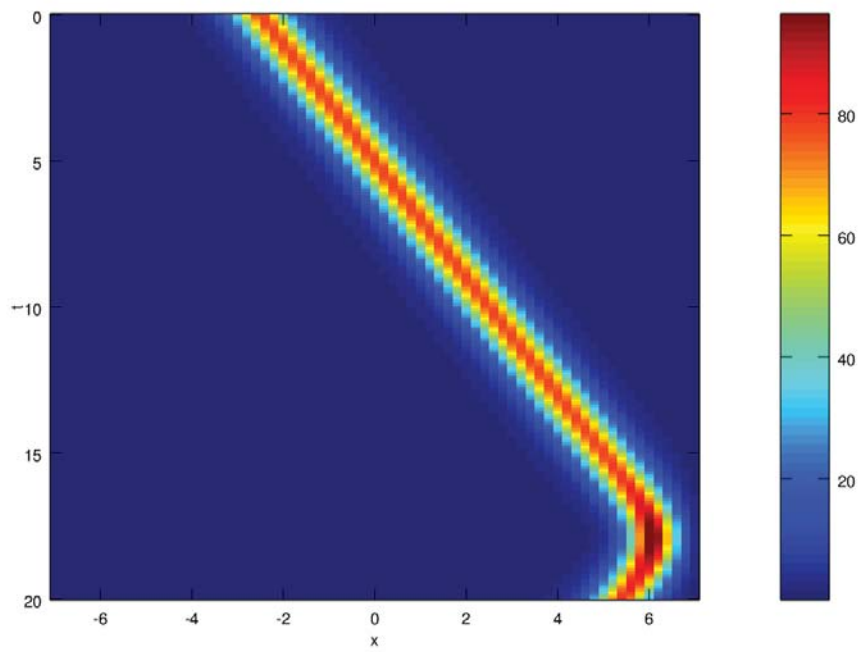


Figure D.3: Density of a soliton of 90 particles confined in a box of length $L = 14$. The soliton travels to the right with an initial velocity of $v = 0.5$ and bounces off the right wall at $t \approx 18$. This picture is an exact copy of the image generated by one of the plotting tools that are integrated in QiviB.

APPENDIX D. THE QIWIB PROGRAM PACKAGE

```
pa.L=14;
pa.xpos0=-7;

pa.dE_limit = 1E-8;
pa.CMF_error = 1E-4; % defines the constant mean-field error tolerance
pa.save_step = 1.0;
pa.save_options = [1,1,1,1,1];

% Define the numerical propagators
pa.improved_rlx = 'fixed'; % always take the lowest eigenstate for improved relaxation
pa.ode_phi = "RK78"; % Runge-Kutta 7th-8th order
% Below: defines error tolerance for Runge-Kutta
pa.ode_phi_opts = odeset("AbsTol",1e-10,"InitialStep",1e-4,"MaxStep",1e-2,"RelTol",1e-10);
pa.ode_C = "eigs"; % solves eigenvalue problem for the  $\vec{C}$  vector
pa.ode_C_opts = [20,40,1E-9]; % defines error tolerance and maximal number of Lanczos vectors

pa.H_update_step = 1.0; % The Hamiltonian function below will be called every time unit
function hamiltonian_t(t)
mlock(); global pa
pa.g= -0.04;
% Below: Initially a potential well is used to place the soliton at  $x = -2.5$ .
% After  $t = 10$  we set  $V(x) = 0$ 
pa.V = exp(-t/1)*1.0*([pa.xpos0+2.5:pa.L/(pa.Ng-1):pa.xpos0+2.5+pa.L]'.^2);
if t>10, pa.V = 0; end
endfunction
```

Notice that the Hamiltonian function is now time dependent. This allows for the inclusion of time-dependent potentials, interaction strengths or frequencies if working in a rotating frame. For the relaxation in this section the Hamiltonian function will now be called every time unit. This allows us to fix the central position of the bright soliton via a harmonic potential. The calculation is initiated with the command:

```
$ qiwb -i soliton_relax.inp -d soliton_relax
```

This creates a directory *soliton_relax* which includes a restart file with the ground state soliton data that can be used as an initial state for the following time-dependent simulation.

The input file *soliton_prop.inp* for the propagation of the soliton is given by

```

% soliton_prop.inp

pa.relaxation = -1; % initialise a propagation run
pa.load_phi_C = 'soliton_relax/phiC_restart.gz'; % give the location of the restart file
pa.N=90;
pa.M=2;
pa.Ng=71;
pa.L=14;
pa.xpos0=-7;

% Below: defines a vector that will be multiplied with the initial wave function element by element
% It adds a phase to the initial soliton which equals to an initial velocity of 0.5
pa.phi = exp( i*0.5*repmat([pa.xpos0+2.5:pa.L/(pa.Ng-1):pa.xpos0+2.5+pa.L]',1,pa.M) );

pa.endtime = 20; % maximal time the simulation is running
pa.CMF_error = 1E-6;
pa.save_step = 0.1;
pa.save_options = [1,1,1,1,1];
pa.ode_phi = "RK78";
pa.ode_phi_opts = odeset("AbsTol",1e-10,"InitialStep",1e-4,"MaxStep",1e-2,"RelTol",1e-10);
pa.ode_C = "lanczos"; % using a Lanczos propagator
pa.ode_C_opts = [50,1E-10];

function hamiltonian_t(t)
mlock(); global pa
    pa.g= -0.04;
endfunction

```

This input file loads the previously created soliton and adds an initial velocity of $v = 0.5$. Then, the soliton travels to the right for 20 time units. We start the simulation with

```
$ qiwb -i soliton_prop.inp -d soliton_prop -scr
```

After the simulation finished, we plot the density as a function of time by running

```
$ plot_density -np -dt 0.1 -i soliton_prop
```

The resulting graph is shown in the Fig. D.3.

APPENDIX D. THE QIWIB PROGRAM PACKAGE

This ends this section of two example calculations with Qiwib. For further reading we recommend to read the *html* documentation and to test some of the example input files included in the *sample_input* directory of the Qiwib program package. Publications by the author

Published works by the author

Works incorporated into this thesis

Articles

- T. Ernst and J. Brand, *Resonant trapping in the transport of a matter-wave soliton through a quantum well*, *Phys. Rev. A* **81**, 033614 (2010).
- T. Ernst, D. Hallwood, J. Gulliksen, H. Meyer, and J. Brand, *Simulating strongly correlated multiparticle systems in a truncated Hilbert space*, *Phys. Rev. A* **84**, 023623 (2011).
- D. W. Hallwood, T. Ernst, and J. Brand, *Robust mesoscopic superposition of strongly correlated ultracold atoms*, *Phys. Rev. A* **82**, 063623 (2010).

Copyright for these publications is held by the American Physical Society.

Software

- QiwiB program package, <http://qiwiB.googlecode.com/>.

Other works during the course of the PhD

- T. Ernst, T. Paul, and P. Schlagheck, *Transport of ultracold Bose gases beyond the Gross-Pitaevskii description*, *Phys. Rev. A* **81**, 013631 (2010).

APPENDIX D. THE QIWIB PROGRAM PACKAGE

Bibliography

- [1] A. Einstein, *Sitzungsber. Preuss. Akad. Wiss.* **261** (1924).
- [2] A. Einstein, *Sitzungsber. Preuss. Akad. Wiss.* **3** (1925).
- [3] Bose, *Plancks Gesetz und Lichtquantenhypothese, Z. Phys.* **26**, 178 (1924).
- [4] T. Hänsch and A. Schawlow, *Cooling of gases by laser radiation, Opt. Commun.* **13**, 68 (1975).
- [5] M. H. Anderson, J. R. Ensher, M. R. Matthews, C. E. Wieman, and E. A. Cornell, *Observation of Bose-Einstein Condensation in a Dilute Atomic Vapor, Science* **269**, pp. 198 (1995).
- [6] K. B. Davis, M. O. Mewes, M. R. Andrews, N. J. van Druten, D. S. Durfee, D. M. Kurn, and W. Ketterle, *Bose-Einstein Condensation in a Gas of Sodium Atoms, Phys. Rev. Lett.* **75**, 3969 (1995).
- [7] M. R. Andrews, C. G. Townsend, H.-J. Miesner, D. S. Durfee, D. M. Kurn, and W. Ketterle, *Observation of Interference Between Two Bose Condensates, Science* **275**, 637 (1997).
- [8] D. Jaksch, C. Bruder, J. I. Cirac, C. W. Gardiner, and P. Zoller, *Cold Bosonic Atoms in Optical Lattices, Phys. Rev. Lett.* **81**, 3108 (1998).
- [9] C. Orzel, A. Tuchman, M. Fenselau, M. Yasuda, and M. Kasevich, *Squeezed states in a Bose-Einstein condensate, Science* **291**, 2386 (2001).
- [10] I. Bloch, *Ultracold quantum gases in optical lattices, Nat. Phys.* **1**, 23 (2005).
- [11] O. Morsch and M. Oberthaler, *Dynamics of Bose-Einstein condensates in optical lattices, Rev. Mod. Phys.* **78**, 179 (2006).
- [12] M. Greiner, O. Mandel, T. Esslinger, T. Hänsch, and I. Bloch, *Quantum phase transition from a superfluid to a Mott insulator in a gas of ultracold atoms, Nature* **415**, 39 (2002).

BIBLIOGRAPHY

- [13] T. Stöferle, H. Moritz, C. Schori, M. Köhl, and T. Esslinger, *Transition from a Strongly Interacting 1D Superfluid to a Mott Insulator*, *Phys. Rev. Lett.* **92**, 130403 (2004).
- [14] M. Holland, S. Kokkelmans, M. Chiofalo, and R. Walser, *Resonance superfluidity in a quantum degenerate Fermi gas*, *Phys. Rev. Lett.* **87**, 120406 (2001).
- [15] A. Truscott, K. Strecker, W. McAlexander, G. Partridge, and R. Hulet, *Observation of Fermi pressure in a gas of trapped atoms*, *Science* **291**, 2570 (2001).
- [16] K. O'Hara, S. Hemmer, M. Gehm, S. Granade, and J. Thomas, *Observation of a strongly interacting degenerate Fermi gas of atoms*, *Science* **298**, 2179 (2002).
- [17] C. Regal, C. Ticknor, J. Bohn, and D. Jin, *Creation of ultracold molecules from a Fermi gas of atoms.*, *Nature* **424**, 47 (2003).
- [18] J. Bardeen, L. Cooper, and J. Schrieffer, *Theory of superconductivity*, *Phys. Rev.* **108**, 1175 (1957).
- [19] M. Bartenstein, A. Altmeyer, S. Riedl, S. Jochim, C. Chin, J. Denschlag, and R. Grimm, *Crossover from a molecular Bose-Einstein condensate to a degenerate Fermi gas*, *Phys. Rev. Lett.* **92**, 120401 (2004).
- [20] J. Ruostekoski, M. J. Collett, R. Graham, and D. F. Walls, *Macroscopic superpositions of Bose-Einstein condensates*, *Phys. Rev. A* **57**, 511 (1998).
- [21] J. I. Cirac, M. Lewenstein, K. Mølmer, and P. Zoller, *Quantum superposition states of Bose-Einstein condensates*, *Phys. Rev. A* **57**, 1208 (1998).
- [22] M. J. Steel and M. J. Collett, *Quantum state of two trapped Bose-Einstein condensates with a Josephson coupling*, *Phys. Rev. A* **57**, 2920 (1998).
- [23] D. Gordon and C. M. Savage, *Creating macroscopic quantum superpositions with Bose-Einstein condensates*, *Phys. Rev. A* **59**, 4623 (1999).

- [24] K. W. Mahmud, J. N. Kutz, and W. P. Reinhardt, *Bose-Einstein condensates in a one-dimensional double square well: Analytical solutions of the nonlinear Schrödinger equation*, *Phys. Rev. A* **66**, 063607 (2002).
- [25] T.-L. Ho and C. V. Ciobanu, *The Schrödinger Cat Family in Attractive Bose Gases*, *J. Low Temp. Phys.* **135**, 257 (2004).
- [26] Y. P. Huang and M. G. Moore, *Creation, detection, and decoherence of macroscopic quantum superposition states in double-well Bose-Einstein condensates*, *Phys. Rev. A* **73**, 023606 (2006).
- [27] D. J. Masiello and W. P. Reinhardt, *Time-dependent quantum many-body theory of identical bosons in a double well: Early-time ballistic interferences of fragmented and number entangled states*, *Phys. Rev. A* **76**, 043612 (2007).
- [28] C. Weiss and Y. Castin, *Creation and Detection of a Mesoscopic Gas in a Nonlocal Quantum Superposition*, *Phys. Rev. Lett.* **102**, 010403 (2009).
- [29] A. I. Streltsov, O. E. Alon, and L. S. Cederbaum, *Efficient generation and properties of mesoscopic quantum superposition states in an attractive Bose-Einstein condensate threaded by a potential barrier*, *J. Phys. B* **42**, 091004 (5pp) (2009).
- [30] A. I. Streltsov, O. E. Alon, and L. S. Cederbaum, *Scattering of an attractive Bose-Einstein condensate from a barrier: Formation of quantum superposition states*, *Phys. Rev. A* **80**, 043616 (2009).
- [31] D. K. Faust and W. P. Reinhardt, *Analysis of a Bose-Einstein Condensate Double-Well Atom Interferometer*, *Phys. Rev. Lett.* **105**, 240404 (2010).
- [32] Y. Castin, *Simple theoretical tools for low dimension Bose gases*, *J. Phys. IV France* **116**, 89 (2004).
- [33] I. Bloch, J. Dalibard, and W. Zwerger, *Many-body physics with ultracold gases*, *Rev. Mod. Phys.* **80**, 885 (2008).

BIBLIOGRAPHY

- [34] T. Cheon and T. Shigehara, *Fermion-Boson Duality of One-Dimensional Quantum Particles with Generalized Contact Interactions*, *Phys. Rev. Lett.* **82**, 2536 (1999).
- [35] F. Wilczek, *Quantum Mechanics of Fractional-Spin Particles*, *Phys. Rev. Lett.* **49**, 957 (1982).
- [36] M. Girardeau, *Relationship between systems of impenetrable bosons and fermions in one dimension*, *J. Math. Phys.* **1**, 516 (1960).
- [37] I. Romanovsky, C. Yannouleas, and U. Landman, *Crystalline Boson Phases in Harmonic Traps: Beyond the Gross-Pitaevskii Mean Field*, *Phys. Rev. Lett.* **93**, 230405 (2004).
- [38] E. Lieb and W. Liniger, *Exact analysis of an interacting Bose gas. I. The general solution and the ground state*, *Phys. Rev.* **130**, 1605 (1963).
- [39] E. Lieb, *Exact analysis of an interacting Bose gas. II. The excitation spectrum*, *Phys. Rev.* **130**, 1616 (1963).
- [40] A. Griffin, *Conserving and gapless approximations for an inhomogeneous Bose gas at finite temperatures*, *Phys. Rev. B* **53**, 9341 (1996).
- [41] L. Pitaevskii and S. Stringari, *Elementary Excitations in Trapped Bose-Einstein Condensed Gases Beyond the Mean-Field Approximation*, *Phys. Rev. Lett.* **81**, 4541 (1998).
- [42] A. Fabrocini and A. Polls, *Beyond the Gross-Pitaevskii approximation: Local density versus correlated basis approach for trapped bosons*, *Phys. Rev. A* **60**, 2319 (1999).
- [43] D. Hutchinson, K. Burnett, R. Dodd, S. Morgan, M. Rusch, E. Zaremba, N. Proukakis, M. Edwards, and C. Clark, *Gapless mean-field theory of Bose-Einstein condensates*, *J. Phys. B* **33**, 3825 (2000).
- [44] P. Blakie, A. Bradley, M. Davis, R. Ballagh, and C. Gardiner, *Dynamics and statistical mechanics of ultra-cold Bose gases using c-field techniques*, *Adv. Phys.* **57** (2008).

- [45] C. Pethick and H. Smith, *Bose-Einstein condensation in dilute gases* (Cambridge University Press, 2002).
- [46] L. Pitaevskii and S. Stringari, *Bose-Einstein Condensation* (Oxford University Press, USA, 2003).
- [47] R. K. Smith, *Travelling waves and bores in the lower atmosphere: the 'morning glory' and related phenomena*, *Earth-Sci. Rev.* **25**, 267 (1988).
- [48] G. Agrawal, *Nonlinear Fiber Optics* (Springer Berlin / Heidelberg, 2000).
- [49] Y. S. Kivshar and B. A. Malomed, *Dynamics of solitons in nearly integrable systems*, *Rev. Mod. Phys.* **61**, 763 (1989).
- [50] L. Khaykovich, F. Schreck, G. Ferrari, T. Bourdel, J. Cubizolles, L. D. Carr, Y. Castin, and C. Salomon, *Formation of a Matter-Wave Bright Soliton*, *Science* **296**, 1290 (2002).
- [51] K. E. Strecker, G. B. Partridge, A. G. Truscott, and R. G. Hulet, *Formation and propagation of matter-wave soliton trains*, *Nature* **417**, 150 (2002).
- [52] B. Eiermann, T. Anker, M. Albiez, M. Taglieber, P. Treutlein, K.-P. Marzlin, and M. K. Oberthaler, *Bright Bose-Einstein Gap Solitons of Atoms with Repulsive Interaction*, *Phys. Rev. Lett.* **92**, 230401 (2004).
- [53] N. Zabusky and M. Kruskal, *Interaction of Solitons in a Collisionless Plasma and the Recurrence of Initial States*, *Phys. Rev. Lett.* **15**, 240 (1965).
- [54] R. Rajaraman, *Solitons and instantons: an introduction to solitons and instantons in quantum field theory* (North-Holland, 1982).
- [55] A. Hasegawa and F. Tappert, *Transmission of stationary nonlinear optical pulses in dispersive dielectric fibers. I. Anomalous dispersion*, *Appl. Phys. Lett.* **23**, 142 (1973).
- [56] Y. Kivshar and G. Agrawal, *Optical solitons* (Academic Press Boston, 2003).
- [57] K. Forinash, M. Peyrard, and B. Malomed, *Interaction of discrete breathers with impurity modes*, *Phys. Rev. E* **49**, 3400 (1994).

BIBLIOGRAPHY

- [58] X. Cao and B. Malomed, *Soliton-defect collisions in the nonlinear Schrödinger equation*, *Phys. Lett. A* **206**, 177 (1995).
- [59] D. Frantzeskakis, G. Theocharis, F. Diakonov, P. Schmelcher, and Y. Kivshar, *Interaction of dark solitons with localized impurities in Bose-Einstein condensates*, *Phys. Rev. A* **66**, 53608 (2002).
- [60] A. E. Miroshnichenko, S. Flach, and B. Malomed, *Resonant scattering of solitons*, *Chaos* **13**, 874 (2003).
- [61] V. Ahufinger, A. Mebrahtu, R. Corbalán, and A. Sanpera, *Quantum switches and quantum memories for matter-wave lattice solitons*, *New J. Phys.* **9**, 4 (2007).
- [62] H. Sakaguchi and M. Tamura, *Scattering and Trapping of Nonlinear Schrödinger Solitons in External Potentials*, *J. Phys. Soc. Jpn.* **73**, 503 (2004).
- [63] R. H. Goodman, P. J. Holmes, and M. I. Weinstein, *Strong NLS soliton-defect interactions*, *Physica D* **192**, 215 (2004).
- [64] K. T. Stoychev, M. T. Primatarowa, and R. S. Kamburova, *Resonant scattering of nonlinear Schrödinger solitons from potential wells*, *Phys. Rev. E* **70**, 066622 (2004).
- [65] L. Morales-Molina and R. A. Vicencio, *Trapping of discrete solitons by defects in nonlinear waveguide arrays*, *Opt. Lett.* **31**, 966 (2006).
- [66] C. Lee and J. Brand, *Enhanced quantum reflection of matter-wave solitons*, *Europhys. Lett.* **73**, 321 (2006).
- [67] A. Aceves, J. Moloney, and A. Newell, *Theory of light-beam propagation at nonlinear interfaces. I. Equivalent-particle theory for a single interface*, *Phys. Rev. A* **39**, 1809 (1989).
- [68] Y. Kivshar, A. Kosevich, and O. Chubykalo, *Radiative effects in the theory of beam propagation at nonlinear interfaces*, *Phys. Rev. A* **41**, 1677 (1990).

- [69] S. Cornish, N. Parker, A. Martin, T. Judd, R. Scott, T. Fromhold, and C. Adams, *Quantum reflection of bright matter-wave solitons*, *Physica D* **238**, 1299 (2009).
- [70] H. Frauenkron and P. Grassberger, *Unexpected behavior of nonlinear Schrödinger solitons in an external potential*, *Phys. Rev. E* **53**, 2823 (1996).
- [71] H. Friedrich and J. Trost, *Working with WKB waves far from the semiclassical limit*, *Phys. Rep.* **397**, 359 (2004).
- [72] R. Scott, A. Martin, T. Fromhold, and F. Sheard, *Anomalous Quantum Reflection of Bose-Einstein Condensates from a Silicon Surface: The Role of Dynamical Excitations*, *Phys. Rev. Lett.* **95**, 73201 (2005).
- [73] R. Scott, C. Gardiner, and D. Hutchinson, *Nonequilibrium dynamics: Studies of the reflection of Bose-Einstein condensates*, *Las. Phys.* **17**, 527 (2007).
- [74] T. A. Pasquini, Y. Shin, C. Sanner, M. Saba, A. Schirotzek, D. E. Pritchard, and W. Ketterle, *Quantum Reflection from a Solid Surface at Normal Incidence*, *Phys. Rev. Lett.* **93**, 223201 (2004).
- [75] T. A. Pasquini, M. Saba, G.-B. Jo, Y. Shin, W. Ketterle, D. E. Pritchard, T. A. Savas, and N. Mulders, *Low Velocity Quantum Reflection of Bose-Einstein Condensates*, *Phys. Rev. Lett.* **97**, 093201 (2006).
- [76] A. I. Streltsov, O. E. Alon, and L. S. Cederbaum, *Formation and Dynamics of Many-Boson Fragmented States in One-Dimensional Attractive Ultracold Gases*, *Phys. Rev. Lett.* **100**, 130401 (2008).
- [77] A. I. Streltsov, O. E. Alon, and L. S. Cederbaum, *Swift Loss of Coherence of Soliton Trains in Attractive Bose-Einstein Condensates*, *Phys. Rev. Lett.* **106**, 240401 (2011).
- [78] T. Paul, K. Richter, and P. Schlagheck, *Nonlinear Resonant Transport of Bose-Einstein Condensates*, *Phys. Rev. Lett.* **94**, 020404 (2005).
- [79] T. Ernst, T. Paul, and P. Schlagheck, *Transport of ultracold Bose gases beyond the Gross-Pitaevskii description*, *Phys. Rev. A* **81**, 013631 (2010).

BIBLIOGRAPHY

- [80] C. Chin, R. Grimm, P. Julienne, and E. Tiesinga, *Feshbach resonances in ultracold gases*, *Rev. Mod. Phys.* **82**, 1225 (2010).
- [81] T. Grunzweig, A. Hilliard, M. McGovern, and M. F. Andersen, *Near-deterministic preparation of a single atom in an optical microtrap*, *Nat. Phys.* **6**, 951 (2010).
- [82] F. Deuretzbacher, K. Bongs, K. Sengstock, and D. Pfannkuche, *Evolution from a Bose-Einstein condensate to a Tonks-Girardeau gas: An exact diagonalization study*, *Phys. Rev. A* **75**, 013614 (2007).
- [83] R. Kanamoto, H. Saito, and M. Ueda, *Symmetry Breaking and Enhanced Condensate Fraction in a Matter-Wave Bright Soliton*, *Phys. Rev. Lett.* **94**, 090404 (2005).
- [84] D. W. Hallwood, T. Ernst, and J. Brand, *Robust mesoscopic superposition of strongly correlated ultracold atoms*, *Phys. Rev. A* **82**, 063623 (2010).
- [85] G. Vidal, *Efficient Classical Simulation of Slightly Entangled Quantum Computations*, *Phys. Rev. Lett.* **91**, 147902 (2003).
- [86] S. R. White and A. E. Feiguin, *Real-Time Evolution Using the Density Matrix Renormalization Group*, *Phys. Rev. Lett.* **93**, 076401 (2004).
- [87] A. J. Daley, C. Kollath, U. Schollwöck, and G. Vidal, *Time-dependent density-matrix renormalization-group using adaptive effective Hilbert spaces*, *J. Stat. Mech.* **2004**, P04005 (2004).
- [88] H.-D. Meyer, U. Manthe, and L. Cederbaum, *The multi-configurational time-dependent Hartree approach*, *Chem. Phys. Lett.* **165**, 73 (1990).
- [89] M. Beck, A. Jäckle, G. Worth, and H.-D. Meyer, *The multiconfiguration time-dependent Hartree (MCTDH) method: a highly efficient algorithm for propagating wavepackets*, *Phys. Rep.* **324**, 1 (2000).
- [90] H.-D. Meyer, F. Gatti, and G. Worth, *Multidimensional quantum dynamics: MCTDH theory and applications* (Wiley-VCH, Weinheim, 2009).

- [91] <http://www.pci.uni-heidelberg.de/cms/mctdh.html>.
- [92] O. E. Alon, A. I. Streltsov, and L. S. Cederbaum, *Multiconfigurational time-dependent Hartree method for bosons: Many-body dynamics of bosonic systems*, *Phys. Rev. A* **77**, 033613 (2008).
- [93] <http://mctdhb.uni-hd.de>.
- [94] T. Ernst and J. Brand, *Resonant trapping in the transport of a matter-wave soliton through a quantum well*, *Phys. Rev. A* **81**, 033614 (2010).
- [95] T. Ernst, D. W. Hallwood, J. Gulliksen, H.-D. Meyer, and J. Brand, *Simulating strongly correlated multiparticle systems in a truncated Hilbert space*, *Phys. Rev. A* **84**, 023623 (2011).
- [96] <http://qiwiib.googlecode.com/>.
- [97] L. Landau and E. Lifshitz, *Statistical Physics Part 1 and 2* (Pergamon Oxford, UK, 1980).
- [98] E. Fermi, *Sul moto dei neutroni nelle sostanze idrogenante*, *Ric. Sci. Progr. Tecn. Econom. Naz.* **2**, 13 (1936).
- [99] K. Huang, *Statistical Mechanics* (John Wiley & Sons, New York, 1963).
- [100] C. Buggle, J. Léonard, W. von Klitzing, and J. T. M. Walraven, *Interferometric Determination of the s and d-Wave Scattering Amplitudes in ^{87}Rb* , *Phys. Rev. Lett.* **93**, 173202 (2004).
- [101] D. A. W. Hutchinson, E. Zaremba, and A. Griffin, *Finite Temperature Excitations of a Trapped Bose Gas*, *Phys. Rev. Lett.* **78**, 1842 (1997).
- [102] A. Norrie, *A Classical Field Treatment of Colliding Bose-Einstein Condensates*, PhD thesis University of Otago, New Zealand 2005.
- [103] P. D. Drummond and C. W. Gardiner, *Generalised P-representations in quantum optics*, *J. Phys. A* **13**, 2353 (1980).

BIBLIOGRAPHY

- [104] A. Gilchrist, C. W. Gardiner, and P. D. Drummond, *Positive P representation: Application and validity*, *Phys. Rev. A* **55**, 3014 (1997).
- [105] E. Wigner, *On the Quantum Correction For Thermodynamic Equilibrium*, *Phys. Rev.* **40**, 749 (1932).
- [106] C. Gardiner and P. Zoller, *Quantum noise: a handbook of Markovian and non-Markovian quantum stochastic methods with applications to quantum optics* (Springer Verlag, 2004).
- [107] A. Sinatra, C. Lobo, and Y. Castin, *Classical-Field Method for Time Dependent Bose-Einstein Condensed Gases*, *Phys. Rev. Lett.* **87**, 210404 (2001).
- [108] T. Ernst, *Many body effects in the transport of Bose-Einstein Condensates*, Master's thesis University of Regensburg, Germany 2006.
- [109] M. Olshanii, *Atomic Scattering in the Presence of an External Confinement and a Gas of Impenetrable Bosons*, *Phys. Rev. Lett.* **81**, 938 (1998).
- [110] A. Görlitz *et al.*, *Realization of Bose-Einstein condensates in lower dimensions*, *Phys. Rev. Lett.* **87**, 130402 (2001).
- [111] L. Landau, *Theory of the superfluidity of helium II*, *Phys. Rev.* **60**, 356 (1941).
- [112] H. Bethe, *Zur Theorie der Metalle*, *Z. Phys. A* **71**, 205 (1931).
- [113] T. Kinoshita, T. Wenger, and D. Weiss, *Observation of a one-dimensional Tonks-Girardeau gas*, *Science* **305**, 1125 (2004).
- [114] B. Paredes, A. Widera, V. Murg, O. Mandel, S. Fölling, I. Cirac, G. Shlyapnikov, T. Hänsch, and I. Bloch, *Tonks-Girardeau gas of ultracold atoms in an optical lattice*, *Nature* **429**, 277 (2004).
- [115] C. Yang and C. Yang, *Thermodynamics of a One-Dimensional System of Bosons with Repulsive Delta-Function Interaction*, *J. Math. Phys.* **10**, 1115 (1969).
- [116] N. Bogoliubov, *On the theory of superfluidity*, *J. Phys. (USSR)* **11**, 4 (1947).

- [117] J. Russell, *Report on waves*, in *14th meeting of the British Association for the Advancement of Science* pp. 311–390 1844.
- [118] Z. Sinkala, *Soliton/exciton transport in proteins*, *J. Theor. Biol.* **241**, 919 (2006).
- [119] J. Brand and W. P. Reinhardt, *Generating ring currents, solitons and vortices by stirring a Bose-Einstein condensate in a toroidal trap*, *J. Phys. B* **34**, L113 (2001).
- [120] J. Brand and W. P. Reinhardt, *Solitonic vortices and the fundamental modes of the “snake instability”: Possibility of observation in the gaseous Bose-Einstein condensate*, *Phys. Rev. A* **65**, 043612 (2002).
- [121] V. M. Pérez-García, H. Michinel, J. I. Cirac, M. Lewenstein, and P. Zoller, *Dynamics of Bose-Einstein condensates: Variational solutions of the Gross-Pitaevskii equations*, *Phys. Rev. A* **56**, 1424 (1997).
- [122] L. Carr and Y. Castin, *Dynamics of a matter-wave bright soliton in an expulsive potential*, *Phys. Rev. A* **66**, 63602 (2002).
- [123] L. D. Carr and J. Brand, *Spontaneous Soliton Formation and Modulational Instability in Bose-Einstein Condensates*, *Phys. Rev. Lett.* **92**, 040401 (2004).
- [124] S. Sinha, A. Cherny, D. Kovrizhin, and J. Brand, *Friction and Diffusion of Matter-Wave Bright Solitons*, *Phys. Rev. Lett.* **96**, 30406 (2006).
- [125] U. Manthe, H.-D. Meyer, and L. Cederbaum, *Wave-packet dynamics within the multiconfiguration Hartree framework: General aspects and application to NOCl*, *J. Chem. Phys.* **97**, 3199 (1992).
- [126] M. Beck and H.-D. Meyer, *An efficient and robust integration scheme for the equations of motion of the multiconfiguration time-dependent Hartree (MCTDH) method*, *Z. Phys. D* **42**, 113 (1997).
- [127] S. Zöllner, H.-D. Meyer, and P. Schmelcher, *Composite fermionization of one-dimensional Bose-Bose mixtures*, *Phys. Rev. A* **78**, 013629 (2008).

BIBLIOGRAPHY

- [128] S. Zöllner, H.-D. Meyer, and P. Schmelcher, *Tunneling dynamics of a few bosons in a double well*, *Phys. Rev. A* **78**, 013621 (2008).
- [129] J. W. Eaton, *GNU Octave Manual* (Network Theory Limited, 2002).
- [130] F. Schwabl, *Quantum mechanics* (Springer, 2007).
- [131] J. P. Gordon, *Interaction forces among solitons in optical fibers*, *Opt. Lett.* **8**, 596 (1983).
- [132] X. Yin, Y. Hao, S. Chen, and Y. Zhang, *Ground-state properties of a few-boson system in a one-dimensional hard-wall split potential*, *Phys. Rev. A* **78**, 013604 (2008).
- [133] Hao, Y. J. and Chen, S., *Ground-state properties of interacting two-component Bose gases in a one-dimensional harmonic trap*, *Eur. Phys. J. D* **51**, 261 (2009).
- [134] S. Zöllner, H.-D. Meyer, and P. Schmelcher, *Ultracold few-boson systems in a double-well trap*, *Phys. Rev. A* **74**, 053612 (2006).
- [135] S. Zöllner, H.-D. Meyer, and P. Schmelcher, *Correlations in ultracold trapped few-boson systems: Transition from condensation to fermionization*, *Phys. Rev. A* **74**, 063611 (2006).
- [136] K. Suzuki and S. Lee, *Convergent theory for effective interaction in nuclei*, *Prog. Theor. Phys.* **64**, 2091 (1980).
- [137] I. Stetcu, B. R. Barrett, U. van Kolck, and J. P. Vary, *Effective theory for trapped few-fermion systems*, *Phys. Rev. A* **76**, 063613 (2007).
- [138] Y. Alhassid, G. F. Bertsch, and L. Fang, *New Effective Interaction for the Trapped Fermi Gas*, *Phys. Rev. Lett.* **100**, 230401 (2008).
- [139] J. Christensson, C. Forssén, S. Åberg, and S. M. Reimann, *Effective-interaction approach to the many-boson problem*, *Phys. Rev. A* **79**, 012707 (2009).

- [140] M. Albiez, R. Gati, J. Fölling, S. Hunsmann, M. Cristiani, and M. Oberthaler, *Direct observation of tunneling and nonlinear self-trapping in a single bosonic Josephson junction*, *Phys. Rev. Lett.* **95**, 10402 (2005).
- [141] L. Carr, D. Dounas-Frazer, and M. Garcia-March, *Dynamical realization of macroscopic superposition states of cold bosons in a tilted double well*, *Europhys. Lett.* **90**, 10005 (2010).
- [142] G. Brennen, C. Caves, P. Jessen, and I. Deutsch, *Quantum logic gates in optical lattices*, *Phys. Rev. Lett.* **82**, 1060 (1999).
- [143] D. Tretyakov, I. Beterov, V. Entin, and I. Ryabtsev, *Cold atoms in optical lattices as qubits for a quantum computer*, *Russ. Microelectronics* **35**, 74 (2006).
- [144] Z. Bacić and J. C. Light, *Highly excited vibrational levels of floppy triatomic molecules: A discrete variable representation-Distributed Gaussian basis approach*, *J. Chem. Phys.* **85**, 4594 (1986).
- [145] R. Kosloff and H. Tal-Ezer, *A direct relaxation method for calculating eigenfunctions and eigenvalues of the Schrödinger equation on a grid*, *Chem. Phys. Lett.* **127**, 223 (1986).
- [146] H.-D. Meyer, F. Quéré, C. Léonard, and F. Gatti, *Calculation and selective population of vibrational levels with the Multiconfiguration Time-Dependent Hartree (MCTDH) algorithm*, *Chem. Phys.* **329**, 179 (2006).
- [147] L. Doriol, F. Gatti, C. Iung, and H.-D. Meyer, *Computation of vibrational energy levels and eigenstates of fluorofrom using the multiconfiguration time-dependent Hartree method*, *J. Chem. Phys.* **129**, 224109 (2008).
- [148] T. Busch, B.-G. Englert, K. Rzażewski, and M. Wilkens, *Two Cold Atoms in a Harmonic Trap*, *Found. Phys.* **28**, 549 (1998).
- [149] J. A. Jones, S. D. Karlen, J. Fitzsimons, A. Ardavan, S. C. Benjamin, G. A. D. Briggs, and J. J. L. Morton, *Magnetic Field Sensing Beyond the Standard Quantum Limit Using 10-Spin NOON States*, *Science* **324**, 1166 (2009).

BIBLIOGRAPHY

- [150] L. D. Carr and J. Brand, *Pulsed atomic soliton laser*, *Phys. Rev. A* **70**, 033607 (2004).
- [151] T. Lahaye, C. Menotti, L. Santos, M. Lewenstein, and T. Pfau, *The physics of dipolar bosonic quantum gases*, *Rep. Prog. Phys.* **72**, 126401 (2009).
- [152] J. Brand, T. J. Haigh, and U. Zülicke, *Rotational fluxons of Bose-Einstein condensates in coplanar double-ring traps*, *Phys. Rev. A* **80**, 011602 (2009).
- [153] J. Brand, T. J. Haigh, and U. Zülicke, *Sign of coupling in barrier-separated Bose-Einstein condensates and stability of double-ring systems*, *Phys. Rev. A* **81**, 025602 (2010).
- [154] V. Giovannetti, S. Lloyd, and L. Maccone, *Quantum-Enhanced Measurements: Beating the Standard Quantum Limit*, *Science* **306**, 1330 (2004).
- [155] A. J. Leggett and A. Garg, *Quantum mechanics versus macroscopic realism: Is the flux there when nobody looks?*, *Phys. Rev. Lett.* **54**, 857 (1985).
- [156] C. H. van der Wal, A. C. J. ter Haar, F. K. Wilhelm, R. N. Schouten, C. J. P. M. Harmans, T. P. Orlando, S. Lloyd, and J. E. Mooij, *Quantum Superposition of Macroscopic Persistent-Current States*, *Science* **290**, 773 (2000).
- [157] J. Friedman, V. Patel, W. Chen, S. Tolpygo, and J. Lukens, *Quantum superposition of distinct macroscopic states*, *Nature* **406**, 43 (2000).
- [158] F. Marquardt, B. Abel, and J. von Delft, *Measuring the size of a quantum superposition of many-body states*, *Phys. Rev. A* **78**, 012109 (2008).
- [159] A. Leggett, *Chance and Matter, Proceedings, 1986 Les Houches Summer School*, (1987).
- [160] J. I. Korsbakken, K. B. Whaley, J. Dubois, and J. I. Cirac, *Measurement-based measure of the size of macroscopic quantum superpositions*, *Phys. Rev. A* **75**, 042106 (2007).

- [161] J. Korsbakken, F. Wilhelm, and K. Whaley, *Electronic structure of superposition states in flux qubits*, *Phys. Scr.* **2009**, 014022 (2009).
- [162] K. T. Kapale and J. P. Dowling, *Vortex Phase Qubit: Generating Arbitrary, Counterrotating, Coherent Superpositions in Bose-Einstein Condensates via Optical Angular Momentum Beams*, *Phys. Rev. Lett.* **95**, 173601 (2005).
- [163] J. Dunningham, K. Burnett, R. Roth, and W. Phillips, *Creation of macroscopic superposition states from arrays of Bose-Einstein condensates*, *New J. Phys.* **8**, 182 (2006).
- [164] Z. F. Xu, P. Zhang, R. Lü, and L. You, *Quantum pump for countercirculation in a spinor Bose-Einstein condensate*, *Phys. Rev. A* **81**, 053619 (2010).
- [165] P. Bader and U. R. Fischer, *Fragmented Many-Body Ground States for Scalar Bosons in a Single Trap*, *Phys. Rev. Lett.* **103**, 060402 (2009).
- [166] W. H. Zurek, *Decoherence, einselection, and the quantum origins of the classical*, *Rev. Mod. Phys.* **75**, 715 (2003).
- [167] D. Hallwood, K. Burnett, and J. Dunningham, *The barriers to producing multiparticle superposition states in rotating Bose-Einstein condensates*, *J. Mod. Optic.* **54**, 2129 (2007).
- [168] D. R. Dounas-Frazer, A. M. Hermundstad, and L. D. Carr, *Ultracold Bosons in a Tilted Multilevel Double-Well Potential*, *Phys. Rev. Lett.* **99**, 200402 (2007).
- [169] W. Press, S. Teukolsky, W. Vetterling, and B. Flannery, *Numerical Recipes in C*, 2nd ed. (Cambridge University Press, Cambridge, UK, 1992).
- [170] <http://octave.sourceforge.net>.
- [171] J. R. Cash and A. H. Karp, *A variable order Runge-Kutta method for initial value problems with rapidly varying right-hand sides*, *ACM Trans. Math. Softw.* **16**, 201 (1990).

BIBLIOGRAPHY

- [172] T. Park and J. Light, *Unitary quantum time evolution by iterative Lanczos reduction*, *J. Chem. Phys.* **85**, 5870 (1986).
- [173] U. Manthe, H. Köppel, and L. Cederbaum, *Dissociation and predissociation on coupled electronic potential energy surfaces: A three-dimensional wave packet dynamical study*, *J. Chem. Phys.* **95**, 1708 (1991).
- [174] <http://www.gnu.org/software/octave>.



MASSEY UNIVERSITY
GRADUATE RESEARCH SCHOOL

**STATEMENT OF CONTRIBUTION
TO DOCTORAL THESIS CONTAINING PUBLICATIONS**

(To appear at the end of each thesis chapter/section/appendix submitted as an article/paper or collected as an appendix at the end of the thesis)

We, the candidate and the candidate's Principal Supervisor, certify that all co-authors have consented to their work being included in the thesis and they have accepted the candidate's contribution as indicated below in the *Statement of Originality*.

Name of Candidate: Thomas Ernst

Name/Title of Principal Supervisor: Prof. Joachim Brand

Name of Published Paper: T. Ernst and J. Brand,
*Resonant trapping in the transport of a matter-wave soliton
through a quantum well, Phys. Rev. A 81, 033614 (2010).*

In which Chapter is the Published Work: Chapter 3

Candidate's contributions:

- All numerical calculations (including programming work)
- Explained resonant processes
- Developed theory on trapping mechanism
- Developed extended variational model
- Wrote most of the paper with minor contributions from supervisor
- Prepared all figures

Candidate's Signature

Date

Principal Supervisor's signature

Date



MASSEY UNIVERSITY
GRADUATE RESEARCH SCHOOL

**STATEMENT OF CONTRIBUTION
TO DOCTORAL THESIS CONTAINING PUBLICATIONS**

(To appear at the end of each thesis chapter/section/appendix submitted as an article/paper or collected as an appendix at the end of the thesis)

We, the candidate and the candidate's Principal Supervisor, certify that all co-authors have consented to their work being included in the thesis and they have accepted the candidate's contribution as indicated below in the *Statement of Originality*.

Name of Candidate: Thomas Ernst

Name/Title of Principal Supervisor: Prof. Joachim Brand

Name of Published Paper: T. Ernst, D. Hallwood, J. Gulliksen, H. Meyer, and J. Brand, *Simulating strongly correlated multiparticle systems in a truncated Hilbert space*, *Phys. Rev. A* **84**, 023623 (2011).

In which Chapter is the Published Work: Section 4.2

Candidate's contributions:

- Developed empirical rescaling scheme
- Performed all calculations for the ring system and partially for the double well
- Assisted Masters student in his work on the harmonic well and double-well
- Wrote most of the paper with minor contributions from the other authors
- Prepared all figures in publication
- Significantly contributed to the derivative of two-body rescaling in discussion with Joachim Brand and David Hallwood

Candidate's Signature

Date

Principal Supervisor's signature

Date



MASSEY UNIVERSITY
GRADUATE RESEARCH SCHOOL

**STATEMENT OF CONTRIBUTION
TO DOCTORAL THESIS CONTAINING PUBLICATIONS**

(To appear at the end of each thesis chapter/section/appendix submitted as an article/paper or collected as an appendix at the end of the thesis)

We, the candidate and the candidate's Principal Supervisor, certify that all co-authors have consented to their work being included in the thesis and they have accepted the candidate's contribution as indicated below in the *Statement of Originality*.

Name of Candidate: Thomas Ernst

Name/Title of Principal Supervisor: Prof. Joachim Brand

Name of Published Paper: D. W. Hallwood, T. Ernst, and J. Brand,
Robust mesoscopic superposition of strongly correlated ultracold atoms, Phys. Rev. A **82**, 063623 (2010).

In which Chapter is the Published Work: Appendix A

Candidate's contributions:

- Assisted in numerical calculations
- Assisted in the application of the rescaling scheme

Candidate's Signature

Date

Principal Supervisor's signature

Date